POLITECHNIKA ŚLĄSKA

Wydział Inżynierii Biomedycznej

Analiza tekstury obrazów tomografii komputerowej kręgosłupa w celu wykrywania obszarów objętych osteoporozą

Autor: **Róża Dzierżak**

Promotor: prof. dr hab. inż. **Ewaryst Tkacz**

Zabrze 2023

SPIS TREŚCI

STRESZCZENIE

Analiza tekstury obrazów tomografii komputerowej kręgosłupa w celu wykrywania obszarów objętych osteoporozą

Z uwagi na fakt starzenia się społeczeństwa, osteoporoza stała się poważną chorobą cywilizacyjną, która dotyka coraz więcej osób na świecie. Problem odpowiednio wczesnej diagnostyki stał się jeszcze bardziej aktualny w obliczu pandemii COVID-19. Pacjenci znacznie rzadziej kierowani byli na badania diagnostyczne przez co wielu z nich nadal żyje w nieświadomości rozwijającej się choroby. Wpływ na zaburzenia metabolizmu tkanki kostnej mają również glikokortykosteroidy szeroko stosowane w terapii pacjentów dotkniętych COVID-19. W połączeniu ze spadkiem aktywności fizycznej podczas lockdownu oraz złej diety, powoduje to znaczne zwiększenie grupy ryzyka zagrożonej osteoporozą. Wymienione aspekty przemawiają za zasadnością poszukiwania nowych rozwiązań diagnostycznych pozwalających na identyfikację osteoporozy na jej wczesnym etapie, zanim doprowadzi ona do złamań osteoporotycznych mogących mieć poważne konsekwencje.

Niniejsza rozprawa oparta o cykl czterech publikacji prezentuje metody analizy i klasyfikacji obrazów tkanki gąbczastej kręgu L1 wykonanych techniką tomografii komputerowej. Na potrzeby przeprowadzonych badań stworzono bazę danych obrazowych zawierającą wyniki badań pacjentów przypisanych do dwóch grup: grupy kontrolnej osób zdrowych oraz grupy osób chorych u których zdiagnozowano osteoporozę.

W przeprowadzonych badaniach wykorzystano trzy główne podejścia stosowane w analizie i klasyfikacji obrazów, obejmujące zastosowanie klasycznych metod uczenia maszynowego w połączeniu z analizą cech tekstury, zastosowanie głębokich konwolucyjnych sieci neuronowych oraz analizy fraktalnej. Przedstawione w publikacjach wyniki świadczą o skuteczności wybranych metod, a dalsze zaplanowane działania naukowe dają szansę na dostosowanie ich do praktycznego zastosowania. Opracowane algorytmy mogą stać się podstawą do stworzenia systemu automatycznej diagnostyki ubytków w mikroarchitekturze tkanki kostnej pozwalającego na wczesną identyfikację zmian osteoporotycznych.

Słowa kluczowe: osteoporoza, analiza tekstury, analiza fraktalna, klasyfikacja, konwolucyjne sieci neuronowe

SUMMARY

Texture analysis of spine CT images to detect the areas affected by osteoporosis

Due to the fact that the population is aging, osteoporosis has become a serious disease of civilization that affects an increasing number of people worldwide. The problem of timely diagnosis has become even more topical in the face of the COVID-19 pandemic. Patients have been referred much less frequently for diagnostic tests due to which many still live in ignorance of the developing disease. Bone metabolism disorders are also influenced by glucocorticosteroids widely used in the treatment of patients affected by COVID-19. Combined with a decrease in physical activity during lockdown and poor diet, this results in a significant increase in the risk group at risk for osteoporosis. The afore-mentioned aspects justify the search for new diagnostic solutions to identify osteoporosis at its early stage, before it leads to osteoporotic fractures that can have serious consequences.

This dissertation, based on a series of four publications, presents the methods for analyzing and classifying images of the spongy tissue of the L1 vertebrae taken by computed tomography. For the purposes of the study, an image database was created containing the results of patients assigned to two groups: a control group of healthy subjects and a group of patients diagnosed with osteoporosis.

In the conducted research, three main approaches used in image analysis and classification were employed, including the application of classical machine learning methods combined with texture feature analysis, the use of deep convolutional neural networks and fractal analysis. The results presented in the publications prove the effectiveness of the selected methods, and further planned scientific activities provide an opportunity to adapt them to practical application. The developed algorithms can become the basis for the creation of a system for automatic diagnosis of defects in the microarchitecture of bone tissue allowing early identification of osteoporotic lesions.

Keywords: osteoporosis, texture analysis, fractal analysis, classification, convolutional neural networks

WYKAZ WAŻNIEJSZYCH OZNACZEŃ

L – oznaczenie kręgów lędźwiowych kręgosłupa

CT – tomografia komputerowa (ang. *Computed Tomography*)

BMD – mineralna gęstość kości (ang. *Bone Mineral Density*)

DXA – dwuwiązkowa absorpcjometria rentgenowska (ang. *Dual-Energy X-ray Absorptiometry*)

LDA, QDA – liniowa i kwadratowa analiza dyskryminacyjna (ang. *linear and quadratic discriminant analysis*),

SVM – metoda wektorów wspierających (ang. *support vector machines*)

KNN – K – najbliższych sąsiadów (ang. *K-nearest neighbors*)

DT – drzewo decyzyjne (ang. *decision tree*)

MLP – perceptron wielowarstwowy (ang. *multi-layer perceptron*)

RF – lasy losowe (ang. *random forest*)

LR – regresja logistyczna (ang. *logistic regression*)

CNN – konwolucyjne sieci neuronowe (ang. *Convolutional Neural Network*)

DCNN – głębokie konwolucyjne sieci neuronowe (ang. *Deep Convolutional Neural Network*)

ACC – dokładność klasyfikacji (ang. *Classification Accuracy*)

TPR – wrażliwość, czułość (ang. *True Positive Rate*)

TNR – specyficzność (ang. *True Negative Rate*)

ERR – błąd klasyfikacji (ang. *Classification Error*)

FPR – wskaźnik fałszywie dodatni (ang. *False Positive Rate*)

PPV – wartość predykcyjna dodatnia (ang. *Positive Predictive Value*)

NPV – wartość predykcyjna ujemna (ang. *Negative Predictive Value*)

FDR – wskaźnik fałszywego rozpoznania (ang. *False Discovery Rate*)

CB – baza konwolucyjna (ang. *Convolution Base*)

1. WSTĘP

1.1 *Uzasadnienie podjęcia tematyki pracy*

Według definicji Światowej Organizacji Zdrowia (WHO, 1994 r.) *osteoporoza jest układową chorobą szkieletu, charakteryzującą się niską masą kości, upośledzeniem mikroarchitektury tkanki kostnej i w konsekwencji jej zwiększoną podatnością na złamania* [15]. Występowanie osteoporozy najczęściej związane jest z wiekiem, kiedy to zaburzenia remodelingu tkanki kostnej prowadzą do jej ujemnego bilansu. Z uwagi na fakt starzenia się społeczeństwa, osteoporoza stała się poważną chorobą cywilizacyjną. W końcu 2021 r. liczba ludności Polski wyniosła 38,1 mln, w tym ponad 9,8 mln stanowiły osoby w wieku 60 lat i więcej (25,8%). W stosunku do 2020 r. liczba osób w wieku senioralnym wzrosła o 28,6 tys. osób tj. o 0,3%. W populacji osób w starszym wieku większość stanowią kobiety. W 2021 r., podobnie jak rok wcześniej, stanowiły one 58,1% [17]. Ostatni oficjalny raport Narodowego Funduszu Zdrowia, przedstawiający dane statystyczne związane z osteoporozą, został opublikowany w listopadzie 2019 roku [26]. Szacowana liczba osób chorych na osteoporozę w Polsce w 2018 roku (oparta na wskaźnikach epidemiologicznych) to 2,1 mln, z czego 1,7 mln to właśnie kobiety. Tym samym szacuje się, że liczba osób z niezdiagnozowaną osteoporozą w 2018 roku wahała się od 86 tys. (w przedziale wiekowym 50÷54 lata) do 247 tys. (w przedziale wiekowym 80÷84 lata). Według tego raportu już w 2019 roku prognoza dla Polski wskazywała, że bezwzględna liczba osób zagrożonych osteoporozą będzie rosła, pomimo zmniejszania się populacji kraju [26].

Przedstawione powyżej statystyki i prognozy dotyczące osteoporozy, zawierają dane sprzed okresu pandemii COVID-19. Należy pamiętać, że w ostatnich trzech latach pacjenci znacznie rzadziej kierowani byli na dedykowane osteoporozie badania kontrolne, więc wielu pacjentów nadal żyje z brakiem świadomości o dotykającej ich chorobie. Według Międzynarodowej Fundacji Osteoporozy już w kwietniu 2020 roku obliczenia ryzyka złamania FRAX spadło o 58%, przez co ponad 0,5 miliona pacjentów z 66 krajów zostało wykluczonych z oceny ryzyka, a wielu z koniecznego leczenia osteoporozy [7, 24]. Poza brakiem wykonywania badań diagnostycznych również styl życia jaki społeczeństwo prowadziło podczas lockdownu, znaczenie przyczynił się do rozwoju tej choroby. Brak aktywności fizycznej, nieodpowiednia dieta, niskie spożycie wapnia i fosforu, nadmierne spożywanie alkoholu oraz niedobory witaminy D, to czynniki ryzyka, które zwiększają prawdopodobieństwo wystąpienia osteoporozy.

Poza wymienionymi powyższej czynnikami związanymi z pandemią i trybem życia sprzyjającymi rozwojowi osteoporozy, kluczową rolę odgrywa wpływ obecności COVID-19 w organizmie człowieka oraz oddziaływanie terapii farmakologicznej u osób zakażonych. Artykuł [34] zawiera przegląd informacji wskazujących, że COVID-19 może mieć bezpośredni i pośredni wpływ na osteoklasty i osteoblasty oraz prowadzić do osteoporozy. Produkcja cytokin prozapalnych wzrasta wraz z zakażeniem COVID-19, co może skutkować utratą masy kostnej i resorpcją kości u ciężko chorych pacjentów, zwłaszcza w podeszłym wieku, którzy pozostają przez długi czas unieruchomieni [16].

Kolejnym aspektem, który należy wziąć pod uwagę, jest negatywny wpływ terapii glikokortykosteroidami na metabolizm kości. Glikokortykosteroidy są powszechnie wykorzystywane w leczeniu zespołu ostrej niewydolności oddechowej, ponieważ zmniejszają stan zapalny i poprawiają funkcjonowanie płuc [37]. W związku z tym terapia z ich wykorzystaniem jest szeroko stosowana również w leczeniu pacjentów z COVID-19 [12].

Szacuje się, że zmiany osteoporotyczne wywołane stosowaniem glikokortykosteroidów są najczęstszą przyczyną osteoporozy wtórnej i trzecią najczęstszą przyczyną osteoporozy po osteoporozie postmenopauzalnej i osteoporozie starczej [34, 30]. Już w 2002 roku opublikowano badania wskazujące, że osoby przyjmujące doustne glikokortykosteroidy były prawie trzy razy bardziej narażone na złamanie kręgów [34, 36]. Osteoporoza i niska gęstość mineralna kości mogą być wynikiem niekorzystnego wpływu tych substancji na funkcję komórek kostnych i metabolizm mineralny. Objawy osteoporozy wywołanej glikokortykosteroidami są trudne do wykrycia we wczesnym stadium, dlatego w późniejszym okresie może wystąpić szereg powikłań, takich jak złamania i martwica kości [34].

Biorąc pod uwagę powyższe czynniki należy spodziewać się znacznego wzrostu zachorowań na osteoporozę w ciągu najbliższych lat. Jednym z największych problemów związanych z tą chorobą jest jej bezobjawowy charakter. Najczęściej osteoporoza diagnozowana jest na etapie zaawansowanym, kiedy dochodzi już do złamań osteoporotyczych. Raport Europejskiej Fundacji Osteoporozy i Chorób Mięśniowo-Szkieletowych oraz Polskiego Towarzystwa Ortopedycznego i Traumatologicznego dotyczący osteoporozy w Polsce [27], informuje, że po 50 roku życia złamania te występują u 30% kobiet i 8% mężczyzn. Złamania osteoporotyczne są wyjątkowo niebezpieczne w przypadku kręgosłupa, gdzie obniżenie wzrostu i deformacje sylwetki (np. pogłębienie kifozy) prowadzą do zmniejszenia pojemności oddechowej płuc oraz pogorszenia wydolności układu krążeniowo-oddechowego, co w konsekwencji skutkuje zgonem pacjenta.

Nie sposób nie wspomnieć o aspekcie ekonomicznym związanym z osteoporozą. Ostatnie dostępne dane Narodowego Funduszu Zdrowia szacowane na podstawie liczby złamań w roku 2018 wskazują, że refundacja bezpośrednich kosztów leczenia wyniosła ok 18,0 mln zł [26]. Z uwagi na fakt, wzrostowej tendencji zachorowań koszty te będą się sukcesywnie zwiększać.

Powyższe aspekty obrazują jak ważnym problemem jest epidemia osteoporozy i jak daleko idące konsekwencje może za sobą nieść. Zdaniem autorki poza szeroko zakrojoną akcją informacyjną i profilaktyczną konieczne jest opracowanie procedury badań przesiewowych wykonywanych standardowo dla osób w określonej grupie wiekowej narażonej na ubytki w tkance kostnej. Rozwiązaniem, które według autorki mogłoby korzystnie wpłynąć na diagnostykę osteoporozy jest stworzenie dodatkowego modułu diagnostycznego do stosowanego w placówkach medycznych oprogramowania, pozwalającego na automatyczną analizę tekstury tkanki kostnej podczas badania wykonywanego w innych celach diagnostycznych. Jeśli taka analiza obrazu tkanki byłaby możliwa podczas badań CT, np. u osób z wypadków, gdzie badanie służy wykryciu ewentualnych urazów, pozwoliłoby to znacznie poszerzyć grono badanych osób i wykryć zmiany w tkance kostnej u pacjentów, którzy prawdopodobnie nie zostaliby skierowani na specjalistyczne badania pod kątem utraty masy kostnej. Tego typu rozwiązanie nie generowałoby dodatkowych kosztów, a bazowało jedynie na obrazach wykorzystywanych do diagnostyki innych schorzeń.

W związku z powyższym autorka skupiła swoje działania na badaniach, które mogłyby stać się podstawą do stworzenia dodatkowego, kompatybilnego z obecnie stosowanymi urządzeniami i oprogramowaniem modułu diagnostycznego do analizy obrazu mikroachitektury tkanki gąbczastej i wykrywania ich ewentualnych ubytków. Zamieszczony w rozprawie cykl czterech publikacji przedstawia różne podejścia obejmujące analizę tekstury oraz klasyfikację obrazów tkanki. Tematyka związana z diagnostyką osteoporozy pojawia się również w innych publikacjach autorki, które nie wchodzą w skład niniejszej rozprawy. Złożoność poruszanego problemu podkreślają również sprecyzowane plany kolejnych badań przedstawione w podsumowaniu niniejszej pracy. Z uwagi na fakt, że to właśnie w odcinku lędźwiowym kręgosłupa najwcześniej pojawiają się zmiany osteoporotyczne, co wynika z dużego obszaru występowania tkanki beleczkowej, autorka skupiła się na obszarze kręgosłupa. Kręg L1 statystycznie jest najbardziej narażony na złamania osteoporotyczne [2].

1.2 *Stan wiedzy w zakresie diagnostyki osteoporozy*

Osteoporoza spowodowana jest zaburzeniami równowagi w procesie ciągłej przebudowy tkanki kostnej. Za proces remodelingu odpowiedzialne są dwa rodzaje komórek – osteoklasty oraz osteoblasty. Osteoklasty odpowiedzialne są za resorpcję i demineralizację dojrzałej tkanki kostnej. Osteoblasty tworzą nową tkankę kostną, gdzie do osteoidu, pełniącego funkcję rusztowania kostnego, następuje przyłączanie jonów wapnia i formowanie hydroksyapatytu. [35]. W przypadku nadaktywności osteoklastów następuje wzmożona resorpcja tkanki kostnej oraz zaburzona zostaje struktura blaszek kostnych istoty gąbczastej. Powoduje to zmianę zwartej dotąd struktury drobnowłóknistej tkanki i czyni ją mniej odporną na czynniki uszkadzające [32]. Mikroarchitektura tkanki kostnej staje się porowata, co może prowadzić do powstawania złamań osteoporotycznych. Podobnie dzieje się w przypadku zaburzeń pracy osteoblastów, które tworzą nową tkankę. W obu przypadkach brak homeostazy w procesie przebudowy tkanki może skutkować stopniową utratą masy kostnej i doprowadzić do osteopenii lub osteoporozy.

Obecnie złotym standardem w diagnostyce osteoporozy jest densytometria (DXA), polegająca na pomiarach gęstości mineralnej kości (BMD) [2]. Głównym celem tego badania jest identyfikacja pacjentów szczególnie zagrożonych wystąpieniem złamań oraz częściowe monitorowanie skuteczności leczenia [33]. Densytometria najczęściej wykonywana jest w obrębie kości udowej oraz części lędźwiowej kręgosłupa. Znaczącą zaletą pomiarów gęstości mineralnej tkanki kostnej kręgosłupa jest duża zawartość kości beleczkowej, przez co to właśnie tam najwcześniej pojawią się zmiany osteoporotyczne. Dzięki temu możliwe jest w miarę dokładne określenie ryzyka złamań w tej lokalizacji (najczęstsze występują w kręgu L1). Jednak problemem pojawiającym się wraz z zaawansowanym wiekiem pacjentów są zmiany zwyrodnieniowe kręgosłupa, które poprzez generowanie osteofitów podnoszą wartość gęstości mineralnej kości [2, 20].

Podstawą do interpretacji wyników badania densytometrycznego jest współczynnik T-score odnoszący gęstość mineralną kości pacjenta do szczytowej masy kostnej dla młodych dorosłych tej samej płci.

Przedziały wartości współczynnika T-score są następujące:

• od +1 do -1 odchylenia standardowego (SD) oznacza normę;

• wartość od -1 do -2,5 SD oznacza osteopenię;

• wartość mniejsza od -2,5 SD oznacza rozpoznanie osteoporozy [31].

Podczas rozpoznawania osteoporozy na podstawie niskiej wartości BMD lub wskaźnika T-score mniejszego od -2,5 SD, należy również brać pod uwagę całokształt obrazu klinicznego pacjenta ze szczególnym uwzględnieniem czynników ryzyka [33]. Stwierdzona na podstawie badania DXA obniżona gęstość mineralna kości wymaga diagnostyki różnicowej dla ustalenia jej podłoża. W tym celu wykonuje się badania krwi i moczu [19].

W literaturze wciąż pojawiają się nowe badania przedstawiające alternatywne rozwiązania w zakresie diagnostyki osteoporozy w różnych obszarach tkanki kostnej człowieka. Według Google Scholar w ciągu ostatnich trzech lat powstało ponad 82 tysiące prac w tej tematyce. Analiza dostępnych publikacji wykazała, że najczęstszym kierunkiem badań jest analiza obrazu mikroarchitektury tkanki kostnej [25]. Artykuł [21] pokazuje kliniczne zainteresowanie analizą tekstury kości za pomocą urządzenia rentgenowskiego o wysokiej rozdzielczości. Badania te wykazały, że połączenie wartości BMD i parametrów tekstury pozwoliło na lepszą ocenę ryzyka złamania niż ta, którą można uzyskać wyłącznie na podstawie pomiaru BMD. Analiza tekstury znalazła również zastosowanie w diagnostyce kości biodrowej, co opisano w pracy [14]. Wykazano w niej, że najbardziej wydajnymi cechami są cechy kowariancji − zapewniają one prawdopodobieństwo błędu diagnostycznego na poziomie 0,2. Podobne wnioski przedstawiono również w pracach [6, 13, 22, 39], w których także wykazano związek między BMD a parametrami tekstury. Autorzy pracy [8] zaproponowali multifraktalną metodę charakteryzowania tekstury kości beleczkowej. Skuteczność tej metody potwierdzono również w badaniach [1, 4, 28, 3]. Kolejnym popularnym podejściem w diagnostyce osteoporozy jest zastosowanie głębokich sieci neuronowych do klasyfikacji obrazów tkanki. W pracy [29] wykorzystano cztery modele sieci CNN: AlexNet, VGGNet, ResNet oraz DenseNet. Badania [18] wykorzystujące model VGG16 w diagnostyce stawu biodrowego pozwoliły na uzyskanie ogólnej dokładności na poziomie 81,2% oraz czułości 91,1%. Obiecujące wyniki zastosowania DNN zostały uzyskane w przypadku analizy obrazów kręgosłupa [38, 11, 23].

Poza coraz nowszymi badaniami w zakresie diagnostyki osteoporozy pojawiają się również liczne badania w zakresie jej leczenia. Wykorzystywane dotychczas standardowo leki antyresorpcyjne (bisfosfoniany, denosumab) mogą znaleźć swoją alternatywę np. w inżynierii komórkowej i genetycznej. Patofizjologia osteoporozy różni się u poszczególnych osób, dlatego leczenie powinno być spersonalizowane. Identyfikacja indywidualnej patologii metabolizmu kostnego pozwoli na lepsze dopasowanie leczenia za pomocą terapii skojarzonych [35].

1.3 *Cel i zakres badań*

Celem badań było opracowanie algorytmu opartego na analizie tekstury obrazu CT tkanki gąbczastej kręgosłupa w celu identyfikacji ubytków osteoporotycznych. Niniejsza rozprawa oparta jest o cykl czterech publikacji:

[A1]. *Comparison of the Classification Results Accuracy for CT Soft Tissue and Bone Reconstructions in Detecting the Porosity of a Spongy Tissue*, **Róża Dzierżak**, Zbigniew Omiotek, Ewaryst Tkacz, Sebastian Uhlig, Journal of Clinical Medicine, 2022, vol. 11, nr 15, s. 1−11 [MNiSW: 140].

[A2]. *Application of Deep Convolutional Neural Networks in the Diagnosis of Osteoporosis*, **Róża Dzierżak**, Zbigniew Omiotek, Sensors, 2022, vol. 22, nr 21, s. 1−18 [MNiSW: 100].

[A3]. *Fractal analysis as a method for feature extraction in detecting osteoporotic bone destruction*, Zbigniew Omiotek, **Róża Dzierżak**, Andrzej Kępa, Fractals : Complex Geometry, Patterns, and Scaling in Nature and Society, 2021, vol. 29, nr 4, s. 1−15 [MNiSW: 100].

[A4]. *The Influence of the Normalisation of Spinal CT Images on the Significance of Textural Features in the Identification of Defects in the Spongy Tissue Structure*, **Róża Dzierżak**, Zbigniew Omiotek, Ewaryst Tkacz, Andrzej Kępa. [W]: Innovations in Biomedical Engineering, Springer, 2019, s. 55−66 [MNiSW: 20].

Sumaryczny Impact Factor (IF) cyklu publikacji przedstawionych jako osiągnięcia naukowe wynosi **13,366**, a sumaryczna liczba punktów ministerialnych publikacji wchodzących w skład osiągnięcia naukowego wynosi **360** (liczona według punktacji z roku publikacji).

W swoich badaniach autorka skupiła się na trzech głównych metodach analizy i klasyfikacji obrazów:

- zastosowanie klasycznych metod uczenia maszynowego do klasyfikacji obrazów na podstawie analizy cech tekstury;
- zastosowanie głębokich konwolucyjnych sieci neuronowych;
- zastosowanie analizy fraktalnej.

Poza wymienionymi powyżej pozycjami literatury autorka posiada w swoim dorobku naukowym jeszcze inne publikacje, prezentujące wyniki badań związanych z diagnostyką osteoporozy, które nie zostały włączone do rozprawy.

1. *Comparison of the influence of standardization and normalization of data on the effectiveness of spongy tissue texture classification*, **Róża Dzierżak**, Informatyka, Automatyka, Pomiary w Gospodarce i Ochronie Środowiska, 2019, vol. 9, nr 3, s. 66−69.
2. *Fractal analysis of the computed tomography images of vertebrae on the thoraco-lumbar region in diagnosing osteoporotic bone damage*, Zbigniew Omiotek, **Róża Dzierżak**, Sebastian Uhlig, Proceedings of the Institution of Mechanical Engineers Part H-Journal of Engineering in Medicine, 2019, vol. 233, nr 12, s. 1269−1281.
3. *The influence of the principal component analysis of texture features on the classification quality of sponge tissue images*, **Róża Dzierżak**, Informatyka, Automatyka, Pomiary w Gospodarce i Ochronie Środowiska, 2020, vol. 10, nr 3, s. 13−16.
4. *Zastosowanie klasyfikatorów tekstury w analizie obrazów medycznych*, **Róża Dzierżak**. [W]: Trendy i rozwiązania technologiczne – odpowiedź na potrzeby współczesnego społeczeństwa. T. 1., 2017, s. 212−221.
5. *Application of neural networks in the classification of medical images textures*, **Róża Dzierżak**, Waldemar Wójcik, Iskusstvennyj Intellekt-Naučno-Teoretičeskij Žurnal (Искусственный Интеллект), 2018, vol. 79, nr 1, s. 49−55.

Przedstawione publikacje zawierają badania, które miały znaczny wpływ na ostateczną wersję opracowanych algorytmów. Autorka w swoim dorobku posiada również rozprawę doktorską pt. „*Zastosowanie konwolucyjnych sieci neuronowych w diagnostyce osteoporozy*" obronioną w dyscyplinie automatyka, elektronika i elektrotechnika na Politechnice Lubelskiej w 2020 roku.

Niniejszą rozprawę opartą o cykl czerech publikacji, dopełniono opisem materiału badawczego, jakim jest baza obrazów CT kręgosłupa oraz opisem metod analizy i klasyfikacji obrazów, wykorzystanych w załączonych publikacjach. Przedstawiona literatura obejmuje pozycje bezpośrednio wymienione w treści rozprawy, natomiast pełne listy źródeł literaturowych znajdują się w części prezentującej poszczególne artykuły autorki. W załączniku nr 1 przedstawiono zbiór obrazów będących przedmiotem badań.

2. MATERIAŁ WYKORZYSTANY W BADANIACH

Na potrzeby badań związanych z opracowaniem algorytmów diagnostyki osteoporozy zbudowano bazę danych obrazowych CT odcinka lędźwiowo-krzyżowego (L – S) kręgosłupa. Baza ta posłużyła do przeprowadzenia wszystkich analiz prezentowanych w pracach naukowych autorki.

Badania obrazowe CT pochodzą z poradni ortopedycznej oraz oddziału SOR w Samodzielnym Szpitalu Klinicznym w Lublinie. Obrazy przedstawiają odcinek lędźwiowo – krzyżowy 100 pacjentów podzielonych na dwie grupy (grupę kontrolną oraz grupę chorych). Podczas wcześniejszych badań przeprowadzono analizę mocy testu istotności statystycznej uzyskanych wyników oraz związaną z nią ocenę wymaganej liczebności próby [9]. Grupa kontrolna obejmowała 26 kobiet i 24 mężczyzn w wieku od 53 do 77 lat bez objawów osteoporozy i osteopenii. Grupę chorych stanowiły 33 kobiety i 17 mężczyzn w wieku od 44 do 95 lat ze stwierdzoną osteoporozą. Dokładne dane dotyczące pacjentów oraz parametrów ekspozycji zastosowanych podczas badania tomograficznego zostały przedstawione w Tab. 2.1.

Tab. 2.1. Zestawienie danych pacjentów oraz parametrów ekspozycji zastosowanych podczas badania tomograficznego

Grupa kontrolna					Grupa z osteoporozą				
Dane pacjenta			Parametry ekspozycji		Dane pacjenta			Parametry ekspozycji	
Numer pacjenta	Płeć	Wiek	Natężenie prądu [mA]	Napięcie [kV]	Numer pacjenta	Płeć	Wiek	Natężenie prądu [mA]	Napięcie [kV]
1	M	72	225	140	1	M	75	181	140
2	M	58	301	140	2	K	88	310	140
3	M	57	181	140	3	M	56	167	120
4	K	55	181	140	4	K	44	181	140
5	K	53	181	140	5	K	56	99	120
6	K	77	181	140	6	M	63	181	140
7	M	68	209	120	7	M	74	181	140

8	K	69	181	140	8	K	83	150	120
9	M	62	181	140	9	K	70	181	140
10	K	63	339	140	10	K	85	181	140
11	K	68	181	140	11	M	66	181	140
12	M	75	385	140	12	M	95	113	120
13	M	74	253	120	13	K	71	181	140
14	K	42	301	140	14	K	76	181	140
15	K	64	335	120	15	K	70	181	140
16	K	61	99	120	16	K	92	181	140
17	M	73	215	140	17	K	68	180	140
18	M	72	194	120	18	M	78	152	120
19	K	63	181	140	19	K	75	499	120
20	M	59	181	140	20	M	67	700	120
21	M	59	181	140	21	K	82	181	140
22	M	66	499	120	22	K	76	99	120
23	K	68	319	140	23	K	73	181	140
24	K	57	332	120	24	K	78	181	140
25	K	68	99	120	25	K	82	181	140
26	K	62	181	140	26	K	74	128	120
27	M	60	181	140	27	M	75	356	140
28	K	62	117	120	28	K	74	499	120
29	M	57	445	120	29	K	73	181	140
30	M	67	254	120	30	K	71	85	120
31	M	65	330	120	31	M	54	168	120
32	K	57	181	140	32	M	65	180	120

33	M	65	499	120	33	K	72	122	120
34	M	60	265	140	34	K	75	260	120
35	M	60	181	140	35	M	68	181	140
36	K	65	268	120	36	M	87	181	140
37	K	62	248	140	37	K	77	126	120
38	M	65	190	140	38	M	82	181	140
39	M	57	181	140	39	K	69	180	140
40	K	59	159	120	40	K	74	181	140
41	K	57	181	140	41	K	63	181	120
42	K	62	499	120	42	K	70	99	120
43	K	58	206	140	43	K	82	330	120
44	K	74	198	120	44	K	69	164	120
45	M	57	181	140	45	K	89	144	120
46	K	59	181	140	46	M	59	181	140
47	M	61	194	120	47	M	58	180	140
48	K	67	234	120	48	K	81	181	140
49	M	59	181	140	49	K	75	260	120
50	K	61	99	120	50	M	65	181	140

Kwalifikacja pacjentów do poszczególnych grup została przeprowadzona przy współpracy z radiologiem. Podstawą kwalifikacji był opis badania sporządzony przez lekarza specjalistę oraz pomiar gęstości radiologicznej tkanki gąbczastej pierwszego kręgu odcinka lędźwiowego kręgosłupa (L1). Na podstawie literatury, jako wartość graniczną gęstości tkanki przyjęto 120 jednostek Hounsfielda (HU) [10]. Pacjenci, u których gęstość była znacząco większa od wartości granicznej oraz opis badania nie sugerował zmian w strukturze tkanki, zakwalifikowani zostali do grupy kontrolnej. W związku z brakiem wyników standardowych badań diagnostycznych takich jak wskaźnik BMD, określono dodatkowe kryterium

kwalifikacji do grupy osób chorych jakim było osteoporotyczne złamanie kręgu, możliwe do zdiagnozowania na podstawie obrazu pochodzącego z tomografii komputerowej.

Z serii obrazów każdego badania CT wybrano cztery obrazy przekroju poprzecznego kręgu L1 na poziomie jego środka (Rys. 2.1. Ilustracja doboru obszaru tkanki gąbczastej do badań). Pozwoliło to na uzyskanie możliwie jak największej powierzchni próbki przedstawiającej teksturę tkanki gąbczastej kręgu. W wyniku tego uzyskano czterysta próbek o wymiarach 50x50 pikseli.

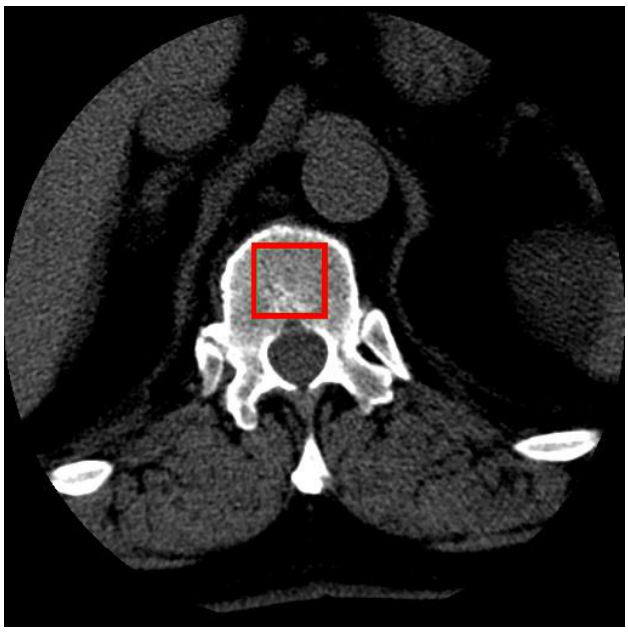

Rys. 2.1. Ilustracja doboru obszaru tkanki gąbczastej do badań

Przykładowe obrazy tkanki próbek pacjentów zdrowych oraz pacjentów chorych zamieszczono poniżej (Rys. 2.2), natomiast komplet 400 obrazów przedstawiono w załączniku nr 1.

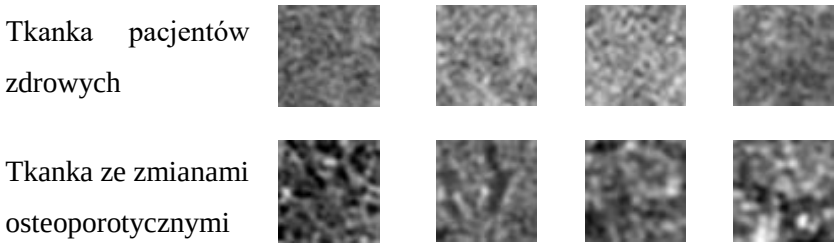

Rys. 2.2. Próbki obrazowe tkanki pacjentów zdrowych oraz tkanki ze zmianami osteoporotycznymi w oryginalnym rozmiarze

3. OMÓWIENIE METOD BADAWCZYCH I WYNIKÓW OPISANYCH W ARTYKUŁACH WCHODZĄCYCH W SKŁAD ROZPRAWY

3.1 *Analiza tekstury obrazu tkanki gąbczastej w rekonstrukcji kostnej i miękkotkankowej*

Artykuł *Comparison of the Classification Results Accuracy for CT Soft Tissue and Bone Reconstructions in Detecting the Porosity of a Spongy Tissue (**Róża Dzierżak**, Zbigniew Omiotek, Ewaryst Tkacz and Sebastian Uhlig)* przedstawia porównanie wyników klasyfikacji obrazów CT na podstawie wartości cech tekstury przy zastosowaniu dwóch różnych filtrów rekonstrukcyjnych.

Obraz pochodzący z tomografii komputerowej uzyskiwany jest na drodze przekształceń i obliczeń matematycznych, wykonywanych podczas procesu pomiarowego. Proces przekształcający dane pierwotne do obrazu tomograficznego nazywamy rekonstrukcją. Z uwagi na różnorodność struktur, występujących w ciele człowieka, konieczne jest zastosowanie różnych filtrów rekonstrukcyjnych. Podczas oceny stanu narządów o dużym kontraście struktur wewnętrznych, jak np. kości lub płuca, stosuje się rekonstrukcję kostną (algorytm twardy) o wysokiej rozdzielczości, która powoduje wzmocnienie krawędzi. Do oceny tkanek miękkich i narządów o mniejszym kontraście struktur wewnętrznych, stosowana jest rekonstrukcja miękkotkankowa (algorytm miękki), która redukuje szum, kosztem zmniejszenia rozdzielczości przestrzennej. Dzięki zastosowaniu różnych filtrów rekonstrukcyjnych możliwe jest odpowiednie dostosowanie obrazu badanych tkanek do dalszych analiz.

W omawianej pracy przedstawiono proces klasyfikacji obrazów istoty gąbczastej w kręgu lędźwiowym L1 na podstawie uzyskanych cech tekstury. Istota gąbczasta zaliczana jest do tkanek kostnych, jednak budujące ją blaszki są luźno ułożone, a poziom jej zmineralizowania około 3 razy niższy niż w istocie zbitej.

Podczas oceny stanu tkanki gąbczastej, zarówno przez radiologów podczas standardowej oceny diagnostycznej, jak również w większości artykułów poświęconych temu tematowi, wykorzystywane są obrazy pochodzące z rekonstrukcji kostnej. Z uwagi na nietypowy charakter tkanki gąbczastej, o którym wspominano powyżej, w niniejszej pracy wykorzystano dwa rodzaje rekonstrukcji obrazów, rekonstrukcję miękkotkanową oraz kostną. Głównym przedmiotem badań była weryfikacja, który rodzaj zrekonstruowanych obrazów umożliwia otrzymanie cech tekstury, pozwalających na dokładniejszą klasyfikację stanu tkanki.

Deskryptory cech tekstury zostały obliczone za pomocą oprogramowania MaZda, pozwalającego na wyznaczenie wartości liczbowych 290 cech na podstawie analizy statystycznej histogramu obrazu szarości, modelu autoregresji oraz transformacji falkowej.

Kolejnym krokiem była redukcja danych poprzez selekcję cech, mającą na celu ograniczenie pełnego zbioru do podzbioru, zawierającego cechy istotne z punktu widzenia zastosowanego kryterium. Wykorzystano do tego 9 metod reprezentujących różne podejścia (metody filtrujące, opakowujące i osadzone). W trakcie procesu selekcji danych cały zestaw 290 cech został znacznie zredukowany – do 32 dla obrazów rekonstrukcji kostnej i 18 dla rekonstrukcji miękkotkankowej. Lista rankingowa zawierała zestaw cech w kolejności odzwierciedlającej ich istotność pod względem dyskryminacji obserwacji należących do różnych klas.

Do budowy modeli klasyfikatorów wykorzystano 11 metod: liniową i kwadratową analizę dyskryminacyjną (LDA, QDA), gaussowską naiwną metodę Bayesa (BAYES), maszyny wektorów wspierających (SVM) wykorzystujące parametr regularyzacji C, maszyny wektorów wspierających (NuSVM) wykorzystujące parametr do sterowania liczbą podpór wektory *nu,* K-najbliższych sąsiadów (KNN), drzewo decyzyjne (DT), perceptron wielowarstwowy (MLP) oraz trzy metody zespołowe – las losowy (RF), wzmacnianie gradientu (GRAD), AdaBoost (ADA). W procesie uczenia zastosowano optymalizację hiperparametryczną opartą na metodzie grid search. Na tej podstawie określono najbardziej efektywny model i optymalny podzbiór cech dla każdej zastosowanej metody selekcji.

W przypadku obrazów rekonstrukcji kostnej 4 modele osiągnęły maksymalną dokładność 92%, z czego jeden miał najwyższą czułość 95%, przy swoistości 89%. W przypadku obrazów rekonstrukcji tkanek miękkich 5 modeli osiągnęło najwyższą dokładność badania na poziomie 95%, gdzie pozostałe wskaźniki jakości (TPR i TNR) również wyniosły 95%.

Wyniki badań pozwalają stwierdzić, że w przypadku analizy tekstury to rekonstrukcja miękkotkankowa oferuje większą dokładność klasyfikacji (ACC=95%), niż zazwyczaj używana do oceny tkanki gąbczastej rekonstrukcja kostna (ACC=92%). Z uwagi na nietypowy charakter badanej tkanki, którą wyróżnia niższa gęstość mineralna, niż w istocie zbitej, więc obraz z rekonstrukcji miękkotkankowej zawiera dokładniejszy zakres wartości cech tekstury. W jej przypadku, aż 5 klasyfikatorów uzyskało te same najlepsze wartości zastosowanych indeksów jakości (ACC=TPR=TNR=95%). Potwierdza to zasadność przeprowadzonych badań i wskazuje nowe możliwości wynikające z odmiennego podejścia do analizowanej tkanki.

3.2 *Konwolucyjne sieci neuronowe*

Artykuł *Application of Deep Convolutional Neural Networks in the Diagnosis of Osteoporosis (**Róża Dzierżak**, Zbigniew Omiotek)* prezentuje wyniki badań nad możliwością zastosowania głębokich konwolucyjnych sieci neuronowych (DCNN) do budowy skutecznej metody rozpoznawania osteoporozy na podstawie obrazów CT kręgosłupa.

Ze względu na niewielki (w ujęciu deep learningu) zestaw danych obrazowych, w badaniach wykorzystano wstępnie wytrenowane modele, które z uwagi na zbiór obrazów wykorzystany do jego uczenia, może pełnić rolę ogólnego modelu do przetwarzania obrazów. Po odpowiednim dostosowaniu model ten może być wykorzystany do rozpoznawania innych klas niż te, których użyto w procesie uczenia. Użyte modele zostały wytrenowane na zbiorze ImageNet zawierającym ok. 1,4 miliona obrazów podzielonych na 1000 klas.

W badaniach wykorzystano 6 modeli o zróżnicowanej architekturze i głębokości topologicznej: Xception, VGG16, VGG19, ResNet50, InceptionResNetV2, MobileNetV2. Modele składały się z dwóch głównych części jakimi były wyuczona wcześniej baza konwolucyjna oraz gęsto połączone klasyfikatory usytuowane na końcu sieci. Standardowe klasyfikatory zostały zastąpione gęsto połączonymi warstwami *dense layer*, warstwą *GlobalAveragePooling2D* odpowiadającą za przeprowadzanie operacji *pooling* dla danych przestrzennych na podstawie średniej globalnej oraz warstwą *Dropout* ograniczającą nadmierne dopasowanie modelu do danych treningowych. Pierwszym etapem trenowania modelu była ekstrakcja cech (trenowanie klasyfikatora przy wykorzystaniu obrazów tkanki gąbczastej), natomiast kolejnym dopasowanie sieci.

Najlepsze wyniki uzyskano dla modelu VGG16, charakteryzującego się najmniejszą głębokością topologiczną (ACC=95%, TPR=96% i TNR=94%). Badania wykazały także, że zastosowanie techniki transfer learning podczas uczenia głębokiego z wykorzystaniem małego zbioru danych, również pozwala uzyskać satysfakcjonujące rezultaty. Zaproponowana metoda pozwala znacznie uprościć etap wstępnego przetwarzania i analizy obrazu przed wykorzystaniem obrazów do budowy modelu klasyfikatora. Konwolucyjna sieć neuronowa jest w stanie ujawnić wewnętrzne cechy poszczególnych obserwacji na podstawie surowych danych uzyskanych z obrazów, zapewniając przy tym wysoką skuteczność klasyfikacji.

3.3 *Analiza fraktalna*

W pracy *Fractal analysis as a method for feature extraction in detecting osteoporotic bone destruction* (*Zbigniew Omiotek, **Róża Dzierżak**, Andrzej Kępa*) zastosowano analizę fraktalną do wyznaczenia zbioru deskryptorów cech, który mógłby zostać wykorzystany w procesie diagnostyki osteoporozy.

Nowym podejściem zaprezentowanym w artykule jest to, że podczas analizy zastosowano kilka różnych estymatorów wymiaru fraktalnego, które wykorzystują zarówno obrazy szare, jak i binarne. Najlepsze z nich zostają wybrane za pomocą odpowiedniej metody selekcji. Oprócz wymiarów fraktalnych, oszacowanych różnymi metodami, wykorzystane są także inne parametry uzyskane na podstawie analizy fraktalnej, takie jak intercept (punkt przecięcia) i lacunarity (lakunarność). Takie podejście rozszerza możliwości zaprezentowanej metody. W niniejszej pracy ocena uzyskanego wektora cech zrealizowana została poprzez testowanie zbudowanych klasyfikatorów. Dzięki temu, dostarczona jest informacja o wartości różnych wskaźników jakości klasyfikacji, istotnych dla pacjenta z medycznego punktu widzenia. Na uwagę zasługuje także fakt, iż system diagnostyki osteoporozy, oparty na prezentowanej metodzie ekstrakcji cech, wykorzystywałby wyłącznie deskryptory uzyskane w wyniku analizy fraktalnej.

Komputerowa reprezentacja obrazu medycznego (np. tomografii komputerowej) to macierz obrazu, w której poziomy skali szarości (intensywności) odpowiadające elementom x, y tworzą mniej lub bardziej złożoną powierzchnię. Istnieje wiele algorytmów szacowania wymiaru fraktalnego takich powierzchni. W przedstawionych badaniach zastosowano metody oparte na widmowej gęstości mocy, metodzie graniastosłupów trójkątnych i wariacji, a także metodę box counting, która w analizie wykorzystywała binarną postać obrazu.

Obrazy szare przeznaczone do analizy za pomocą metody box counting zostały poddane segmentacji. W wyniku tego procesu otrzymano obrazy binarne, na podstawie których obliczono wymiar fraktalny oraz lakunarność. Wstępnie, porównano wyniki działania kilku metod segmentacji, wśród których były: lokalne i globalne progowanie Otsu, lokalne progowanie metodą Bradleya, metoda zbiorów poziomicowych, progowanie adaptacyjne i metoda aktywnego konturu. Stan chorobowy tkanki widoczny jest na zdjęciach CT w postaci powiększonych ciemnych plam. Dlatego, podstawowym kryterium jakości segmentacji było wierne odtworzenie tego typu obszarów. Najlepsze efekty osiągnięto za pomocą metody progowania metodą Bradleya, którą zastosowano do segmentacji obrazów w skali szarości.

Do selekcji cech wykorzystano metodę opartą na liniowej regresji krokowej. W procesie klasyfikacji wykorzystano 3 cechy: *Var_FD, Filte*r oraz *Lac*. Zastosowano sześć metod klasyfikacji: liniowa i kwadratowa analiza dyskryminacyjna (LDA, QDA), naiwny klasyfikator Bayesa (NBC), drzewo decyzyjne (DT), K-najbliższych sąsiadów (K-NN) i lasy losowe (RF). Badania pokazały, że analiza fraktalna jest wartościowym narzędziem do ekstrakcji wektora cech obrazów CT kręgosłupa. Najlepsze wyniki uzyskano dla klasyfikatora K-NN (dla k=1 lub 10) ACC=81%, TPR=78%, TNR=90%, PPV=90%, NPV=77%. Uzyskanie stosunkowo dobrej dokładności klasyfikacji możliwe było dzięki jednoczesnemu zastosowaniu deskryptorów fraktalnych obrazów szarych i binarnych.

Do zalet przedstawionej metody należy to, że jest ona nieinwazyjna i oferuje dość dobrą dokładność rozpoznawania przypadków należących do poszczególnych klas. Poza tym, metoda oparta jest na zaledwie trzech cechach wyłonionych wyłącznie na podstawie analizy fraktalnej. Z drugiej strony, pewnym mankamentem zastosowanej metody analizy jest fakt, braku standaryzacji metod szacowania wymiaru fraktalnego. W konsekwencji, wartości tego parametru dla tego samego obrazu, szacowane różnymi metodami, są zbliżone, lecz nie identyczne. Poza tym, w różny sposób może być określany zakres estymacji nachylenia linii regresji, co ma wpływ na wartość szacowanego parametru. W przyszłych badaniach należy także uwzględnić wpływ zmian wielkości oraz pozycji ROI na wyniki klasyfikacji. Pomimo zasygnalizowanych problemów, analiza fraktalna wydaje się być interesującym narzędziem ekstrakcji wektora cech w badaniach tekstur obrazów CT kręgosłupa.

3.4 *Wpływ normalizacji obrazów CT kręgosłupa na istotność cech teksturalnych w identyfikacji ubytków w strukturze tkanki gąbczastej*

W artykule *The Influence of the Normalisation of Spinal CT Images on the Significance of Textural Features in the Identification of Defects in the Spongy Tissue Structure* (***Róża Dzierżak****, Zbigniew Omiotek, Ewaryst Tkacz, Andrzej Kępa)* przedstawiono wpływ procesu normalizacji obrazu CT kręgosłupa na dokładność rozpoznawania ubytków w strukturze tkanki gąbczastej kręgów na odcinku piersiowo-lędźwiowym.

Obrazy pochodzące ze współczesnych tomografów, w porównaniu z innymi technikami obrazowania medycznego, charakteryzują się dużą dokładnością, wysoką rozdzielczością i kontrastem. Dzięki dobrej jakości otrzymywanych wyników możliwa jest analiza tekstury tkanek. Ma ona na celu znalezienie zbioru parametrów, nazywanych cechami teksturalnymi, z których każdy jest liczbową miarą określonej właściwości tekstury. Do uzyskania jak

najlepszych informacji na temat badanej tkanki konieczne jest odpowiednie dobranie działań z zakresu przetwarzania wstępnego. W niniejszym artykule przedstawiono wpływ procesu normalizacji obrazu na zmiany jego istotnych cech teksturalnych.

Deskryptory cech oparte były na histogramie poziomów szarości, macierzy gradientu, macierzy RL, macierzy zdarzeń, modelu autoregresji i transformacie falkowej. Zastosowano 6 metod selekcji cech: współczynnik Fishera, minimalizacja prawdopodobieństwa błędu klasyfikacji i średnich współczynników korelacji pomiędzy wybranymi cechami, korelację Spearmana, wzajemną informację, heurystyczną identyfikację zmiennych zakłócających, liniową regresję krokową. Każda z pięciu pierwszych metod selekcji zwróciła 10 cech zajmujących początkowe miejsca w rankingu wykonanym według własnego współczynnika. Szósta metoda, tj. liniowa regresja krokowa, zwróciła 6 cech dla obrazów przed normalizacją i 7 cech dla obrazów po wykonaniu tej operacji. Zestawy cech wyłonione w procesie selekcji poddano ewaluacji za pomocą sześciu popularnych metod klasyfikacji nadzorowanej. Były to: liniowa i kwadratowa analiza dyskryminacyjna, naiwny klasyfikator Bayesa, drzewo decyzyjne, klasyfikator *K* najbliższych sąsiadów i lasy losowe. Do oceny dokładności klasyfikatorów zastosowano: dokładność klasyfikacji (ACC), czułość (TPR), specyficzność (TNR), wartość predykcyjną dodatnią (PPV) i wartość predykcyjną ujemną (NPV). Uzyskano następujące wartości poszczególnych współczynników jakości klasyfikacji (przed normalizacją / po normalizacji): ogólna dokładność klasyfikacji – 90%/82%, wrażliwość klasyfikacji – 89%/85%, specyficzność klasyfikacji – 96%/82%, wartość predykcyjna dodatnia – 95%/95%, wartość predykcyjna ujemna – 89%/84%.

Przeprowadzenie normalizacji badanych obrazów spowodowało zmianę jasności poszczególnych pikseli. W efekcie, zmieniły się cechy teksturalne obrazów, co pokazały wyniki analizy. Zestawy deskryptorów, uzyskane jako efekt działania wybranych metod selekcji, były różne dla obrazów przed i po normalizacji. Poszczególne zbiory cech oceniono pod kątem dokładności automatycznej klasyfikacji obrazów na przypadki kategorii zdrowy i chory na osteoporozę. Prawie każdy z zastosowanych współczynników jakości klasyfikacji osiągnął większą wartość dla obrazów bez normalizacji jasności. Różnice w pogorszeniu dokładności, w wyniku przeprowadzenia normalizacji, wynosiły od 4% dla współczynnika TPR do 14% dla ACC. Wyjątkiem był współczynnik PPV, który nie zmienił się w efekcie normalizacji.

Uzyskane wyniki pokazały, że należy ostrożnie dobierać operacje przetwarzania wstępnego, gdyż nie zawsze prowadzą one do poprawy zamierzonych efektów. Normalizacja, rozszerzając zakres odcieni do maksymalnego dopuszczalnego, poprawia jakość obrazu, dzięki czemu

można łatwiej rozróżnić występujące na nim szczegóły. Jednak, jak pokazały badania, może dojść do utraty informacji istotnej z punktu widzenia rozpoznawania tekstur. Dla zastosowanych deskryptorów cech oraz metod klasyfikacji, normalizacja obrazów CT kręgosłupa doprowadziła do pogorszenia dokładności automatycznego rozpoznawania osteoporozy. W związku z tym, operacji tej nie należy rekomendować do stosowania w kontekście zaprezentowanych badań.

4. WYKAZ PUBLIKACJI STANOWIĄCYCH ROZPRAWĘ DOKTORSKĄ

Niniejsza praca oparta jest o cykl publikacji i przedstawia opublikowane wyniki badań nad analizą obrazów TK kręgu lędźwiowego z wykorzystaniem najbardziej efektywnych metod analizy i klasyfikacji obrazów jakie możemy znaleźć w literaturze. Temat diagnostyki osteoporozy jest niezwykle istotny co znajduje potwierdzenie w licznych pracach publikowanych w tej tematyce. Podstawą niniejszej rozprawy są cztery publikacje zawarte w kolejnych podrozdziałach.

4.1 *Comparison of the classification results accuracy for CT soft tissue and bone reconstructions in detecting the porosity of a spongy tissue*

Autorzy: **Róża Dzierżak**, Zbigniew Omiotek, Ewaryst Tkacz and Sebastian Uhlig
Opublikowano: Journal of Clinical Medicine.- 2022, vol. 11, nr 15, s. 1−11.
DOI: https://doi.org/10.3390/jcm11154526

Impact Factor: **4.964**

Liczba punktów ministerialnych: **140**

Udział pierwszego autora w poniżej załączonym artykule polegał na opracowaniu koncepcji badań, analizie literaturowej, analizie otrzymanych wyników, przygotowaniu manuskryptu oraz pracach publikacyjnych (50%). Wkład współautorów, w formie oświadczenia, zamieszczono na końcu artykułu.

Celem badań prezentowanych w niniejszym artykule było porównanie dokładności wyników klasyfikacji dwóch typów rekonstrukcji tkanek miękkich i kości tomografii komputerowej kręgosłupa w wykrywaniu porowatości tkanki gąbczastej. Deskryptory cech tekstury zostały obliczone na podstawie analizy statystycznej histogramu obrazu szarości, modelu autoregresji i transformacji falkowej. Redukcję wymiarów danych zastosowano poprzez selekcję cech przy użyciu dziewięciu metod reprezentujących różne podejścia (filtr, opakowanie i metody osadzone). W przypadku obrazów rekonstrukcji kości cztery modele osiągnęły maksymalną dokładność 92%, z czego jeden miał najwyższą czułość 95%, przy swoistości 89%. W przypadku obrazów rekonstrukcji tkanek miękkich pięć modeli osiągnęło najwyższą dokładność testową wynoszącą 95%, podczas gdy pozostałe wskaźniki jakości (TPR i TNR) również wyniosły 95%. Badania wykazały, że obrazy pochodzące z rekonstrukcji tkanek miękkich pozwalają na uzyskanie dokładniejszych wartości parametrów tekstury, co zwiększa dokładność klasyfikacji i daje lepsze możliwości diagnozowania osteoporozy.

Journal of
Clinical Medicine

MDPI

Article

Comparison of the Classification Results Accuracy for CT Soft Tissue and Bone Reconstructions in Detecting the Porosity of a Spongy Tissue

Róża Dzierżak [1,*], Zbigniew Omiotek [1], Ewaryst Tkacz [2] and Sebastian Uhlig [3]

[1] Department of Electronics and Information Technology, Lublin University of Technology, ul. Nadbystrzycka 38 A, 20-618 Lublin, Poland; z.omiotek@pollub.pl
[2] Department of Biosensors and Processing of Biomedical Signals, Silesian University of Technology, ul. Roosevelta 40, 44-800 Zabrze, Poland; etkacz@polsl.pl
[3] Department of Medical Radiology, Medical University of Lublin, ul. Jaczewskiego 8, 20-090 Lublin, Poland; sebastian.uhlig@icloud.com
* Correspondence: r.dzierzak@pollub.pl

Abstract: The aim of the study was to compare the accuracy of the classification pertaining to the results of two types of soft tissue and bone reconstructions of the spinal CT in detecting the porosity of L1 vertebral body spongy tissue. The dataset for each type of reconstruction (high-resolution bone reconstruction and soft tissue reconstruction) included 400 sponge tissue images from 50 healthy patients and 50 patients with osteoporosis. Texture feature descriptors were calculated based on the statistical analysis of the grey image histogram, autoregression model, and wavelet transform. The data dimensional reduction was applied by feature selection using nine methods representing various approaches (filter, wrapper, and embedded methods). Eleven methods were used to build the classifier models. In the learning process, hyperparametric optimization based on the grid search method was applied. On this basis, the most effective model and the optimal subset of features for each selection method used were determined. In the case of bone reconstruction images, four models achieved a maximum accuracy of 92%, one of which had the highest sensitivity of 95%, with a specificity of 89%. For soft tissue reconstruction images, five models achieved the highest testing accuracy of 95%, whereas the other quality indices (TPR and TNR) were also equal to 95%. The research showed that the images derived from soft tissue reconstruction allow for obtaining more accurate values of texture parameters, which increases the accuracy of the classification and offers better possibilities for diagnosing osteoporosis.

Keywords: osteoporosis; soft tissue reconstruction; bone reconstruction; texture analysis; classification

Citation: Dzierżak, R.; Omiotek, Z.; Tkacz, E.; Uhlig, S. Comparison of the Classification Results Accuracy for CT Soft Tissue and Bone Reconstructions in Detecting the Porosity of a Spongy Tissue. *J. Clin. Med.* **2022**, *11*, 4526. https://doi.org/10.3390/jcm11154526

Academic Editor: Gerald Atkins

Received: 12 June 2022
Accepted: 31 July 2022
Published: 3 August 2022

1. Introduction

A CT image is obtained through transformations and mathematical calculations performed during the measurement process. They are based on an attempt to recreate the damping of a radiation beam in an object through a series of measurements. The process of transforming the primary data into a CT image is known as reconstruction. In order to form a CT image, a computer system assigns a single value in Hounsfield (HU) scale to each pixel. The obtained radiodensity values are a mean from the weakening of radiation beams going through a given point [1–3]. Due to the diversity of the structures in the human body, it is necessary to employ various reconstruction filters. While assessing the condition of organs with a high contrast of internal structures, e.g., bones or lungs, the high-resolution bone reconstruction ("hard kernel" algorithm) is carried out, which enhances the edge quality. In the assessment of soft tissues or organs with lower contrast of internal structures, the soft tissue reconstruction ("soft kernel" algorithm) is employed, which reduces noise at the expense of lowering the spatial resolution. Owing to the application of various reconstruction filters, adjustment of the image for further analyses is possible [4,5].

One of the methods for determining the condition of the analyzed tissue is texture analysis [6]. Although this method can be successfully used in many diagnostic processes, new applications are still being sought, which is indicated by numerous scientific publications [7–18]. This paper presented the process for the classification of spongy matter images in the L1 lumbar vertebra on the basis of the obtained texture properties. The spongy matter is considered bone tissue; however, their lamellae are arranged loosely, and their mineralization level is approximately a third of that in compact bone. Decreasing the mineral density of the spongy matter leads to porosis, initially in the form of osteopenia and then osteoporosis [19–21]. Dual-energy X-ray Absorptiometry (DXA), based on the measurement of bone density, is a commonly employed method for diagnosing osteoporosis. The mineral content in bones governs the number of minerals in the measurement spot, which is divided by the surface, yielding bone mineral density (BMD). Therefore, this technique provides information on the mineral density of the entire examined region without the precise determination of the segment with deficiencies. The index T corresponding to the standard deviation from the reference mineral density is used to classify a patient as healthy or ill. The T = −1 value is considered to be normal; ranges of −1 to 2.4 corresponds to osteopenia, while −2.5 and less are recognized as osteoporosis. Reduced bone mineral density (BMD) identified through DXA requires differential diagnosis to determine its causes. The blood tests and urinalyses are conducted for this purpose [22–24].

The course of osteoporosis is symptomless in its early stages. It is usually diagnosed in the advanced stage, when osteoporotic fractures may occur, even without injuries. Therefore, preventive examinations, aiming at detecting the condition at an early stage and mitigating its consequences, are essential [22,24]. For this reason, new diagnostic solutions enabling the diagnosis of osteoporosis at an early stage are being sought. The literature contains descriptions of numerous experiments connected to seeking methods for identifying lesions in bone regions. Mustapha et al. [25,26] and Stanley et al. [27] presented the method for identifying lesions in neck vertebrae. Mustapha et al. [25] describe a method for AOs (classes and severity) classification of cervical radiography by designing a fuzzy decision tree (FDT) model. The results obtained on a set of 400 cervical vertebrae radiography images indicate the classification rate of 93.09%. Stanley et al. [27], based on the size invariant descriptor (SID), *K*-means (Km), and nearest neighbor methods (NN), the obtained classification rate reached 84.44%. In turn, Mustapha et al. in [26] the employing region-based (RB) fracture characterization as well as five-fold cross-validation (5FCV), and an efficiency of 87.58% was achieved. Lespessailles et al. [28] show clinical interest in bone texture analysis with a new high-resolution X-ray device. The studies indicated that the combination of BMD and texture parameter values provided a better assessment of the fracture risk than that obtainable solely by BMD measurement. The texture analysis also found an application in the diagnostic of pelvic bones, which was described in [29] by Gaidel et al. It was demonstrated that the covariance features were the most efficient—the diagnostic error probability of 0.2 was obtained. Similar findings were also presented in Chappard et al. [30] and Lespessailles et al. [31]. These works also demonstrated the relationship between BMD and texture parameters.

During the assessment of the spongy matter, both by radiologists during the standard diagnostic assessment and in the majority of papers on this subject [32,33], the images from bone reconstruction are used. Due to the atypical character of the spongy matter, which was mentioned above, two types of image reconstruction were employed, i.e., soft and hard kernel reconstruction. The main aim of the study was to verify which type or reconstructed images enable obtaining the texture and allow for a more precise classification of the tissue condition.

2. Materials and Methods

2.1. Material

The imaging examinations considered in the paper were carried out in a hospital (Samodzielny Szpital Kliniczny nr 4) in Lublin. Patients were referred to the lumbosacral

spine examination from an orthopaedic clinic and ER. The examination involved the analysis of the lumbosacral spine CT of 100 patients. The control group comprised 50 individuals without the symptoms of osteoporosis or osteopenia. The same number of patients constituted the group of people with osteoporosis. The control group included 26 women and 24 men aged 53 to 77. Each of the patients was examined by means of 32-row CT by GE in a standard protocol for lumbosacral spine examinations. The examination was performed in the spiral acquisition and assessed using multi-surface and three-dimensional reconstructions. The layers of the soft kernel and hard kernel reconstructions corresponded were 2.5 mm and 1.25 mm, respectively. The exposure parameters were adjusted in the range from 85 mA to 700 mA (median = 181) for the intensity and two values—120 kV or 140 kV in the case of voltage.

The assignment of patients to both groups was performed on the basis of the radiology report and the measurement of radiological densities of the spongy matter of the first vertebra of the lumbar spine (L1). On the basis of the literature [34], the border value of tissue density of 120 Hounsfield Units (HU) was assumed. The patients in whom the density was greater than the limit value and the report did not indicate lesions in the spongy matter were assigned to the control group (HEALTHY class). In turn, the patients who did not meet the criteria were assigned to the osteoporotic group (OSTEOPOROSIS class).

2.2. Image Preprocessing

The source data saved in the DICOM standard contained RGB images in the 512 × 512 resolution. The images which show the interior of the vertebra along with the spongy matter were selected (Figure 1).

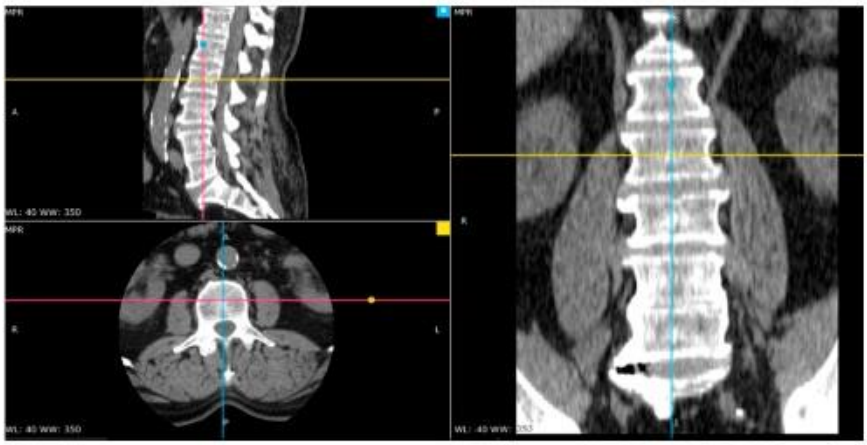

Figure 1. The arrangement of the axis in the center of one of the vertebrae (image in three projections).

The images on the same vertebra level were selected for soft tissue and bone reconstruction. Since the thickness of layers for bone reconstruction was halved, every other layer of a given vertebra cross-section was analyzed. The images selected for further studies were saved in BMP format and converted from 24-bit RGB to 8-bit greyscale. The extraction of the regions of interest (ROI) was performed manually (Figure 2). The size of the extracted samples was selected to use the textured surface, potentially containing the information in the image of the transverse vertebra section, to the maximum extent. This resulted in samples with a size of 50 × 50 pixels (Figure 3).

During the preprocessing, the image histogram normalization process was omitted because the available results indicate that this operation deteriorates the classification accuracy in the range from 4% for the TPR coefficient (classification sensitivity) to 14% for ACC (overall classification accuracy) [35].

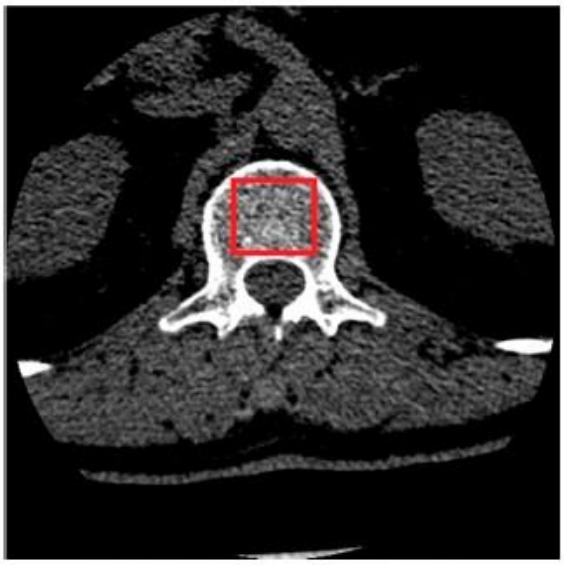

Figure 2. Manual selection of the spongy matter region.

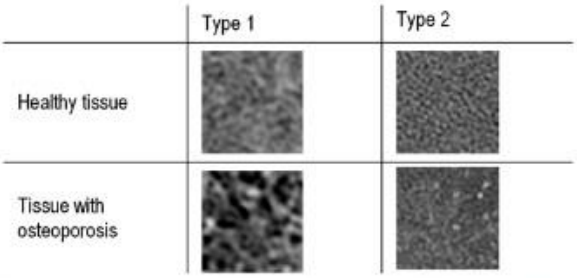

Figure 3. Spongy matter structure in soft-tissue (Type 1) and bone reconstruction (Type 2).

2.3. Estimation of Texture Parameters

The prepared samples were subjected to tissue image texture analysis. The image analysis was conducted using the MaZda software (version 4.6) developed in the Institute of Electronics of Lodz University of Technology (Lodz, Poland) [36]. This software was made available online for free for scientific purposes. It enables the analysis of greyscale texture images and indicates the numerical values of the image features. A detailed description of these features can be found in [37–40], as well as in the MaZda manual. The advantage of this software is the fact that apart from the statistical approach to the image analysis, it also employs a mathematical model (autoregression model) and a transformation approach (wavelet transform).

The set of features has been obtained on the basis of:

- Histogram (9 features): histogram mean, histogram variance, histogram skewness, histogram kurtosis, percentiles 1%, 10%, 50%, 90%, and 99%;
- Gradient (5 features): absolute gradient mean, absolute gradient variance, absolute gradient skewness, absolute gradient kurtosis, percentage of pixels with a nonzero gradient;
- Run length matrix (5 features × 4 various directions): run length nonuniformity, grey level nonuniformity, long run emphasis, short run emphasis, the fraction of image in runs;
- Co-occurrence matrix (11 features × 4 various directions × 5 between-pixels distances) angular second moment, contrast, correlation, sum of squares, inverse difference

moment, sum average, sum variance, sum entropy, entropy, difference variance, difference entropy;
- Autoregressive model (5 features): parameters Θ1, Θ2, Θ3, Θ4, standard deviation.
- Haar wavelet (24 features): wavelet energy (features are computed at 6 scales within 4 frequency bands LL, LH, HL, and HH).

The available research results show that the textural features obtained with the above-mentioned methods allowed for high classification accuracy of the ultrasound and radiographic images [41,42].

2.4. Data Preprocessing

Two sets of observations were used in the studies; the first contained the images produced through bone reconstruction, while the other used those from soft-tissue reconstruction. For both types of reconstruction, a full set comprised 400 observations, 200 per class. At the beginning of preprocessing, both sets were divided randomly into learning and testing sets. The division was performed in such a way that 70% constituted the learning set and 30%—the test set. As a result, the learning set comprised 280 observations (137 healthy cases and 143 osteoporosis cases), while the test set involved 120 observations (63 healthy cases and 57 osteoporosis cases).

Due to the fact that the feature descriptors were measured at different scales (interval scale, ratio scale), the features were scaled through standardization [43]:

$$z_{ij} = (x_{ij} - \overline{x}_j)/s_j,$$

where x_{ij}—value of feature j for observation i; z_{ij}—standardized value for feature j for observation i; $\overline{x}_j$—arithmetical mean for feature j; s_j—standard deviation for feature j. Following standardization, the interval measurement scale and normal distribution N(0, 1) were used for all features. Scaling was performed once for the learning data. Then, the test sets were transformed in a similar manner. The vectors of mean values and variance obtained during the standardization of learning sets were used for each feature.

In the following step, the four-stage data cleansing procedure was carried out:

1. Removal of features with constant values (variance equal to 0).
2. Removal of features with nearly constant values (variance lower than 0.01).
3. Removal of duplicated features.
4. Removal of correlated features

The Pearson correlation coefficient (r), which detects linear dependencies and assumes the normality of their distribution, was employed. The features for which $|r| > 0.9$—indicating strong correlation—were removed.

As a result of data cleansing, the number of features was reduced from 290 to 32 for the bone reconstruction and from 290 to 18 for the soft-tissue reconstruction. The data preprocessing was carried out with the *scikit-learn* library and Python programming language, which was also employed in the further stages of the study.

2.5. Data Reduction

The study involved the reduction of the data through feature selection. Generally, the aim of the selection is to limit the initial (complete) set of features to a certain subset, containing the features that are important from the point of view of the applied criterion. In the course of the data cleansing process, the complete set of 290 features was greatly reduced—to 32 for bone reconstruction and 18 for soft-tissue reconstruction. This mainly had an influence on the occurrence of features with a strong correlation ($|r| > 0.9$). Therefore, the additional reduction was omitted, and the creation of a ranking list by each of the employed methods was set as a goal. The ranking list contained a set of features in the order reflecting their significance in terms of discrimination of observations belonging to different classes. The choice of an optimal number of features for each of the employed selection methods was made in the following stage, which involved training the classification model.

In order to avoid overtraining the classifiers, the selection of features was carried out only in relation to the training sets. Then, its results were employed for the transformation of test sets. The selection of features was performed with *scikit-learn*, *scikit-feature*, *ReliefF*, *MLxtend*, and *LightGBM* libraries.

Nine methods belonging to the three following groups were used:

1. Filter methods:
   - Univariate—Fisher's method (FISHER) and variance analysis method (ANOVA);
   - Multivariate—Relief method (RELIEF).
2. Wrapper methods:
   - Sequential Forward Selection (SFS);
   - Sequential Backward Selection (SBS);
   - Recursive Feature Elimination along with LogisticRegression estimator (RFE).
3. Embedded methods:
   - SelectFromModel meta-transformer and logistic regression estimator (LR);
   - SelectFromModel meta-transformer and AdaBoost estimator (ADA);
   - SelectFromModel meta-transformer along with LightGBM estimator (LGBM).

2.6. Training the Classification Models

The training of the classification models aimed to obtain the most efficient model as well as an optimal subset of features for each of the employed selection methods. In the course of this process, the number of features of the learning set changed in accordance with the ranking list. For bone reconstruction, the number of features changed from 2 to 32, except for the methods employing the logistic regression model and AdaBoost model, for which the number of features changed from 2 to 12. In the case of soft-tissue reconstruction, the number of features changed from 2 to 18. The exceptions included the methods based on the logistic regression model and AdaBoost model, for which the number of features changed from 2 to 5 and from 2 to 9, respectively. In the training process, optimal hyperparameter values for a given model were determined in accordance with the grid search method. The GridSearchCV method was employed for this purpose, available in the model_selection module of the scikit-learn library. The model assessment was carried out on the basis of 10-fold cross-validation. Each model considered optimal for a given number of features was saved as a file on the disc. Then, the best model, i.e., the one which ensured the highest classification accuracy at a minimum number of features, was selected from this set. The selection of the best model enabled the unequivocal determination of the optimal set of features that were applied by that model. The above-mentioned procedure was employed for all filter and wrapper methods. In the case of the embedded methods, only the classifiers employed in the selection process were built and adjusted.

Eleven classification methods were used for the features selected by means of the filter and wrapper methods. They were: linear and quadratic discriminant analysis (LDA, QDA), gaussian naive Bayes (BAYES), support vector machines (SVM) that uses regularization parameter C), support vector machines (NuSVM) that uses a parameter to control the number of support vectors nu), *K*-nearest neighbors (KNN), decision tree (DT), multi-layer perceptron (MLP) and three ensemble methods—random forest (RF), gradient boosting (GRAD), AdaBoost (ADA). In turn, three classification methods have been used for the features selected by means of the embedded methods: AdaBoost, logistic regression (LR), and LightGBM (LGBM). All algorithms of the applied machine learning methods (except LightGBM) are implemented in the scikit-learn library.

Figure 4 presents an exemplary course of model learning and validation for the set of features obtained with the Fisher method for soft-tissue reconstruction. In turn, Table 1 shows the exemplary results of hyperparametric optimization with the grid search method for the Fisher method and the same type of reconstruction.

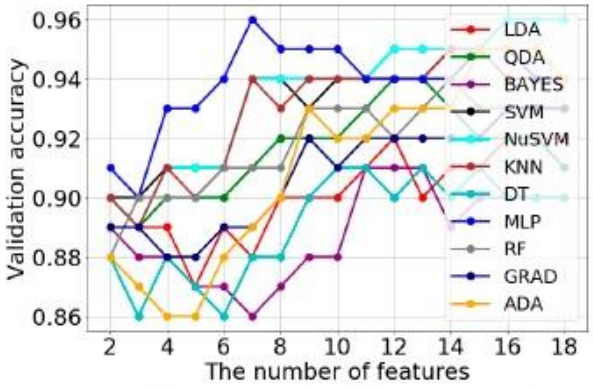

Figure 4. Exemplary process of the model learning and validation for a set of features obtained with the Fisher method (soft-tissue reconstruction) for different classification methods. The graph shows that—for instance—the optimal number of features for the MLP model is 7.

Table 1. Results of hyperparametric optimization with the grid search method for the set of features obtained with the Fisher method (soft-tissue reconstruction). The criterion assumed for the selection of an optimal model for a given classification method involved achieving maximum validation accuracy with minimum number of training set features. The grey background was used to emphasize the model, which proved the best among the employed classification methods for the Fisher method. The meaning of parameters of individual classification models can be found in the scikit-learn library documentation [44].

Classification Method	Validation Accuracy	Optimal Features Number	Optimal Model Parameters
LDA	0.92	12	*solver* = 'svd'
QDA	0.94	12	$tol = 1 \times 10^{-5}$
BAYES	0.91	11	*var_smoothing* = 0.1
SVM	0.96	16	*C* = 1.0, *gamma* = 'scale', *kernel* = 'rbf'
NuSVM	0.96	16	*gamma* = 'scale', *kernel* = 'rbf', *nu* = 0.3
KNN	0.95	14	*n_neighbors* = 5
DT	0.91	10	*criterion* = 'gini', *max_depth* = 3
MLP	0.96	7	*activation* = 'relu', *alpha* = 0.1, *solver* = 'lbfgs', *max_iter* = 1000, *hidden_layer_sizes* = (3,)
RF	0.94	14	*max_depth* = 5, *n_estimators* = 20
GRAD	0.93	16	*loss* = 'deviance', *n_estimators* = 50
ADA	0.95	15	*n_estimators* = 50

The exemplary results in Table 1 indicate that the highest validation accuracy (0.96) is provided by the SVM, NuSVM, and MLP models. However, due to the lowest number of the training set features (7), the MLP model was assumed as the best for the set of features obtained with the Fisher method (grey background).

3. Results

Table 2 shows the complete results pertaining to the selection of the optimal models for all feature selection methods and both types of reconstruction. The information in the table contains the symbols of the employed classification method and the selection method applied for building the feature ranking, as well as the number of features used for model construction and its validation accuracy.

Table 2. Basic information about optimal models for particular feature selection methods.

Model Number	Bone Reconstruction				Soft Tissue Reconstruction			
	Classification Method	Feature Selection Method	The Number of Features	Validation Accuracy (%)	Classification Method	Feature Selection Method	The Number of Features	Validation Accuracy (%)
1	NuSVM	FISHER	13	94	MLP	FISHER	7	96
2	RF	ANOVA	26	94	NuSVM	ANOVA	17	96
3	SVM	RELIEF	27	94	MLP	ANOVA	17	96
4	NuSVM	SFS	6	94	SVM	RELIEF	18	96
5	KNN	SBS	9	94	NuSVM	RELIEF	18	96
6	RF	SBS	9	94	KNN	SFS	5	96
7	MLP	RFE	18	95	KNN	SBS	5	96
8	ADA		9	93	SVM	RFE	18	96
9	LR		10	93	NuSVM	RFE	18	96
10	LGBM		3	89	ADA		8	95
11					LR		4	91
12					LGBM		2	88

The evaluation of the optimal methods was carried out through independent test sets. As a result, the most efficient selection method, optimal feature subset indicated with this method, and the best classifiers were obtained. The applied classification quality measures included overall accuracy (ACC), true positive rate (TPR), and true negative rate (TNR). For bone reconstruction (Figure 5a), the highest accuracy (ACC = 92%) was obtained by models no. 1, 2, 3, and 5 (Table 2), at the same validation accuracy of 94%. In the case of the soft-tissue reconstruction (Figure 5b), the highest accuracy (ACC = 95%) was obtained for models no. 2, 4, 5, 8, and 9 (Table 2). The validation accuracy for these models amounted to 96%.

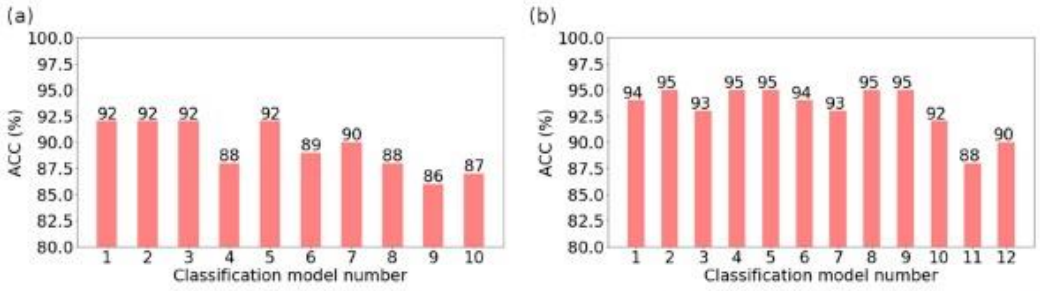

Figure 5. Results of testing the models considered optimal for particular feature selection methods: (**a**) bone reconstruction; (**b**) soft tissue reconstruction.

Figure 6 shows more information on the model evaluation results. Apart from the total classification accuracy, it also presents the true positive rate (sensitivity) and true negative rate (specificity). In the case of bone reconstruction, Figure 6a shows the value of TPR and TNR for models no. 1, 2, 3, and 5, for which ACC = 92%. In turn, for the soft-tissue reconstruction (Figure 6b), the information on TPR and TNR pertains to models no. 2, 4, 5, 8, and 9, which achieved ACC = 95%. In the case of the same ACC value, the TPR value was assumed as the criterion for the selection of the best model due to the medical benefits of such an approach. Therefore, model no. 5 turned out to be the most efficient in bone reconstruction, achieving a TPR of 95%. This model was built with the *K*-nearest neighbors method (for $K = 1$), employing nine features obtained with the SBS method. In the case of soft-tissue reconstruction, all models (2, 4, 5, 8, and 9) were similarly effective. They achieved the same values of TPR and TNR indices, equal to 95%. Detailed data on the

structure of the models are presented in Table 3, whereas the confusion matrices of the most effective models for both types of reconstruction are presented in Figure 7.

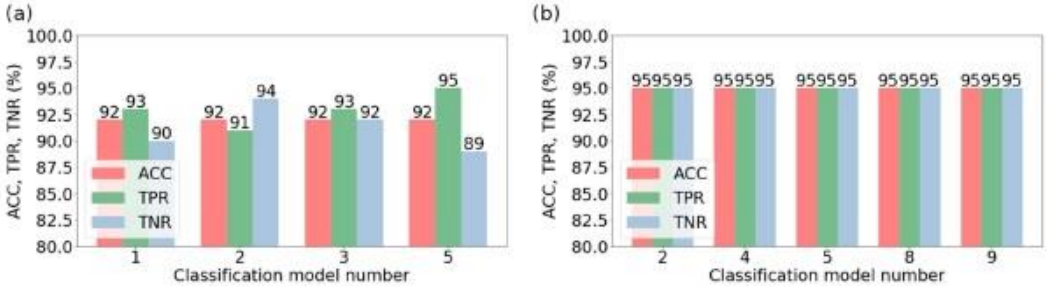

Figure 6. The sensitivity (*TPR*) and specificity (*TNR*) of the models that have reached the highest value of the overall classification accuracy (*ACC*): (**a**) bone reconstruction; (**b**) soft-tissue reconstruction.

Table 3. Information on the structure of models considered most effective for soft-tissue reconstruction.

Model Number	Classification Method	Feature Selection Method	The Number of Features	Model Parameters
2	NuSVM	ANOVA	17	*gamma* = 'scale', *kernel* = 'rbf', *nu* = 0.3
4	SVM	RELIEF	18	*C* = 1.0, *gamma* = 'scale', *kernel* = 'rbf'
5	NuSVM	RELIEF	18	*gamma* = 'scale', *kernel* = 'rbf', *nu* = 0.3
8	SVM	RFE	18	*C* = 1.0, *gamma* = 'scale', *kernel* = 'rbf'
9	NuSVM	RFE	18	*gamma* = 'scale', *kernel* = 'rbf', *nu* = 0.3

The meaning of the model parameters in Table 3: *gamma*—kernel coefficient; *kernel*—specifies the kernel type to be used in the algorithm; *nu*—an upper bound on the fraction of training errors and a lower bound of the fraction of support vectors; *C*—regularization parameter. The other model parameters, not listed in Table 3, take default values.

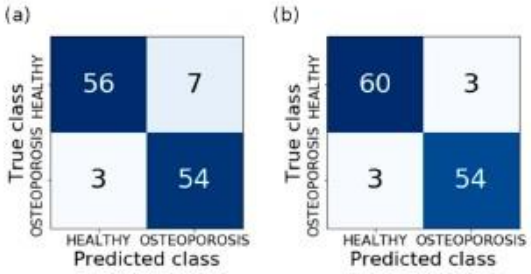

Figure 7. Confusion matrices: (**a**) model 5 for bone reconstruction; (**b**) models 2, 4, 5, 8 and 9 for soft tissue reconstruction.

4. Discussion

The quality of the built models should be assessed as high. In the case of bone reconstruction, four models (1, 2, 3, and 5) achieved the maximum accuracy for the test set (*ACC* = 92%); model no. 5 was characterized by the greatest sensitivity (*TPR* = 95%) at specificity *TNR* = 89%. In turn, for the soft-tissue reconstruction, the highest accuracy (*ACC* = 95%) was obtained for five models (2, 4, 5, 8, and 9). The remaining quality indices of these models, i.e., *TPR* and *TNR*, were equal to 95%. It should be emphasized that for both types of reconstruction, the majority of the models are characterized by relatively high validation accuracy. In turn, for the best models, the testing accuracy is only slightly lower than the validation accuracy. For bone reconstruction, this difference amounts only to 2%, and for soft-tissue reconstruction—1%. Such a situation indicates high quality, both of the models themselves, as well as the data used in the course of their training. The disadvantage of this method is that the extraction of the regions of interest was carried

out manually. However, this problem requires separate investigations; therefore, it will be the topic of further research. The obtained results were compared with the results from the papers on a similar matter conducted by other authors (Table 4). Taking into account the total classification accuracy (*ACC*), it can be seen that the obtained result is one of the highest and is only 1.6% lower than the results achieved in [45,46], where it amounted to 96.6%. However, the majority of results presented in the table are much lower, and in the case of Andersen et al. [47], it amounts only to 71.3%. Other parameters also approximate the best results. While analyzing the data, it can be stated that the presented method stands out from similar investigations and exhibits high diagnostic potential.

Table 4. Summary of results of similar bone texture analysis tests [48].

No. in Ref.	Texture Features	ROI Segmentation	Dataset	Classifier	*TPR*	*TNR*	*PPV*	*NPV*	*ACC*	F1-Score
Own results	Histogram, Gradient, Run length matrix, Cooccurrence, Autoregressive, Haar wavelet	Manual	50 cases & 50 controls	SVM NuSVM	95	95	-	-	95	-
[49]	power spectral density, triangular prism surface area and variation, box counting,	Manual	11 cases & 13 controls	K-NN	78	90	90	77	81	-
[50]	Wavelet Marginals-Haar	Calcaneal (Manual)	58 cases & 58 controls	SVM	62.1	65.5	64.3	63.3	63.8	63.2
[51]	1D LBP	Calcaneal (Manual)	39 cases & 41 controls	KNN	-	43.9	-	-	71.3	77.2
[47]	Fractal dimension, wavelet analysis, Gabor, LBP, DFT, DCT, Laws masks, edge histogram and GLCM	Calcaneal (Manual)	58 cases & 58 controls	RF	74.1	74.1	-	-	74.1	-
[52]	1D projection modeled as fractional Brownian motion	Calcaneal (Manual)	-	SVM	96.9	97.6	-	-	94.5	94.3
[45]	Fractional Brownian model and Rao geodesic distance	Calcaneal	348 cases & 348 controls	KNN	97.8	95.4	-	-	96.6	96.5
[46]	Histogram and GLCM and PCA analysis	Calcaneal (Manual)	87 cases & 87 controls	SVM	97.7	95.4	95.5	97.7	96.6	96.6
[53]	Anisotropic discrete dual-tree wavelet transform	Calcaneal (Manual)	87 cases & 87 controls	SVM	-	93.1	92.9	91.0	91.9	91.9
[54]	Wavelet decomposition and parametric circular models	Calcaneal (Manual)	87 cases & 87 controls	SVM	100	92.5	91.9	100	95.9	95.8
[55]	Oriental fractal analysis	Calcaneal (Manual)	87 cases & 87 controls	-	72.0	71.0	72.0	71.0	71.8	72.2
[56]	BMD, fractal, histomorphometric and skeletal measures	Distal radius	87 cases & 87 controls	SVM	79.0	66.0	-	-	-	-
[48]	Cortical, histogram, GLCM and MGM	Distal radius (Automated)	60 cases & 60 controls	SVM	86.7	65.0	71.2	83.0	75.8	78.2

Table 4. *Cont.*

No. in Ref.	Texture Features	ROI Segmentation	Dataset	Classifier	*TPR*	*TNR*	*PPV*	*NPV*	*ACC*	F1-Score
[48]	Cortical and LLBP	Distal radius (Automated)	60 cases & 60 controls	SVM	88.3	66.7	72.6	85.1	77.5	79.7
[48]	Cortical and hLLBP	Distal radius (Automated)	60 cases & 60 controls	LR	81.7	76.7	77.8	80.7	79.2	79.7
[48]	Cortical and vLLBP	Distal radius (Automated)	60 cases & 60 controls	SVM	88.3	60.0	68.8	83.7	74.2	77.4

Figure 8 shows the general scheme of a system for the prediction of new images with the constructed models. Initially, ROI extraction is conducted, and the 24-bit RGB type is changed to an 8-bit greyscale. The next stage is the determination of the feature descriptors, which were significant in the training process. The *K*-NN classifier ($K = 1$), considered the best for bone reconstruction, involves nine features that are obtained with the SBS method. In the case of soft-tissue reconstruction, a set of 17 or 18 features has to be determined in accordance with the applied classifier and selection method (Table 3). Then, the important features were scaled (standardization) with vectors of mean values and variance of features obtained during the scaling of training sets. Classification is the final step. On the basis of the classification model and the values of feature descriptors, the class is assigned to the analyzed image (prediction). Figure 9 shows prospective prediction results for exemplary images obtained through soft-tissue reconstruction. The presented results were obtained with a prototype system for diagnosing osteoporosis, which employs model no. 4 for prediction (Table 3).

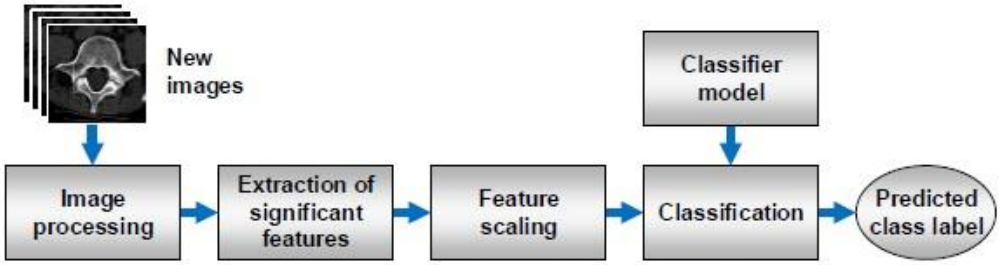

Figure 8. Process flow during the prediction of a class of new images.

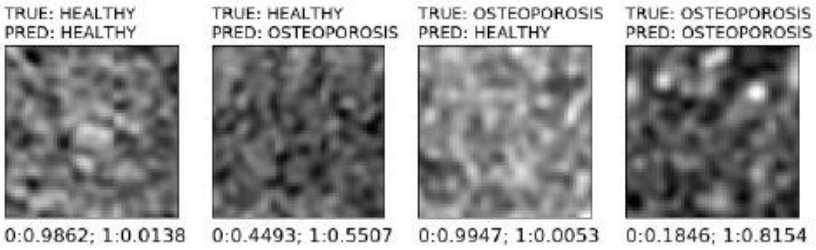

Figure 9. Various prediction results of sample images using soft tissue reconstruction.

5. Conclusions

The results of studies indicate that in the case of texture analysis, soft-tissue reconstruction is characterized by a higher classification accuracy ($ACC = 95\%$) than bone reconstruction ($ACC = 92\%$), which is usually employed for the spongy matter examination. Due to the atypical character of the examined tissue, exhibiting lower mineral density than in compact bone, the image from soft-tissue reconstruction contains a more accurate range

of values pertaining to texture features. In that case, as many as five classifiers obtained the same maximum values of index quality ($ACC = TPR = TNR = 95\%$). This justifies the usefulness of the conducted studies and indicates new possibilities stemming from an alternative approach to the analyzed tissue. The high efficiency of feature selection using the ANOVA, RELIEF, and RFE methods was observed as well. In combination with SVM and NuSVM classifiers, they enable achieving high classification accuracy. Studies showed that while designing a system for the automatic identification of osteoporotic bone fractures based on spinal CT, the application of soft-tissue reconstruction yields better results than bone reconstruction. It achieves 3% better classification accuracy than the traditional approach to the analysis of bone reconstruction images. Further investigations will focus on the development of an algorithm for automatic ROI extraction and testing the system utilizing a greater number of observations.

Author Contributions: Conceptualization, R.D. and S.U.; Data curation, S.U.; Methodology, R.D. and Z.O.; Project administration, R.D.; Software, Z.O.; Validation, R.D.; Visualization, Z.O.; Writing—original draft, R.D. and Z.O.; Writing—review & editing, E.T. All authors have read and agreed to the published version of the manuscript.

Funding: This research was funded by the Ministry of Education and Science—Poland, grant number FD-20/EE-2/302 and FD-20/EE-2/315.

Institutional Review Board Statement: Not applicable.

Informed Consent Statement: Not applicable.

Data Availability Statement: Not applicable.

Conflicts of Interest: The authors declare no conflict of interest.

References

1. Prakash, P.; Kalra, M.K.; Digumarthy, S.R.; Hsieh, J.; Pien, H.; Singh, S.; Gilman, M.D.; Shepard, J.-A.O. Radiation Dose Reduction with Chest Computed Tomography Using Adaptive Statistical Iterative Reconstruction Technique: Initial Experience. *J. Comput. Assist. Tomogr.* **2010**, *34*, 40–45. [CrossRef] [PubMed]
2. Silva, A.C.; Lawder, H.J.; Hara, A.; Kujak, J.; Pavlicek, W. Innovations in CT Dose Reduction Strategy: Application of the Adaptive Statistical Iterative Reconstruction Algorithm. *AJR Am. J. Roentgenol.* **2010**, *194*, 191–199. [CrossRef] [PubMed]
3. Solomon, J.; Samei, E. Quantum Noise Properties of CT Images with Anatomical Textured Backgrounds across Reconstruction Algorithms: FBP and SAFIRE. *Med. Phys.* **2014**, *41*, 091908. [CrossRef] [PubMed]
4. Andersen, A.H. Algebraic Reconstruction in CT from Limited Views. *IEEE Trans. Med. Imaging* **1989**, *8*, 50–55. [CrossRef] [PubMed]
5. Huda, W.; Ogden, K.M.; Samei, E.; Scalzetti, E.M.; Lavallee, R.L.; Roskopf, M.L.; Groat, G.E. Reconstruction Filters and Contrast Detail Curves in CT. In Proceedings of the Medical Imaging 2008: Image Perception, Observer Performance, and Technology Assessment; International Society for Optics and Photonics, San Diego, CA, USA, 6 March 2008; Volume 6917, p. 691710.
6. Shahabaz; Somwanshi, D.K.; Yadav, A.K.; Roy, R. Medical Images Texture Analysis: A Review. In Proceedings of the 2017 International Conference on Computer, Communications and Electronics (Comptelix), Jaipur, India, 1–2 July 2017. [CrossRef]
7. Blair, J.P.; Bierma-Zeinstra, S.; Nielsen, H.B.; Bay-Jensen, A.-C.; Dam, E.B. Texture Analysis of Knee Pathology for the Diagnosis of Radiographic Osteoarthritis. *Osteoarthr. Cartil.* **2018**, *26*, S436. [CrossRef]
8. Fan, J.; Min, B.; Xu, F.; Yang, P.; Ye, H.; Feng, Y.; Shen, Y.; Xu, C.; Zhou, W.; Ren, X. Clinical Diagnosis of Pancreatic Cancer Using Texture Analysis in Endoscopic Ultrasonography. *J. Med. Imaging Health Inform.* **2019**, *9*, 1844–1848. [CrossRef]
9. Fujima, N.; Homma, A.; Harada, T.; Shimizu, Y.; Tha, K.K.; Kano, S.; Mizumachi, T.; Li, R.; Kudo, K.; Shirato, H. The Utility of MRI Histogram and Texture Analysis for the Prediction of Histological Diagnosis in Head and Neck Malignancies. *Cancer Imaging* **2019**, *19*, 5. [CrossRef]
10. Gilanie, G.; Bajwa, U.I.; Waraich, M.M.; Habib, Z. Computer Aided Diagnosis of Brain Abnormalities Using Texture Analysis of MRI Images. *Int. J. Imaging Syst. Technol.* **2019**, *29*, 260–271. [CrossRef]
11. Li, Z.; Yu, L.; Wang, X.; Yu, H.; Gao, Y.; Ren, Y.; Wang, G.; Zhou, X. Diagnostic Performance of Mammographic Texture Analysis in the Differential Diagnosis of Benign and Malignant Breast Tumors. *Clin. Breast Cancer* **2018**, *18*, e621–e627. [CrossRef]
12. Manabe, O.; Ohira, H.; Hirata, K.; Hayashi, S.; Naya, M.; Tsujino, I.; Aikawa, T.; Koyanagawa, K.; Oyama-Manabe, N.; Tomiyama, Y.; et al. Use of 18F-FDG PET/CT Texture Analysis to Diagnose Cardiac Sarcoidosis. *Eur. J. Nucl. Med. Mol. Imaging* **2019**, *46*, 1240–1247. [CrossRef]

13. Mitrea, D.; Nedevschi, S.; Mitrea, P.; Brehar, R.; Vancea, F.I.; Platon(lupșor), M.; Ștefănescu, H.; Badea, R. Advanced Texture Analysis and Classification Methods for the Automatic Diagnosis of the Hepatocellular Carcinoma. *Appl. Med. Inform.* **2019**, *41*, 17–18.
14. WANG Minhong, Z.L.; WANG Minhong, Z.L. Value of Conventional MRI Texture Analysis in Differential Diagnosis of Glioblastomas and Primary Central Nervous System Lymphoma. *China Oncol.* **2019**, *29*, 284–288. [CrossRef]
15. Wang, X.; Suo, S.; Zhu, J.; Feng, Q.; Hua, X.; Wang, W.; Gong, J.; Liu, J.; Lu, Q. Application of intestinal CT texture analysis and nonlinear discriminant analysis in differential diagnosis of colorectal cancer and ulcerative colitis. *J. Shanghai Jiaotong Univ.* **2018**, *38*, 624. [CrossRef]
16. Masci, G.M.; Ciccarelli, F.; Mattei, F.I.; Grasso, D.; Accarpio, F.; Catalano, C.; Laghi, A.; Sammartino, P.; Iafrate, F. Role of CT Texture Analysis for Predicting Peritoneal Metastases in Patients with Gastric Cancer. *Radiol. Med.* **2022**, *127*, 251–258. [CrossRef]
17. Nagawa, K.; Suzuki, M.; Yamamoto, Y.; Inoue, K.; Kozawa, E.; Mimura, T.; Nakamura, K.; Nagata, M.; Niitsu, M. Texture Analysis of Muscle MRI: Machine Learning-Based Classifications in Idiopathic Inflammatory Myopathies. *Sci. Rep.* **2021**, *11*, 9821. [CrossRef]
18. Cavallo, A.U.; Troisi, J.; Forcina, M.; Mari, P.-V.; Forte, V.; Sperandio, M.; Pagano, S.; Cavallo, P.; Floris, R.; Garaci, F. Texture Analysis in the Evaluation of COVID-19 Pneumonia in Chest X-Ray Images: A Proof of Concept Study. *Curr. Med. Imaging Rev.* **2021**, *17*, 1094–1102. [CrossRef]
19. Downey, P.A.; Siegel, M.I. Bone Biology and the Clinical Implications for Osteoporosis. *Phys. Ther.* **2006**, *86*, 77–91. [CrossRef]
20. Marcus, R.; Dempster, D.; Cauley, J.; Feldman, D. *Osteoporosis*, 4th ed.; Academic Press: Cambridge, MA, USA, 2013; ISBN 978-0-12-415853-5.
21. Ebeling, P.R.; Nguyen, H.H.; Aleksova, J.; Vincent, A.J.; Wong, P.; Milat, F. Secondary Osteoporosis. *Endocr. Rev.* **2022**, *43*, 240–313. [CrossRef]
22. Kanis, J.A. Diagnosis of Osteoporosis and Assessment of Fracture Risk. *Lancet* **2002**, *359*, 1929–1936. [CrossRef]
23. Klibanski, A.; Adams-Campbell, L.; Bassford, T.; Blair, S.N.; Boden, S.D.; Dickersin, K.; Gifford, D.R.; Glasse, L.; Goldring, S.R.; Hruska, K.; et al. Osteoporosis Prevention, Diagnosis, and Therapy. *JAMA* **2001**, *285*, 785–795.
24. Orimo, H.; Hayashi, Y.; Fukunaga, M.; Sone, T.; Fujiwara, S.; Shiraki, M.; Kushida, K.; Miyamoto, S.; Soen, S.; Nishimura, J.; et al. Diagnostic Criteria for Primary Osteoporosis: Year 2000 Revision. *J. Bone Miner. Metab.* **2001**, *19*, 331–337. [CrossRef]
25. Mustapha, A.; Hussain, A.; Zulkifley, M.A.; Zaki, W.M.D.W.; Husain, H.; Abdul Hamid, H.B. Anterior Osteoporosis Classification in Cervical Vertebrae Using Fuzzy Decision Tree. *Multimed. Tools Appl.* **2017**, *77*, 4011–4045. [CrossRef]
26. Mustapha, A.; Hussain, A.; Samad, S.; Zulkifley, M.; Diyana Wan Zaki, W.; Hamid, H. Design and Development of a Content-Based Medical Image Retrieval System for Spine Vertebrae Irregularity. *Biomed. Eng. Online* **2015**, *14*, 6. [CrossRef]
27. Stanley, R.J.; Antani, S.; Long, R.; Thoma, G.; Gupta, K.; Das, M. Size-Invariant Descriptors for Detecting Regions of Abnormal Growth in Cervical Vertebrae. *Comput. Med. Imaging Graph.* **2008**, *32*, 44–52. [CrossRef] [PubMed]
28. Lespessailles, E.; Gadois, C.; Kousignian, I.; Neveu, J.P.; Fardellone, P.; Kolta, S.; Roux, C.; Do-Huu, J.P.; Benhamou, C.L. Clinical Interest of Bone Texture Analysis in Osteoporosis: A Case Control Multicenter Study. *Osteoporos. Int.* **2008**, *19*, 1019–1028. [CrossRef]
29. Gaidel, A.; Khramov, A. Application of Texture Analysis for Automated Osteoporosis Diagnostics by Plain Hip Radiography. *Pattern Recognit. Image Anal.* **2015**, *25*, 301–305. [CrossRef]
30. Chappard, D.; Pascaretti-Grizon, F.; Gallois, Y.; Mercier, P.; Baslé, M.F.; Audran, M. Medullar Fat Influences Texture Analysis of Trabecular Microarchitecture on X-Ray Radiographs. *Eur. J. Radiol.* **2006**, *58*, 404–410. [CrossRef]
31. Lespessailles, E.; Gadois, C.; Lemineur, G.; Do-Huu, J.P.; Benhamou, L. Bone Texture Analysis on Direct Digital Radiographic Images: Precision Study and Relationship with Bone Mineral Density at the Os Calcis. *Calcif. Tissue Int.* **2007**, *80*, 97–102. [CrossRef]
32. Bar, A.; Wolf, L.; Bergman Amitai, O.; Toledano, E.; Elnekave, E. Compression Fractures Detection on CT. In Proceedings of the Medical Imaging 2017: Computer-Aided Diagnosis, Orlando, Fl, USA, 3 March 2017; Armato, S.G., Petrick, N.A., Eds.; SPIE: Bellingham, WC, USA, 2017; Volume 10134.
33. Roth, H.R.; Wang, Y.; Yao, J.; Lu, L.; Burns, J.E.; Summers, R.M. Deep Convolutional Networks for Automated Detection of Posterior-Element Fractures on Spine CT. In Proceedings of the Medical Imaging 2016: Computer-Aided Diagnosis, International Society for Optics and Photonics, San Diego, CA, USA, 24 March 2016; SPIE: Bellingham, WC, USA, 2016; Volume 9785, p. 97850.
34. Emohare, O.; Cagan, A.; Morgan, R.; Davis, R.; Asis, M.; Switzer, J.; Polly, D.W. The Use of Computed Tomography Attenuation to Evaluate Osteoporosis Following Acute Fractures of the Thoracic and Lumbar Vertebra. *Geriatr. Orthop. Surg. Rehabil.* **2014**, *5*, 50–55. [CrossRef]
35. Dzierżak, R.; Omiotek, Z.; Tkacz, E.; Kępa, A. The Influence of the Normalisation of Spinal CT Images on the Significance of Textural Features in the Identification of Defects in the Spongy Tissue Structure. In Proceedings of the Innovations in Biomedical Engineering, Katowice, Poland, 18–20 October 2018; Tkacz, E., Gzik, M., Paszenda, Z., Piętka, E., Eds.; Springer International Publishing: Cham, Switzerland, 2019; pp. 55–66.
36. Oprogramowanie –> Program MaZda. Available online: http://www.eletel.p.lodz.pl/programy/cost/progr_mazda.html (accessed on 3 May 2020).
37. Haralick, R.M. Statistical and Structural Approaches to Texture. *Proc. IEEE* **1979**, *67*, 786–804. [CrossRef]

38. Haralick, R.M.; Shanmugam, K.; Dinstein, I. Textural Features for Image Classification. *IEEE Trans. Syst. Man Cybern.* **1973**, *SMC-3*, 610–621. [CrossRef]
39. Hu, Y.; Dennis, T.J. Textured Image Segmentation by Context Enhanced Clustering. *IEE Proc. Vis. Image Signal Process.* **1994**, *141*, 413–421. [CrossRef]
40. Lerski, R.A.; Straughan, K.; Schad, L.R.; Boyce, D.; Blüml, S.; Zuna, I. MR Image Texture Analysis—An Approach to Tissue Characterization. *Magn. Reson. Imaging* **1993**, *11*, 873–887. [CrossRef]
41. Omiotek, Z. Improvement of the Classification Quality in Detection of Hashimoto's Disease with a Combined Classifier Approach. *Proc. Inst. Mech. Eng. Part H J. Eng. Med.* **2017**, *231*, 774–782. [CrossRef]
42. Omiotek, Z.; Stepanchenko, O.; Wójcik, W.; Legieć, W.; Szatkowska, M. The Use of the Hellwig's Method for Feature Selection in the Detection of Myeloma Bone Destruction Based on Radiographic Images. *Biocybern. Biomed. Eng.* **2019**, *39*, 328–338. [CrossRef]
43. Dzierżak, R. Comparison of the influence of standardization and normalization of data on the effectiveness of spongy tissue texture classification. *Inform. Control Meas. Econ. Environ. Prot.* **2019**, *9*, 66–69. [CrossRef]
44. Scikit-Learn: Machine Learning in Python—Scikit-Learn 0.22.2 Documentation. Available online: https://scikit-learn.org/stable/ (accessed on 3 May 2020).
45. Hassani, A.S.E.B.E.; Hassouni, M.E.; Houam, L.; Rziza, M.; Lespessailles, E.; Jennane, R. Texture Analysis Using Dual Tree M-Band and Rényi Entropy. Application to Osteoporosis Diagnosis on Bone Radiographs. In Proceedings of the 2012 9th IEEE International Symposium on Biomedical Imaging (ISBI), Barcelona, Spain, 2–5 May 2012. [CrossRef]
46. Singh, A.; Dutta, M.K.; Jennane, R.; Lespessailles, E. Classification of the Trabecular Bone Structure of Osteoporotic Patients Using Machine Vision. *Comput. Biol. Med.* **2017**, *91*, 148–158. [CrossRef]
47. Zheng, K.; Makrogiannis, S. Bone Texture Characterization for Osteoporosis Diagnosis Using Digital Radiography. *Conf Proc IEEE Eng. Med. Biol. Soc.* **2016**, *2016*, 1034–1037. [CrossRef]
48. Areeckal, A.S.; Kamath, J.; Zawadynski, S.; Kocher, M.; Sumam, D.S. Combined Radiogrammetry and Texture Analysis for Early Diagnosis of Osteoporosis Using Indian and Swiss Data. *Comput. Med. Imaging Graph.* **2018**, *68*, 25–39. [CrossRef]
49. Omiotek, Z.; Dzierżak, R.; Uhlig, S. Fractal Analysis of the Computed Tomography Images of Vertebrae on the Thoraco-Lumbar Region in Diagnosing Osteoporotic Bone Damage. *Proc. Inst. Mech. Eng. H* **2019**, *233*, 1269–1281. [CrossRef]
50. Yger, F. Challenge IEEE-ISBI/TCB: Application of Covariance Matrices and Wavelet Marginals. *arXiv* **2014**, arXiv:1410.2663.
51. Houam, L.; Hafiane, A.; Boukrouche, A.; Lespessailles, E.; Jennane, R. One Dimensional Local Binary Pattern for Bone Texture Characterization. *Pattern Anal. Appl.* **2014**, *17*, 179–193. [CrossRef]
52. Tafraouti, A.; Hassouni, M.E.; Toumi, H.; Lespessailles, E.; Jennane, R. Osteoporosis Diagnosis Using Frequency Separation and Fractional Brownian Motion. In Proceedings of the 2017 International Conference on Wireless Networks and Mobile Communications (WINCOM), Rabat, Morocco, 1–4 November 2017; pp. 1–4.
53. Oulhaj, H.; Rziza, M.; Amine, A.; Toumi, H.; Lespessailles, E.; El Hassouni, M.; Jennane, R. Anisotropic Discrete Dual-Tree Wavelet Transform for Improved Classification of Trabecular Bone. *IEEE Trans. Med. Imaging* **2017**, *36*, 2077–2086. [CrossRef]
54. Oulhaj, H.; Rziza, M.; Amine, A.; Toumi, H.; Lespessailles, E.; Jennane, R.; Hassouni, M.E. Trabecular Bone Characterization Using Circular Parametric Models. *Biomed. Signal Process. Control* **2017**, *33*, 411–421. [CrossRef]
55. Harrar, K.; Jennane, R.; Zaouchi, K.; Janvier, T.; Toumi, H.; Lespessailles, E. Oriented Fractal Analysis for Improved Bone Microarchitecture Characterization. *Biomed. Signal Process. Control* **2018**, *39*, 474–485. [CrossRef]
56. Lee, S.; Lee, J.W.; Jeong, J.-W.; Yoo, D.-S.; Kim, S. A Preliminary Study on Discrimination of Osteoporotic Fractured Group from Nonfractured Group Using Support Vector Machine. *Conf. Proc. IEEE Eng. Med. Biol. Soc.* **2008**, *2008*, 474–477. [CrossRef]

Lublin, 20.12.2022

dr hab. inż. Zbigniew Omiotek, prof. Uczelni
Wydział Elektrotechniki i Informatyki
Politechnika Lubelska

Oświadczenie współautora

Oświadczam, iż mój udział w przygotowaniu publikacji:

1. *Comparison of the Classification Results Accuracy for CT Soft Tissue and Bone Reconstructions in Detecting the Porosity of a Spongy Tissue,* **Róża Dzierżak**, Zbigniew Omiotek, Ewaryst Tkacz and Sebastian Uhlig / Journal of Clinical Medicine, vol. 11, nr 15, s. 1-11, (2022).

wchodzącej w skład rozprawy doktorskiej Pani dr inż. Róży Dzierżak polegał na wsparciu w zakresie doboru metodologii badań oraz opracowaniu kodu algorytmów.

Zbigniew Omiotek
Podpis

Zabrze, 23.01.2023

prof. dr hab. inż. Ewaryst Tkacz
Wydział Inżynierii Biomedycznej/
Katedra Biosensorów i Przetwarzania Sygnałów Biomedycznych

Oświadczenie współautora

Oświadczam, iż mój udział w przygotowaniu publikacji:

1. *Comparison of the Classification Results Accuracy for CT Soft Tissue and Bone Reconstructions in Detecting the Porosity of a Spongy Tissue,* **Róża Dzierżak**, Zbigniew Omiotek, Ewaryst Tkacz and Sebastian Uhlig / Journal of Clinical Medicine, vol. 11, nr 15, s. 1-11, (2022).

wchodzącej w skład rozprawy doktorskiej Pani dr inż. Róży Dzierżak polegał na konsultacji zakresu badań oraz ostatecznej wersji manuskryptu.

.....
Podpis

Lublin, 20.12.2022

dr n. med. Sebastian Uhlig
Zakład Radiologii Lekarskiej
Uniwersytet Medyczny w Lublinie

Oświadczenie współautora

Oświadczam, iż mój udział w przygotowaniu publikacji:

1. *Comparison of the Classification Results Accuracy for CT Soft Tissue and Bone Reconstructions in Detecting the Porosity of a Spongy Tissue,* **Róża Dzierżak**, Zbigniew Omiotek, Ewaryst Tkacz and Sebastian Uhlig / Journal of Clinical Medicine, vol. 11, nr 15, s. 1-11, (2022).

wchodzącej w skład rozprawy doktorskiej Pani dr inż. Róży Dzierżak polegał na doborze danych obrazowych pacjentów wraz z ich opisem.

Podpis

4.2 *Application of deep convolutional neural networks in the diagnosis of osteoporosis*

Autorzy: **Róża Dzierżak** and Zbigniew Omiotek

Opublikowano: Sensors.- 2022, vol. 22, nr 21, s. 1−18

DOI: https://doi.org/10.3390/s22218189

Impact Factor: **3.847**

Liczba punktów ministerialnych: **100**

Udział pierwszego autora w poniżej załączonym artykule polegał na opracowaniu koncepcji badań, analizie literaturowej, opracowaniu otrzymanych wyników oraz przygotowaniu manuskryptu (70%). Wkład współautorów, w formie oświadczenia, zamieszczono na końcu artykułu.

Celem przeprowadzonych badań była ocena możliwości wykorzystania głębokich konwolucyjnych sieci neuronowych (DCNN) do opracowania skutecznej metody diagnozowania osteoporozy na podstawie zdjęć tomografii komputerowej kręgosłupa. W badaniu wykorzystano sześć wstępnie wytrenowanych architektur DCNN o różnych głębokościach topologicznych (VGG16, VGG19, MobileNetV2, Xception, ResNet50, InceptionResNetV2). Najlepsze wyniki uzyskano dla modelu VGG16 charakteryzującego się najniższą głębokością topologiczną (ACC = 95%, TPR = 96% i TNR = 94%). Pewnym wyzwaniem podczas badania była stosunkowo niewielka (jak na deep learning) liczba obserwacji (400 obrazów). Problem ten został rozwiązany przy użyciu wstępnie wyszkolonych modeli DCNN na dużym zbiorze danych oraz techniki rozszerzania danych. Uzyskane wyniki pozwalają wnioskować, że technika transfer learning daje zadowalające wyniki podczas budowy głębokich modeli do diagnostyki osteoporozy na podstawie małych zbiorów danych obrazów TK kręgosłupa. W artykule zaproponowano oryginalny algorytm analizy obrazów CT kręgu L1, przy wykorzystaniu modelu sieci VGG16, dla którego uzyskano najlepsze wyniki parametrów klasyfikacji.

sensors

MDPI

Article

Application of Deep Convolutional Neural Networks in the Diagnosis of Osteoporosis

Róża Dzierżak and Zbigniew Omiotek *

Department of Electronics and Information Technology, Lublin University of Technology, ul. Nadbystrzycka 38A, 20-618 Lublin, Poland
* Correspondence: z.omiotek@pollub.pl

Abstract: The aim of this study was to assess the possibility of using deep convolutional neural networks (DCNNs) to develop an effective method for diagnosing osteoporosis based on CT images of the spine. The research material included the CT images of L1 spongy tissue belonging to 100 patients (50 healthy and 50 diagnosed with osteoporosis). Six pre-trained DCNN architectures with different topological depths (VGG16, VGG19, MobileNetV2, Xception, ResNet50, and InceptionResNetV2) were used in the study. The best results were obtained for the VGG16 model characterised by the lowest topological depth (ACC = 95%, TPR = 96%, and TNR = 94%). A specific challenge during the study was the relatively small (for deep learning) number of observations (400 images). This problem was solved using DCNN models pre-trained on a large dataset and a data augmentation technique. The obtained results allow us to conclude that the transfer learning technique yields satisfactory results during the construction of deep models for the diagnosis of osteoporosis based on small datasets of CT images of the spine.

Keywords: osteoporosis; convolutional neural networks; deep learning; VGG16; image classification; neural networks

Citation: Dzierżak, R.; Omiotek, Z. Application of Deep Convolutional Neural Networks in the Diagnosis of Osteoporosis. *Sensors* **2022**, 22, 8189. https://doi.org/10.3390/s22218189

Academic Editor: Zongwei Zhou

Received: 28 September 2022
Accepted: 24 October 2022
Published: 26 October 2022

1. Introduction

Due to the fact that we live in an aging society, osteoporosis has become a disease of serious concern around the world. According to the WHO definition, osteoporosis is a systemic skeletal disease characterised by low bone mass, impaired microarchitecture of bone tissue and, consequently, increased fragility and susceptibility to fractures. In 2019, the number of cases in Europe increased to 32 million (5.6% of the total European population aged 50+) [1]. The development of this disease is influenced by lifestyle, especially diet and physical activity. Thus, it can be expected that the pandemic will worsen the situation and significantly affect the progression of the disease in patients. According to reports [1], the incidence rate will increase significantly in the near future. It should be remembered that, in the last two years, patients were referred to osteoporosis-dedicated follow-up examinations much less frequently [2], and, therefore, so many patients are still unaware of their disease. Most often, osteoporosis is diagnosed at an advanced stage, when osteoporotic fractures occur. This is especially dangerous for the spine. Therefore, continuous research is necessary in order to develop the best diagnostic method that would allow the detection of osteoporosis at an early stage of development [3]. The general trend of research in this area shows that the best results are obtained from the analysis of bone tissue microarchitecture [2,4–9].

In recent years, a rapid development of machine learning algorithms has taken place, especially deep learning methods. Deep learning is a machine learning concept based on artificial neural networks [10]. In most cases, they use multiple layers of interconnected neural networks. There are many types of architecture of such networks, including deep belief networks, convolutional networks, recursive networks, long short-term memories,

deep Boltzmann machines, and deep coding networks. Many of them work very well in the process of image recognition, including biomedical images. Recent studies report the use of artificial neural networks in the diagnostics of intramucosal gastric cancer [11], early detection and prediction of chronic kidney disease [12], major depressive and bipolar disorders [13], as well as COVID-19 pneumonia [14]. There are also publications on new methods of diagnosing osteoporosis with the use of deep learning [15–17].

One of the important issues in building machine learning models (including deep models), is the estimation of uncertainty as a measure of confidence in the model's predictions. This problem, among others in the area of computer vision, is successfully addressed by using Bayesian convolutional neural networks (BCNNs). Networks of this type prevent over-fitting by introducing uncertainty estimation. BCNNs are preferred in problems where CNNs are an appropriate learning model, but, due to too little data, they may become overtrained. An extension of the problem of uncertainty estimation using BCNNs and experimental results can be found, among others, in [18–20].

An important issue affecting the wider use of machine learning models, particularly in healthcare, is interpretability [21]. A model is interpretable when the decisions it makes can be fully understood [22]. Unfortunately, for ordinary users, machine learning models, especially deep models, are similar to black boxes. Therefore, aiming for a wider application of artificial intelligence solutions in healthcare, a better understanding of the models' mechanisms becomes crucial. Consequently, attempts are being made to improve the interpretability and transparency of machine learning models [23–25]. This is due to the need to establish a trust relationship between users and decision-making models in practical implementation applications.

The key problem of machine learning comes down to a trade-off between optimisation and generalisation. Optimisation involves tuning the model to obtain the best possible performance for the learning data. Generalisation, on the other hand, determines how well the model performs when processing new data. After a certain number of iterations (epochs) of the learning algorithm, generalisation for validation data reaches a constant level and then (mostly) starts to deteriorate. This means that over-fitting of the model to the learning data is taking place (overtraining). Various methods are used to combat over-fitting, which are generally referred to as regularisation methods [26]. Popular regularisation methods applied to learning deep convolutional neural networks include: transfer learning, dropout, data augmentation, early stopping, weights regularisation (L1, L2, max-norm), and others [27–30]. A summary and comparison of these and other regularisation methods is included in [31]. The problem of regularisation is still an area of active research, so new efficient algorithms are constantly being proposed, e.g., the two-stage training method [31].

The effects of the conducted research allow the detection of the porosity of L1 spongy tissue by analysing and classifying the spinal CT images using deep convolutional neural networks (DCNN). This is a new approach in the research on the diagnosis of osteoporosis. To the best of the authors' knowledge, no research in which deep learning algorithms would be used to solve this problem is available. The proposed method enables to significantly simplify the stage of image pre-processing and analysis before using images to build the classifier model. The convolutional neural network is able to reveal the internal features of individual observations based on the raw data obtained from images, while ensuring high classification efficiency.

In this article, Section 2.1 describes the material used in the research and the method of selecting images. The following Section 2.2 describe the construction of the classification models, as well as the characteristics of the architecture of the network models used. Section 3 presents the obtained results of the network operation. The discussion and comparison of the research results with other works are presented in Section 4. The final part of the article summarizes the achievements and presents a plan for further work.

2. Materials and Methods

2.1. Material

The study used computed tomography images of the spine in the lumbosacral (L-S) section from 100 patients. The imaging tests used in the study were performed in the tomography laboratory located in the Independent Clinical Hospital No. 4 in Lublin (Poland). Patients were referred for examinations of the lumbosacral (L-S) spine from the orthopaedic clinic and the Hospital Emergency Department. Each patient was tested on a GE 32-row CT scan in a standard spine examination protocol, including the lumbar and sacral (L-S) vertebrae. Fifty of the patients belonged to the control group of healthy people, unaffected by osteoporosis or osteopenia. There was an equal number of patients in the group diagnosed with osteoporosis. The control group included 26 women and 24 men. The age range of the patients ranged from 53 to 77 years. The group with diagnosed osteoporosis included 33 women and 17 men aged 44 to 95 years. The patients were classified into both groups based on the description of the examination prepared by the radiologist and the measurement of the radiological density of the spongy tissue of the first lumbar spine (L1). On the basis of the literature [32], the tissue density limit was set at 120 Hounsfield units (HU).

The source data contained images in RGB mode with a resolution of 512 × 512 pixels and was saved in the DICOM format. Soft tissue reconstruction images were used for the research. The research showed that the images derived from soft tissue reconstruction allow obtaining more accurate values of texture parameters, increasing the accuracy of classification, and offering better possibilities for diagnosing osteoporosis [33]. From the series of images, the sample sections showing the inside of the circle with the spongy essence were selected (Figure 1).

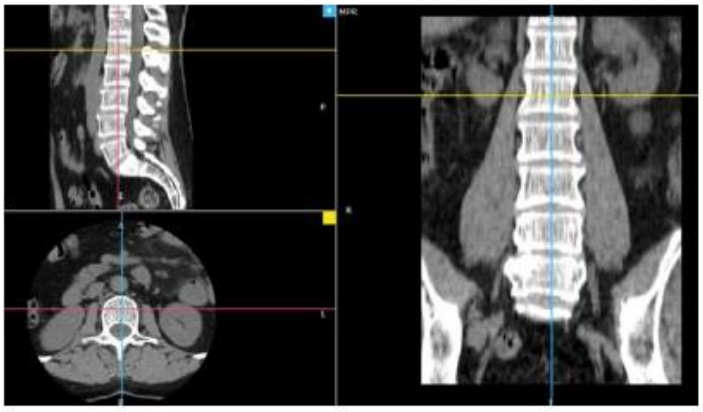

Figure 1. The arrangement of the axis in the centre of one of the vertebrae (image in three projections).

Four L1 transverse images were selected from a series of studies of each patient. These images presented the sections of the vertebra closest to the middle value of its height, so that the largest possible area of the spongy tissue was visible (Figure 2). One image sample of the examined tissue was obtained from each of the selected cross-sections.

The size of the extracted samples was selected to use the textured surface, potentially containing the information in the image of the transverse vertebra section, to the maximum extent. As a result, 400 samples with dimensions of 50 × 50 pixels were obtained. The sample images of the tissue from healthy and osteoporotic patients are presented below (Figure 3).

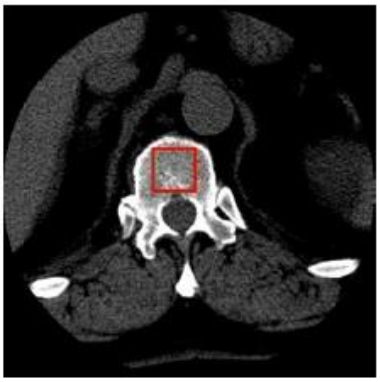

Figure 2. Manual selection of the spongy matter region.

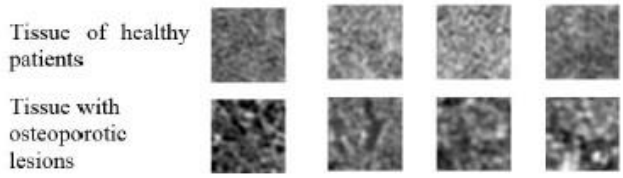

Figure 3. Image samples of healthy patients' tissue and tissues with osteoporotic lesions in their original size.

The image histogram normalisation process is one of the image preprocessing techniques frequently used for classification. As part of the studies previously carried out by the authors, it was shown that this operation reduces the classification accuracy from 4% for the TPR coefficient to 14% for ACC [34].

2.2. *Construction of the Classification Models*

The full dataset contained 400 observations, 200 of which were healthy subjects and 200 were patients diagnosed with osteoporosis. Following the procedure described in Section 2.1, both image categories were assigned labels, HEALTHY and OSTEOPOROTIC, respectively. Then, the full dataset was randomly divided into training, validation, and test subsets, with the number of observations belonging to individual classes in each of these subsets being the same. As a result of the division, the training set constituted 50% of the full set (100 observations for each class), 25% of the validation set (50 observations), and 25% of the test set (50 observations). The use of deep neural networks in research was a certain challenge, because, in the context of teaching such networks, the available number of observations was very small. Therefore, classifier models that had been previously trained on large datasets were employed. This approach is often used in the situations similar to the one considered [35]. If the dataset used to train the model was sufficiently large and general, the spatial hierarchy of the learned features can effectively act as an overall model for image processing. Such features can be helpful in solving new image processing problems, even when the problems relate to the recognition of classes other than the original classes used to train the model.

A computer with Windows 10 64-bit system, Intel Core i5-3470 3.20 GHz processor and 32 GB RAM was used to build the models. The TensorFlow 1.13.1 platform (TensorFlow, 2020), the Keras 2.2.4 [36] library, and the Python 3.7.3 programming language were employed. The calculations were performed using the GPU (NVIDIA GeForce GTX 1060 3 GB), the CUDA 9.0 platform, and the cuDNN 7.0 library. The Keras library contains many models for image processing, including Xception [37], VGG16, VGG19 [38],

ResNet [39], ResNetV2 [40], InceptionV3 [41], InceptionResNetV2 [42], MobileNet [43], MobileNetV2 [44], DenseNet [35], and NASNet [45]. All these models were trained on the ImageNet collection containing approximately 1.4 million images divided into 1000 classes [46]. In the study, 6 models characterised by different topological depth were used (Table 1).

Table 1. Models for image classification with weights trained on ImageNet that have been used in the study (CB—Convolution Base).

No.	Model	The Number of Layers of the CB	Fine-Tuned Layers of the CB	Type of Fine-Tuned Layers
1	VGG16	19	12–19	2D convolution
2	VGG19	22	13–22	2D convolution
3	Xception	132	117–132	depth-wise separable 1D and 2D convolution, batch normalization
4	MobileNetV2	155	136–155	2D convolution, depth-wise convolution, batch normalization
5	ResNet50	175	150–175	2D convolution, batch normalization
6	InceptionResNetV2	780	631–780	2D convolution, batch normalization

The VGG network is characterised by the smallest topological depth among the models implemented in the Keras package and a small convolutional filter of 3 × 3 pixels [38]. The VGG16 network consists of thirteen convolutional layers and three fully connected layers. The VGG19 model, on the other hand, consists of 16 convolutionary layers and three fully interconnected layers (Figure 4). Both networks use 3 × 3 pixel convolution filters. The results of the VGG network showed that a relatively small number of its layers allows for a high classification accuracy [47].

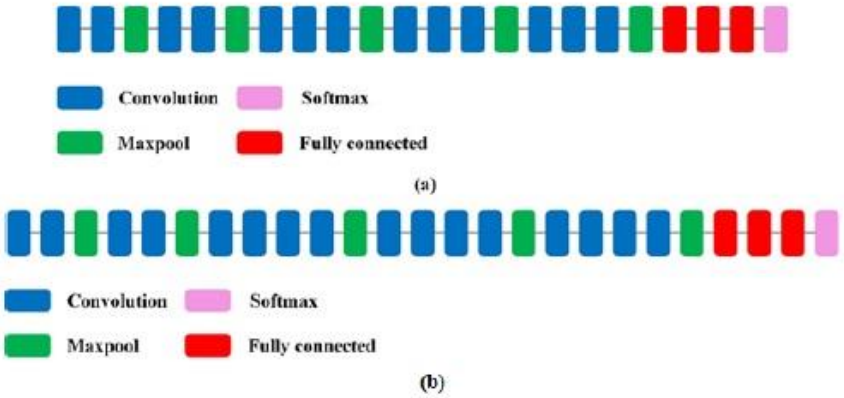

Figure 4. Structure of the VGG16 (**a**) and VGG19 (**b**) network models [47].

MobileNetV2 is a neural network architecture that uses efficient convolutional operations called Depthwise Separable Convolution (Figure 5). Depthwise separable convolution layers spatially convolve each input channel independently and then perform a point convolution of mixing the channels (1 × 1 convolution). This is equivalent to separating learning spatial features from learning the features of individual channels. The advantages of this technique are especially important when training small models on a limited dataset [48].

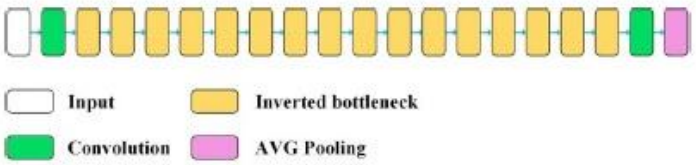

Figure 5. Structure of the MobileNetV2 network model [47].

In the Xception network, starting blocks are based on deep, separate convolutional layers. The architecture of the Xception model is built around a linear stack of 36 deep, separate convolutional layers with linear residual connections (Figure 6). In this configuration, there are two important convolutional layers: a deep convolution layer where spatial convolution is performed independently on each input channel, and a point convolution layer where the 1×1 layer maps output channels to a new channel space using deep convolutions [37].

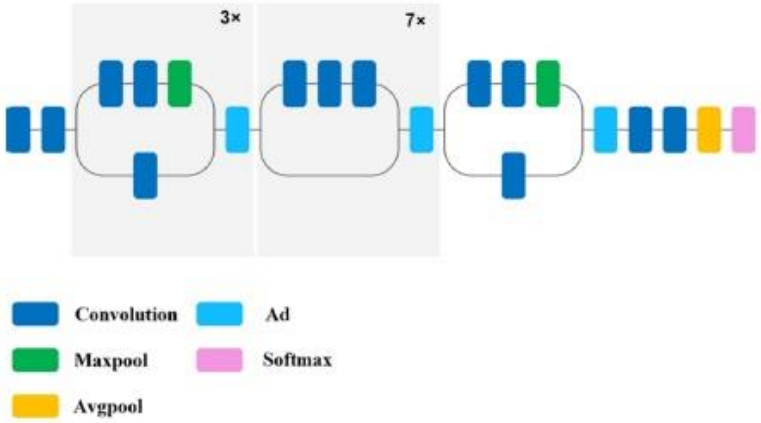

Figure 6. Structure of the Xception network model [47].

The ResNet model is characterised by a very deep network with 152 layers. ResNet deep configuration solves the problem of vanishing gradient by taking advantage of deep residual learning through additive identity transformations. In particular, the residual module uses a direct path between input and output, and each stacked layer matches the residual mapping rather than directly matching the desired base mapping. The optimization process is much easier for the residual mapping compared to the original unreferenced map. As with the VGG models, 3×3 pixel filters are most commonly used in this network. However, ResNet has fewer filters of lower complexity. The 1×1 convolution layers deepen the lattice and increase non-linearity by applying the ReLU function after each 1×1 convolution layer. In this network, fully interconnected layers are replaced by a pooling average layer. This significantly reduces the number of parameters as fully interconnected layers contain a large number of them. The network is, therefore, able to learn deeper representations of functions with fewer parameters [49]. The structure of the ResNet network is shown in Figure 7.

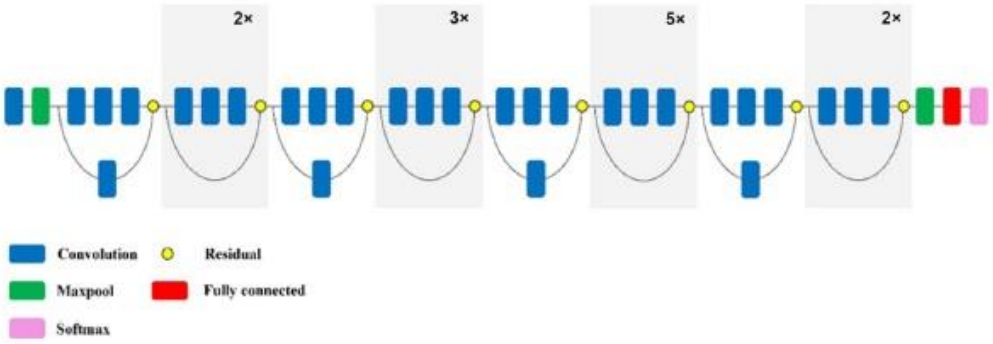

Figure 7. Simplified structure of the ResNet network model [47].

The InceptionResNetV2 network is built by integrating two models of deep convolutional networks, such as ResNet and Inception. In these networks, normalization is only applied at the top of traditional layers. The remaining modules allow you to increase the number of Inception blocks and, thus, increase the depth of the network. The most problematic issue with very deep networks is the learning phase, which can be solved with residual connections. The network rescales these connections, which is taken as an effective approach to solving the learning problem when a large number of filters (over 1000) are used in the network. In particular, the remaining variants experience instability, and the network cannot be trained when the number of filters exceeds 1000. Therefore, the residual connection scaling contributes to stabilizing the network training [50]. Figure 8 shows the compressed structure of the InceptionResNetV2 network.

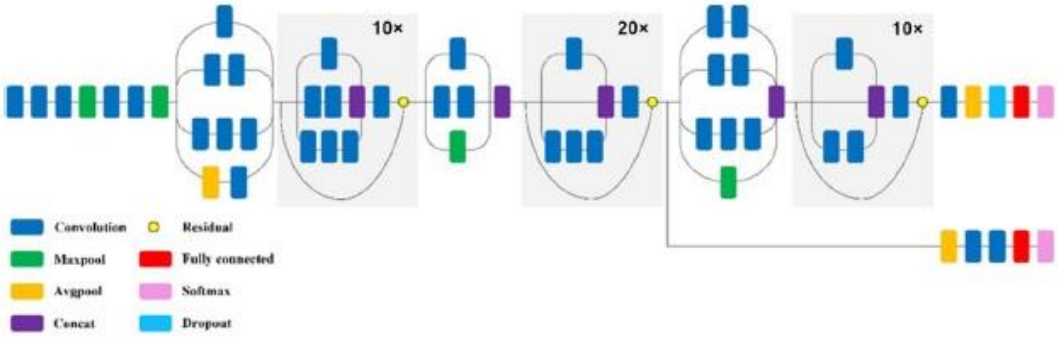

Figure 8. Simplified structure of the InceptionResNetV2 network model [47].

The models consisted of two parts. The first was convolutional bases, and the second was densely connected classifiers, located at the end of the network. Convolution bases were used because the representations they learned presented general concepts that are suitable for solving various image processing problems. Instead of the original classifiers, the authors used their own classifiers, made of two Dense layers. The representations they learned were specific to the set of classes tested (HEALTHY and OSTEOPOROTIC categories) on which these models were trained. Figure 9 shows the general diagram of a deep network implementation which consists of a convolutional base and a new binary classifier (2 Dense layers) added at its end.

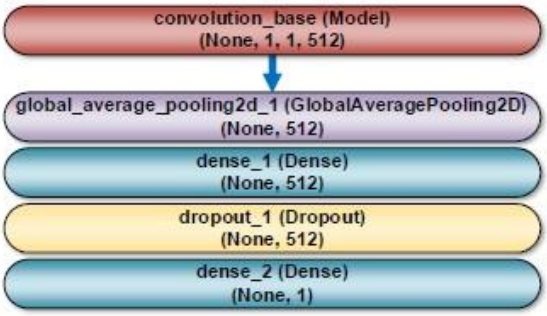

Figure 9. A general scheme for the implementation of a deep network that consists of a convolution base and own classifier. The meaning of the Keras classes is as follows: GlobalAveragePooling2D—a layer responsible for the global average pooling operation for spatial data; Dense—a densely connected layer; Dropout—a layer that limits the excessive adjustment of the model to the training data. The feature map has a shape (samples, height, width, and channels). The first dimension equal to None means any number of samples.

The models were built as sequential Keras models. After convolution base, the first layer of the own classifier was GlobalAveragePooling2D. It performed pooling operations for spatial data based on a global average. Two densely connected layers were added. The first Dense layer, with 512 neurons in the output and the ReLU (Rectified Linear Unit) activation function, interpreted the features extracted by the convolution base. The second Dense layer, with 1 output neuron and the sigmoid activation function, was an output layer that predicted that an observation belonged to a specific class. One Dropout layer with the parameter rate = 0.3 was added as well, to limit the excessive adjustment of the model to the training data.

Model training was performed in two phases:

1. Feature extraction—the convolution base has been frozen, and the added dense layers, creating a new classifier, were initiated randomly and trained over a period of 200 epochs using data augmentation. Layer freezing consists of preventing the update of their weights in the training process, so that the representations previously learned by the convolution base have not been modified during training.
2. Fine tuning—the upper layers of the convolution base have been unfrozen and trained for a period of 300 epochs together with the new layers, also using data augmentation. At the end, the entire convolution base has been unfrozen.

Augmentation consisted of performing random, vertical and horizontal transformations of the image, rotation, cropping, zooming in, and reflecting half of the image in a horizontal plane. During models training, binary cross entropy as a loss function was used. The optimisation algorithm was root mean square propagation (RMSprop) with a low value of the learning parameter. It was 2×10^{-5} for the feature extraction phase and 10^{-5} for fine tuning. The low value of this parameter resulted from the fact that modifications of the representation of the tuned layers of the convolution base had to be minimised. Excessive changes in these values could negatively impact data representations. Accuracy was used as a measure of the training process. In the last layer of the classifier, the sigmoid activation function was used. More detailed information on the settings used during the model building process is provided in Table 2.

Table 2. Settings used during the models building process.

	Parameter	Value
Training	epochs	200 (feature extraction), 300 (fine tuning)
	batch size	5
Model	loss function	binary cross entropy
	optimizer	root mean square propagation (RMSprop)
	metrics	accuracy
Optimizer	learning rate	2×10^{-5} (feature extraction), 10^{-5} (fine tuning)
	rho	0.9
	momentum	0.0
	epsilon	10^{-7}
	centred	False
Data augmentation	rotation range	40°
	width shift range	0.2
	height shift range	0.2
	shear range	0.2
	zoom range	0.2
	horizontal flip	True

As an implementation example, Figure 10 shows the detailed structure of the VGG16 network used. RGB images of 50 × 50 pixels are passed to the input of the network. As part of the preprocessing, a rescaling of RGB pixel intensities to the [0, 1] range was performed. The convolution base contains 13 Keras objects of the Conv2D class that form the convolution kernels. At first, the image passes through the first block built of 2 convolution layers, with ReLU activation functions. In these layers, a reception field of 3 × 3 pixels is used, the convolution stride is 1 pixel, and the padding is also equal to 1 pixel. Each layer of the first block contains 64 filters. The configuration used ensures that the spatial resolution is maintained, i.e., the size of the output activation map is the same as the dimensions of the input image. Subsequently, the activation maps are sent through a max pooling layer with a window size of 2 × 2 pixels and a stride of 2 pixels. As a result, the size of the activation maps is halved. Thus, the size of the activation maps in the output of the first block is 25 × 25 × 64. In an identical manner activation maps are sent through the second block. The only difference is that it contains 128 filters. Therefore, the size of the activation maps in the output of the second block is 12 × 12 × 128. Then, there is a third block, containing 3 convolution layers and a max pool layer. In this case, the number of filters is 256, so that, the size of the activation maps in the output of the block is 6 × 6 × 256. Further there are two more blocks (the fourth and fifth) containing 3 convolution layers each with 512 filters. The size of the activation maps in the output of the last block is 1 × 1 × 512. The convolution base is followed by own classifier (Figure 9). At its beginning, there is a layer responsible for the global average pooling operation. Next, there is a fully connected layer with the ReLU activation function, containing 512 neurons. Behind it there is a dropout layer with a rate parameter equal to 0.3, which limits the over-fitting of the model to the training data. Finally, there is a second fully connected layer, working as an output layer. It contains 1 neuron and a sigmoidal activation function.

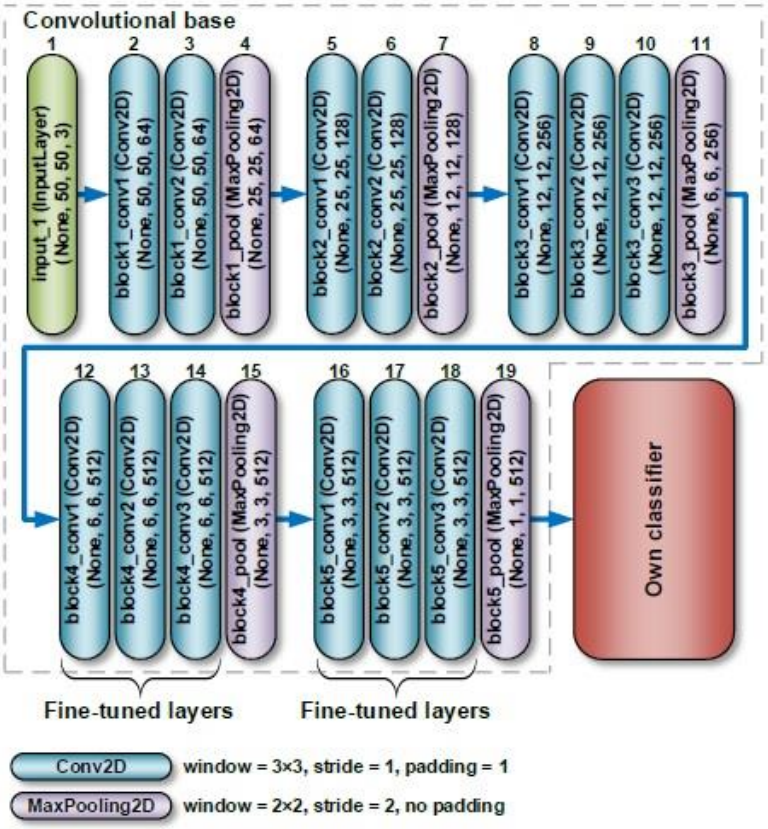

Figure 10. Structure of the VGG16 network.

3. Results

Network training was performed in two phases. They are described in more detail in Section 2.2. In the first phase (feature extraction), new network layers (a new classifier) were trained, while the entire convolution base was frozen. In the second phase (fine tuning), a certain number of final layers of the convolution base was unfrozen and trained together with the new classifier. The plots of the training and validation accuracy are shown in Figure 11.

The final effect of the whole training process was the Keras model containing the classifier architecture, which was saved to disk as a single HDF5 file. Six such models were built during the research, one for each type of network architecture. These models were used to classify new images that did not participate in the training and validation process. Classification accuracy (ACC), sensitivity (TPR), specificity (TNR), and area under the ROC curve (AUC) were calculated (Figure 12). In addition, confusion matrices that show the distribution of correct and incorrect classification cases were built (Figure 13).

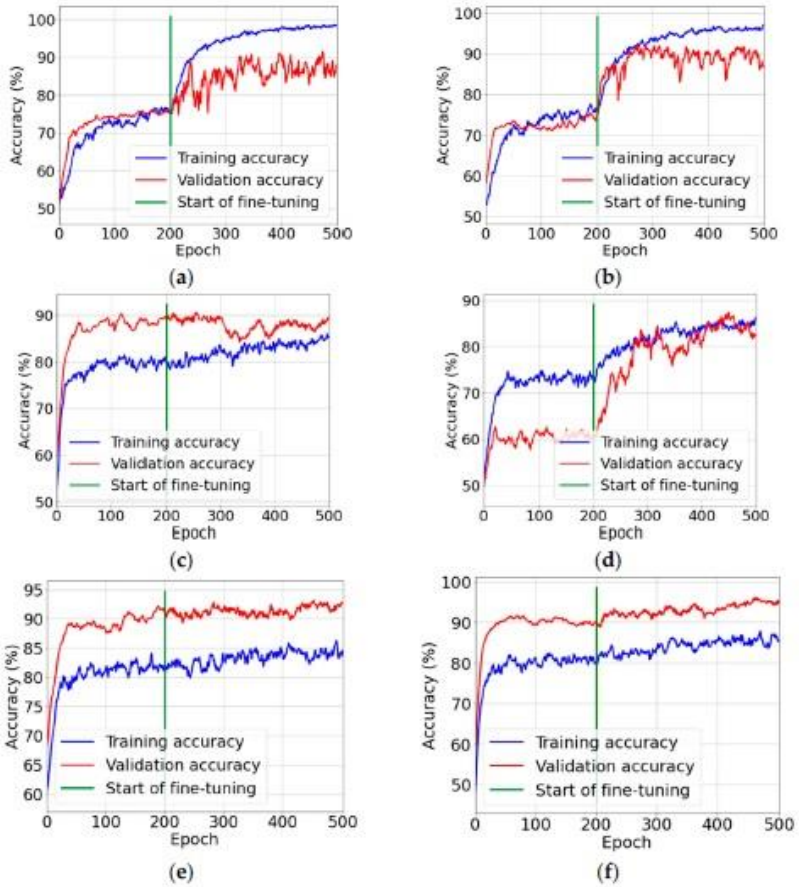

Figure 11. Plots of the training and validation accuracy during the stages of feature extraction and fine tuning: (**a**) VGG16; (**b**) VGG19; (**c**) MobileNetV2; (**d**) Xception; (**e**) ResNet50; and (**f**) InceptionResNetV2.

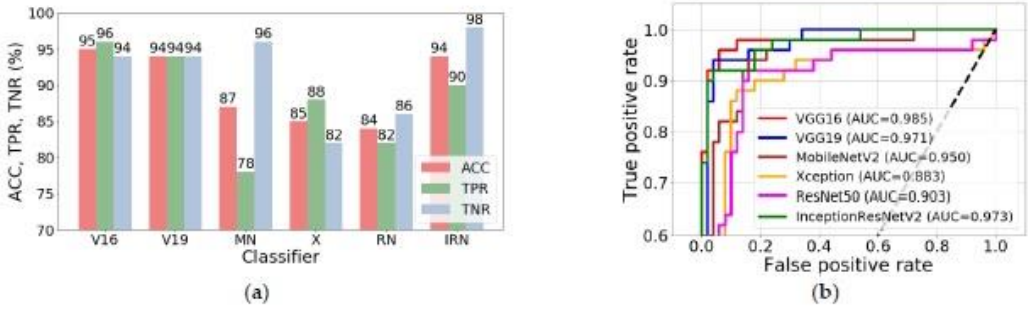

Figure 12. Classification results (**a**) and ROC curves and AUCs for the test set (**b**). Symbols used: V16—VGG16, V19—VGG19, MN—MobileNetV2, X—Xception, RN—ResNet50, and IRN—InceptionResNetV2.

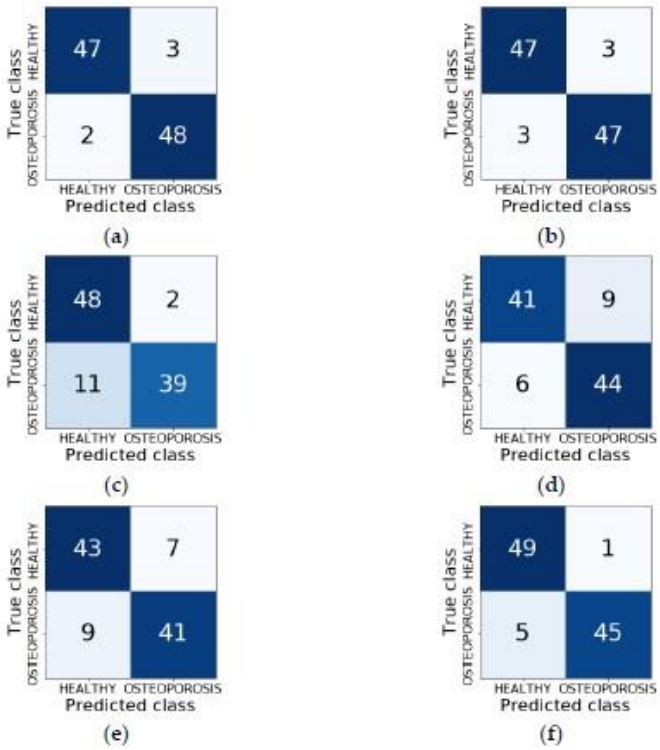

Figure 13. Confusion matrices: (**a**) VGG16; (**b**) VGG19; (**c**) MobileNetV2; (**d**) Xception; (**e**) ResNet50; and (**f**) InceptionResNetV2.

As shown in Figure 3, the tissue image texture of healthy patients is smooth and homogeneous. In the case of sick patients, the texture of the tissue image is characterised by porosity and a significant number of dark spots corresponding to osteoporotic lesions. These texture properties are reflected in the feature maps built by the subsequent convolutional network layers. For the cases shown in Figure 14, the images of healthy patients (top row) contain a number of dark spots characteristic of osteoporosis. In contrast, the images of patients diagnosed with osteoporosis (bottom row) are relatively smooth and homogeneous, with a small number of darker spots. This situation makes these images more difficult cases to classify than the other images in the test set. However, this is not an abnormal situation, as when classifying biomedical images, the possibility of cases that are more difficult to recognise than the others should always be taken into account.

Table 3 shows the GPU and CPU inference time of the individual models for a single observation. A computer with Windows 10 64-bit system, Intel Core i7-4770 3.40 GHz processor, 32 GB RAM, and an NVIDIA GeForce GTX 1660 Ti 6 GB graphics card was used to measure the inference times. As expected, the fastest model was VGG16, which is due to its smallest topological depth (Table 1). Additionally, noteworthy is the ResNet50 model, which, with a relatively low inference time for the GPU (22 ms), experienced only one and a half times the inference time degradation for the CPU.

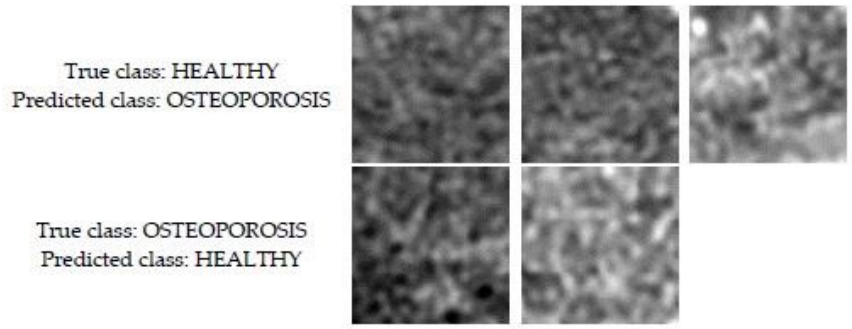

Figure 14. Images that were misclassified by the best VGG16 model.

Table 3. Inference time for a single observation.

Model	GPU Inference Time [ms]	CPU Inference Time [ms]	Latency Increasing (t_{CPU} / t_{GPU})
VGG16	5.6	20.6	3.7
VGG19	7.0	26.1	3.7
Xception	25.2	58.0	2.3
ResNet50	22.0	33.9	1.5
MobileNetV2	21.1	65.0	3.1
InceptionResNetV2	93.8	115.0	1.2

4. Discussion

The stage of building classifiers brought very good results. Out of the six models built, as many as three achieved the classification accuracy at the level exceeding 90% (Figure 11a). For reference, the VGG16 model achieved ACC = 95%, TPR = 96%, and TNR = 94%. At the same time, this model can be considered the best because it has the highest overall classification accuracy (95%), as well as the highest sensitivity (TPR = 96%), which is medically important for patients. The other two models are also characterised by very good quality indicators. For the VGG19 classifier, ACC = 94%, with TPR = TNR = 94%, and for the InceptionResNetV2 model ACC = 94%, TPR = 90%, and TNR = 8%. The high efficiency of the VGG16, VGG19, and InceptionResNetV2 models is also reflected in the ROC curve diagram. The AUC parameter, calculated on the basis of this plot, is equal to 0.985, 0.971, and 0.973 for the above models, respectively.

The vast majority of all quality indicators of the above-mentioned models exceeded the level of 90%. This is a very good result, taking into account the extremely small number of observations used to train the models. Each class had 200 observations, of which 100 belonged to the training set, 50 to the validation set, and 50 to the test set. For deep neural networks, these are very small datasets, because typically sets of thousands of observations are used for training them. It was possible to obtain very good results owing to the approach of using classifiers that were pre-trained on a very large ImageNet dataset. The operation of fine-tuning the top layers of the convolutional basis, together with two layers of a custom classifier added at the end of the model, proved very successful. The research confirmed that this approach may be recommended in the case of small datasets.

It should also be emphasised that the best results were obtained for the models with the smallest topological depth. The convolution base of the VGG16 model consisted of 19 layers, and in the case of the VGG19 model, there were 22 layers. Thus, the models with the lowest complexity turned out to be the most effective for a very small size of the training set. This may suggest that the number of observations was too small for the MobileNetV2, Xception, and ResNet50 models. Nevertheless, although the InceptionResNetV2 model had the greatest complexity (780 layers), it achieved very good quality indicators (ACC = 94%, TPR = 90%, TNR = 98%). A certain drawback of the method discussed is that

the extraction of areas of interest was performed manually. However, this issue requires conducting separate research and will, therefore, become an area of interest in the course of further work.

A list of the results enabling to make such a comparison is provided in Table 4. As it can be seen, the results obtained are at a level comparable with the results of other authors, achieved in solving similar classification problems.

The results presented in this article are easiest to compare with the results of the studies presented in [51,52], as they concerned the same type of images, i.e., those obtained as a result of computed tomography. These studies also share the same anatomical object of interest, i.e., the spine, which is one of the elements of the human skeleton most vulnerable to osteoporosis. Due to its key role in the structure of the human body and complications after vertebral fractures leading to immobilisation of the patient and sometimes even death, the spine is the subject of many experiments aimed at preventing the final stage of the disease. As a result of the research, the outcome of which are shown in Table 4, the sensitivity of classifiers ranging from 78.83% to 98.56% obtained in study [16] with the use of the AlexNET model was obtained. In work [51], the values of the sensitivity and specificity of the used classifier were also given, which were TPR = 83.9% and TNR = 93.8%.

In contrast, study [53] presents a slightly different approach to the diagnosis of osteoporosis, but is also based on artificial neural networks. Instead of images, the research material consisted of data on the age, weight, height, and T-index of the femoral neck. The parameters shown were to be used as input data for the osteoporosis risk prediction algorithm. The achieved results were: ACC = 78.83%, AUC = 0.829, TNR = 90.12%, and TPR = 51.0%. The low value of the classifier's sensitivity may indicate the correctness of the theory about the key importance of the analysis of bone tissue microarchitecture.

Table 4. Comparison with other authors.

Item No.	Role	Research Material	The Method Used	Classifier Quality Assessment Parameter
Our research	Application of deep convolutional neural networks in the diagnosis of osteoporosis	CT images of L1 spongy tissue from 100 patients (50 healthy and 50 diagnosed with osteoporosis)	VGG16, VGG19, MobileNetV2, Xception, ResNet50, InceptionResNetV2	ACC = 95%, TPR = 96%, TNR = 94%
[54]	Classification of osteoporosis on the basis of CR images of phalanges using DCNN	101 computed radiography images of phalanges	An undefined convolutional network model from the Caffe package	TPR = 64.7%, FPR = 6.51%
[51]	Identification of vertebral compression fractures caused by osteoporosis	3701 CT tests, 2681 (72%) were negative for the presence of VCF and 1020 (28%) were marked as positive for VCF,	Convolutional network and a classifier based on a recursive network	ACC = 89.1%, TPR = 83.9%, TNR = 93.8 %
[52]	Automatic detection of osteoporotic vertebral fractures on CT scans	1432 CT images of the spine	(1) a function extraction module based on CNN ResNet34 and (2) an RNN module for aggregating the extracted features and making the final diagnosis.	ACC = 89.2%, F1 score = 90.8%
[55]	Metacarpal screening for osteoporosis	4000 radiographs of the metacarpus	AlexNet	TPR = 82.4%, TNR = 95.7%
[53]	Diagnostic examination and prediction of the risk of osteoporosis in women	Age, weight, height, and T-score of the femoral neck of 1559 women	Radial basic function of artificial neural networks with the 2-4-1 architecture	ACC = 78.83%, AUC = 0.829, TPR = 51.0%, TNR = 90.12%

Table 4. *Cont.*

Item No.	Role	Research Material	The Method Used	Classifier Quality Assessment Parameter
[56]	Prediction of osteoporosis from simple hip radiography	1012 simple hip radiographs	VGG16 model	ACC = 81.2%, TPR = 91.1%, TNR = 68.9%, PPV = 78.5%, NPV = 86.1%
[16]	Predicting osteoporosis based on the mandibular cortical index on panoramic radiographs	Panoramic radiographs of mandibular 744 female patients	AlexNET, GoogleNET, ResNET-50, SqueezeNET, and ShuffleNET deep-learning models	ACC = 81.14%(AlexNET), ACC = 88.94% (GoogleNET), ACC = 98.56% (AlexNET), ACC = 92.79% (GoogleNET)

Figure 15 shows the general scheme of the system for predicting new images using the VGG16 model, which achieved the highest quality indicators (ACC = 95%, TPR = 96%, and TNR = 94%). At the same time, this model is characterised by the lowest topological complexity (the convolution base contains 19 layers). After ROI extraction, new observations are fed to the input of the VGG16 model. The model analyses the data and calculates the probability of belonging to a positive class (OSTEOPOROTIC). If this probability is equal to or greater than 0.5, the classification module assigns the OSTEOPOROTIC label to the observations. Otherwise, the observation is labelled HEALTHY. Figure 16 shows the various possible prediction results for the sample test images. These results were obtained using a prototype system for the diagnosis of osteoporosis, which uses the VGG16 model for prediction.

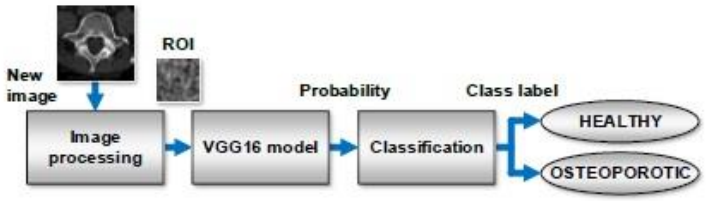

Figure 15. Process flow during the prediction of a class of new images.

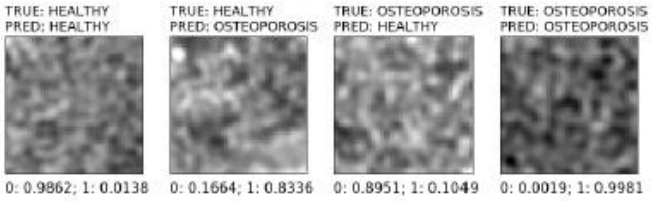

Figure 16. Various prediction results of sample images.

5. Conclusions

The article presents an algorithm for the classification of computed tomography images of the spongy tissue of the lumbar spine using six different convolutional neural network models. Out of the convolutional network models built, as many as three achieved the classification accuracy at a level exceeding 90%. The VGG16 network model turned out to be the best, because it is characterised by the highest classification accuracy (ACC = 95%) and the highest sensitivity (TPR = 96%), which is very important from the medical point of view. This means that properly constructed and trained convolutional neural networks can be the basis for the creation of an effective method for the diagnosis of spinal osteoporosis, through the classification of CT images of spongy tissue.

The plan for further work includes the attempts to create a complete osteoporosis diagnostic system based on the CT images of the spine and other bone elements exposed to this disease. The practical implementation of the proposed prototype osteoporosis diagnostic system based on the VGG16 convolutional network model should be preceded by tests on a larger number of patients and creation of an algorithm for automatic segmentation of tissue image samples from the sequence of images in the DICOM format directly from the CT scanner.

Author Contributions: Conceptualization, R.D. and Z.O.; methodology, R.D. and Z.O.; software, Z.O.; validation, R.D. and Z.O.; formal analysis, R.D. and Z.O.; investigation, R.D. and Z.O.; resources, R.D.; data curation, R.D; writing—original draft preparation, R.D.; writing—review and editing, Z.O.; visualization, R.D. and Z.O.; supervision, Z.O.; project administration, R.D. and Z.O.; funding acquisition, R.D. and Z.O. All authors have read and agreed to the published version of the manuscript.

Funding: This research was funded by the Ministry of Education and Science—Poland, grant number FD-20/EE-2/302 and FD-20/EE-2/315.

Institutional Review Board Statement: Not applicable.

Informed Consent Statement: Not applicable.

Data Availability Statement: The data presented in this study are available on request from the corresponding author. The data are not publicly available due to restrictions regarding privacy.

Conflicts of Interest: The authors declare no conflict of interest.

References

1. International Osteoporosis Foundation. Key Statistics For Europe. Available online: https://www.osteoporosis.foundation/ (accessed on 18 September 2022).
2. Camacho, P.M.; Petak, S.M.; Binkley, N.; Diab, D.L.; Eldeiry, L.S.; Farooki, A.; Harris, S.T.; Hurley, D.L.; Kelly, J.; Lewiecki, E.M.; et al. American College of Endocrinology Clinical Practice Guidelines for the Diagnosis and Treatment of Postmenopausal Osteoporosis—2020 Update. *Endocr. Pract.* **2020**, *26*, 1–46. [CrossRef] [PubMed]
3. Smets, J.; Shevroja, E.; Hügle, T.; Leslie, W.D.; Hans, D. Machine Learning Solutions for Osteoporosis—A Review. *J. Bone Miner. Res.* **2021**, *36*, 833–851. [CrossRef] [PubMed]
4. Jolly, S.; Chaudhary, H.; Bhan, A.; Rana, H.; Goyal, A. Texture based Bone Radiograph Image Analysis for the assessment of Osteoporosis using Hybrid Domain. In Proceedings of the 2021 3rd International Conference on Signal Processing and Communication (ICPSC), Coimbatore, India, 13–14 May 2021; pp. 344–349. [CrossRef]
5. Tang, C.; Zhang, W.; Li, H.; Li, L.; Li, Z.; Cai, A.; Wang, L.; Shi, D.; Yan, B. CNN-based qualitative detection of bone mineral density via diagnostic CT slices for osteoporosis screening. *Osteoporos. Int.* **2021**, *32*, 971–979. [CrossRef] [PubMed]
6. Fang, Y.; Li, W.; Chen, X.; Chen, K.; Kang, H.; Yu, P.; Zhang, R.; Liao, J.; Hong, G.; Li, S. Opportunistic osteoporosis screening in multi-detector CT images using deep convolutional neural networks. *Eur. Radiol.* **2021**, *31*, 1831–1842. [CrossRef]
7. Patil, K.A.; Prashanth, K.V.M.; Ramalingaiah, A. Texture Feature Extraction of Lumbar Spine Trabecular Bone Radiograph Image using Laplacian of Gaussian Filter with KNN Classification to Diagnose Osteoporosis. *J. Phys. Conf. Ser.* **2021**, *2070*, 012137. [CrossRef]
8. Yamamoto, N.; Sukegawa, S.; Yamashita, K.; Manabe, M.; Nakano, K.; Takabatake, K.; Kawai, H.; Ozaki, T.; Kawasaki, K.; Nagatsuka, H.; et al. Effect of Patient Clinical Variables in Osteoporosis Classification Using Hip X-rays in Deep Learning Analysis. *Medicina* **2021**, *57*, 846. [CrossRef]
9. Patil, K.A.; Prashant, K.V.M. Segmentation of Lumbar [L1-L4] AP Spine X-ray images using various Level Set methods to detect Osteoporosis. In Proceedings of the IEEE Bombay Section Signature Conference (IBSSC), Gwalior, India, 18–20 November 2021; pp. 1–6. [CrossRef]
10. Janiesch, C.; Zschech, P.; Heinrich, K. Machine learning and deep learning. *Electron. Mark.* **2021**, *31*, 685–695. [CrossRef]
11. Tang, D.; Zhou, J.; Wang, L.; Ni, M.; Chen, M.; Hassan, S.; Luo, R.; Chen, X.; He, X.; Zhang, L.; et al. A Novel Model Based on Deep Convolutional Neural Network Improves Diagnostic Accuracy of Intramucosal Gastric Cancer (With Video). *Front. Oncol.* **2021**, *11*, 622827. [CrossRef]
12. Singh, V.; Asari, V.K.; Rajasekaran, R.A. Deep Neural Network for Early Detection and Prediction of Chronic Kidney Disease. *Diagnostics* **2022**, *12*, 116. [CrossRef] [PubMed]
13. Lei, Y.; Belkacem, A.N.; Wang, X.; Sha, S.; Wang, C.; Chen, C. A convolutional neural network-based diagnostic method using resting-state electroencephalograph signals for major depressive and bipolar disorders. *Biomed. Signal Process. Control.* **2022**, *72 Pt B*, 103370. [CrossRef]

14. Prudhvi Kumar, B.; Anithaashri, T.P. Novel Diagnostic System for COVID-19 Pneumonia Using Forward Propagation of Convolutional Neural Network Comparing with Artificial Neural Network. *ECS Trans.* **2022**, *107*, 13797. [CrossRef]
15. Varalakshmi, P.; Sathyamoorthy, S.; Darshan, V.; Ramanujan, V.; Rajasekar, S.J.S. Detection of Osteoporosis with DEXA Scan Images using Deep Learning Models. In Proceedings of the International Conference on Advances in Computing, Communication and Applied Informatics (ACCAI), Chennai, India, 28–29 January 2022; pp. 1–6. [CrossRef]
16. Tassoker, M.; Öziç, M.U.; Yuce, F. Comparison of five convolutional neural networks for predicting osteoporosis based on mandibular cortical index on panoramic radiographs. *Dentomaxillofacial Radiol.* **2022**, *51*, 20220108. [CrossRef] [PubMed]
17. Nakamoto, T.; Taguchi, A.; Kakimoto, N. Osteoporosis screening support system from panoramic radiographs using deep learning by convolutional neural network. *Dentomaxillofac Radiol.* **2022**, *51*, 20220135. [CrossRef] [PubMed]
18. Kendall, A.; Gal, Y. What uncertainties do we need in bayesian deep learning for computer vision? In Proceedings of the Annual Conference on Neural Information Processing Systems 2017, Long Beach, CA, USA, 4–9 December 2017; Volume 30.
19. De Sousa Ribeiro, F.; Calivá, F.; Swainson, M.; Gudmundsson, K.; Leontidis, G.; Kollias, S. Deep bayesian self-training. *Neural Comput. Appl.* **2020**, *32*, 4275–4291. [CrossRef]
20. Gal, Y.; Ghahramani, Z. Bayesian Convolutional Neural Networks with Bernoulli Approximate Variational Inference. *arXiv* **2015**, arXiv:1506.02158 [stat.ML].
21. Ibrahim, M.; Louie, M.; Modarres, C.; Paisley, J.W. Global Explanations of Neural Networks: Mapping the Landscape of Predictions. In Proceedings of the 2019 AAAI/ACM Conference on AI, Ethics, and Society, Honolulu, HI, USA, 27–28 January 2019.
22. Kästner, C. Interpretability and Explainability. Available online: https://ckaestne.medium.com/interpretability-andexplainability-a80131467856 (accessed on 8 October 2022).
23. Loyola-González, O. Black-Box vs. White-Box: Understanding Their Advantages and Weaknesses from a Practical Point of View. *IEEE Access* **2019**, *7*, 154096–154113. [CrossRef]
24. Cao, N.; Yan, X.; Shi, Y.; Chen, C. AI-Sketcher: A Deep Generative Model for Producing High-Quality Sketches. In Proceedings of the AAAI Conference on Artificial Intelligence, Honolulu, HI, USA, 27 January–1 February 2019; Volume 33, pp. 2564–2571.
25. Shouling, J.; Jinfeng, L.; Tianyu, D.; Bo, L. Survey on Techniques, Applications and Security of Machine Learning Interpretability. *J. Comput. Res. Dev.* **2019**, *56*, 2071–2096.
26. Rumelhart, D.E.; Hinton, G.E.; Williams, R.J. Learning representations by back-propagating errors. *Nature* **1986**, *323*, 533–536. [CrossRef]
27. Hinton, G.E.; Srivastava, N.; Krizhevsky, A.; Sutskever, I.; Salakhutdinov, R.R. Improving neural networks by preventing co-adaptation of feature detectors. *arXiv* **2012**, arXiv:1207.0580v1 [cs.NE].
28. Srivastava, N.; Hinton, G.; Krizhevsky, A.; Sutskever, I.; Salakhutdinov, R. Dropout: A Simple Way to Prevent Neural Networks from Overfitting. *J. Mach. Learn. Res.* **2014**, *15*, 1929–1958.
29. Xie, L.; Wang, J.; Wei, Z.; Wang, M.; Tian, Q. DisturbLabel: Regularizing CNN on the loss layer. In Proceedings of the 2016 IEEE Conference on Computer Vision and Pattern Recognition (CVPR), Las Vegas, NV, USA, 27–30 June 2016; pp. 4753–4762. [CrossRef]
30. Ioffe, S.; Szegedy, C. Batch normalization: Accelerating deep network training by reducing internal covariate shift. In Proceedings of the International Conference on Machine Learning, Lille, France, 7–9 July 2015; pp. 448–456.
31. Zheng, Q.; Yang, M.; Yang, J.; Zhang, Q.; Zhang, X. Improvement of generalization ability of deep CNN via implicit regularization in two-stage training process. *IEEE Access* **2018**, *6*, 15844–15869. [CrossRef]
32. Emohare, O.; Cagan, A.; Morgan, R.; Davis, R.; Asis, M.; Switzer, J.; Polly, D.W. The Use of Computed Tomography Attenuation to Evaluate Osteoporosis Following Acute Fractures of the Thoracic and Lumbar Vertebra. *Geriatr. Orthop. Surg. Rehabil.* **2014**, *5*, 50–55. [CrossRef]
33. Dzierżak, R.; Omiotek, Z.; Tkacz, E.; Uhlig, S. Comparison of the Classification Results Accuracy for CT Soft Tissue and Bone Reconstructions in Detecting the Porosity of a Spongy Tissue. *J. Clin. Med.* **2022**, *11*, 4526. [CrossRef] [PubMed]
34. Dzierżak, R.; Omiotek, Z.; Tkacz, E.; Kępa, A. The Influence of the Normalisation of Spinal CT Images on the Significance of Textural Features in the Identification of Defects in the Spongy Tissue Structure. In *Innovations in Biomedical Engineering, Proceedings of the Conference on Innovations in Biomedical Engineering, Katowice, Poland, 18–20 October 2018*; Springer: Cham, Switzerland, 2019; pp. 55–66.
35. Huang, G.; Liu, Z.; Maaten, L.; Weinberger, K.Q. Densely Connected Convolutional Networks. *arXiv* **2018**, arXiv:1608.06993v5 [cs.CV].
36. Keras. Keras library. Available online: https://keras.io/ (accessed on 10 February 2020).
37. Chollet, F. Xception: Deep Learning with Depthwise Separable Convolutions. *arXiv* **2017**, arXiv:1610.02357v3 [cs.CV].
38. Simonyan, K.; Zisserman, A. Very Deep Convolutional Networks for Large-Scale Image Recognition. In Proceedings of the International Conference on Learning Representations (ICLR 2015), San Diego, CA, USA, 7–9 May 2015.
39. He, K.; Zhang, X.; Ren, S.; Sun, J. Deep Residual Learning for Image Recognition. *arXiv* **2015**, arXiv:1512.03385v1 [cs.CV].
40. He, K.; Zhang, X.; Ren, S.; Sun, J. Identity Mappings in Deep Residual Networks. *arXiv* **2016**, arXiv:1603.05027v3 [cs.CV].
41. Szegedy, C.; Vanhoucke, V.; Ioffe, S.; Shlens, J.; Wojna, Z. Rethinking the Inception Architecture for Computer Vision. *arXiv* **2015**, arXiv:1512.00567v3 [cs.CV].
42. Szegedy, C.; Ioffe, S.; Vanhoucke, V.; Alemi, A. Inception-v4, Inception-ResNet and the Impact of Residual Connections on Learning. *arXiv* **2016**, arXiv:1602.07261v2 [cs.CV]. [CrossRef]

43. Howard, A.G.; Zhu, M.; Chen, B.; Kalenichenko, D.; Wang, W.; Weyand, T.; Andreetto, M.; Hartwig, A. MobileNets: Efficient Convolutional Neural Networks for Mobile Vision Applications. *arXiv* **2017**, arXiv:1704.04861v1 [cs.CV].
44. Sandler, M.; Howard, A.; Zhu, M.; Zhmoginov, A.; Chen, L.-C. MobileNetV2: Inverted Residuals and Linear Bottlenecks. *arXiv* **2019**, arXiv:1801.04381v4 [cs.CV].
45. Zoph, B.; Vasudevan, V.; Shlens, J.; Le, Q.V. Learning Transferable Architectures for Scalable Image Recognition. *arXiv* **2018**, arXiv:1707.07012v4 [cs.CV].
46. Deng, J.; Dong, W.; Socher, R.; Li, L.-J.; Li, K.; Fei-Fei, L. ImageNet: A large-scale hierarchical image database. In Proceedings of the 2009 IEEE Conference on Computer Vision and Pattern Recognition, Miami, FL, USA, 20–25 June 2009.
47. Mahdianpari, M.; Salehi, B.; Rezaee, M.; Mohammadimanesh, F.; Zhang, Y. Very Deep Convolutional Neural Networks for Complex Land Cover Mapping Using Multispectral Remote Sensing Imagery. *Remote Sens.* **2018**, *10*, 1119. [CrossRef]
48. Dong, K.; Zhou, C.; Ruan, Y.; Li, Y. MobileNetV2 Model for Image Classification. In Proceedings of the 2020 2nd International Conference on Information Technology and Computer Application (ITCA), Guangzhou, China, 18–20 December 2020; pp. 476–480. [CrossRef]
49. Wu, Z.; Shen, C.; Hengel, A. Wider or Deeper: Revisiting the ResNet Model for Visual Recognition. *Pattern Recognit.* **2019**, *90*, 119–133. [CrossRef]
50. Peng, C.; Liu, Y.; Yuan, X.; Chen, Q. Research of image recognition method based on enhanced inception-ResNet-V2. *Multimed. Tools Appl.* **2022**, *81*, 34345–34365. [CrossRef]
51. Bar, A.; Wolf, L.; Amitai, O.B.; Toledano, E.; Elnekave, E. Compression Fractures Detection on CT. In Proceedings of the SPIE Medical Imaging, Orlando, FL, USA, 12–14 February 2017.
52. Tomita, N.; Cheung, Y.Y.; Hassanpour, S. Deep neural networks for automatic detection of osteoporotic vertebral fractures on CT scans. *Comput. Biol. Med.* **2018**, *98*, 8–15. [CrossRef]
53. Meng, J.; Sun, N.; Chen, Y.; Li, Z.; Cui, X.; Fan, J.; Cao, H.; Zheng, W.; Jin, O.; Jiang, L.; et al. Artificial neural networkoptimizes self-examination of osteoporosis risk in women. *J. Int. Med. Res.* **2019**, *47*, 3088–3098. [CrossRef]
54. Hatano, K.; Murakami, S.; Lu, H.; Tan, J.K.; Kim, H.; Aoki, T. Classification of Osteoporosis from Phalanges CR Images Based on DCNN. In Proceedings of the 2017 17th International Conference on Control, Automation and Systems (ICCAS 2017), Jeju, Korea, 18–21 October 2017.
55. Nahom, N.; Teitel, J.; Morris, M.R.; Sani, N.; Mitten, D.; Hammert, W.C. Convolutional Neural Network for Second Metacarpal Radiographic Osteoporosis Screening. *J. Hand Surg. Am.* **2020**, *45*, 175–181.
56. Jang, R.; Choi, J.H.; Kim, N.; Chang, J.S.; Yoon, P.W.; Kim, C.-H. Prediction of osteoporosis from simple hip radiography using deep learning algorithm. *Sci. Rep.* **2021**, *11*, 19997. [CrossRef]

Lublin, 20.12.2022

dr hab. inż. Zbigniew Omiotek, prof. Uczelni
Wydział Elektrotechniki i Informatyki
Politechnika Lubelska

Oświadczenie współautora

Oświadczam, iż mój udział w przygotowaniu publikacji:

1. *Application of Deep Convolutional Neural Networks in the Diagnosis of Osteoporosis,* **Róża Dzierżak**, Zbigniew Omiotek / *Sensors, vol. 22, nr 21, s. 1-18, (2022).*

wchodzącej w skład rozprawy doktorskiej Pani dr inż. Róży Dzierżak polegał na wsparciu w zakresie doboru metodologii oraz implementacji kodu w języku Python.

Zbigniew Omiotek
Podpis

4.3 *Fractal analysis as a method for feature extraction in detecting osteoporotic bone destruction*

Autorzy: Zbigniew Omiotek, **Róża Dzierżak**, Andrzej Kępa

Opublikowano: Fractals: Complex Geometry, Patterns, and Scaling in Nature and Society.- 2021, vol. 29, nr 4, s. 49−64.

DOI: https://doi.org/10.1142/S0218348X2150095X

Impact Factor: **4.555**

Liczba punktów ministerialnych: **100**

Udział drugiego autora w poniżej załączonym artykule polegał na analizie literaturowej, analizie otrzymanych wyników oraz przygotowaniu manuskryptu (30%). Wkład współautorów, w formie oświadczenia, zamieszczono na końcu artykułu.

Do przeprowadzenia badań prezentowanych w niniejszym artykule wykorzystano analizę fraktalną w celu określenia zestawu deskryptorów cech, które można zastosować w procesie diagnozowania uszkodzeń kości spowodowanych osteoporozą. Na podstawie analizy fraktalnej i selekcji cech metodą liniowej regresji krokowej uzyskano trzy deskryptory. Były to dwa wymiary fraktalne obliczone metodą wariacyjną oraz lakunarność fraktalna obliczona metodą liczenia pudełek. Pierwsze dwa deskryptory uzyskano w wyniku analizy obrazów szarych, a trzeci był wynikiem analizy obrazów binarnych. Skuteczność deskryptorów została zweryfikowana za pomocą sześciu popularnych nadzorowanych metod klasyfikacji: liniowej i kwadratowej analizy dyskryminacyjnej, naiwnego klasyfikatora Bayesa, drzewa decyzyjnego, K-najbliższych sąsiadów oraz lasów losowych. Najlepsze wyniki uzyskano stosując klasyfikator K-NN; były to: ogólna trafność klasyfikacji – 81%, czułość klasyfikacji – 78%, specyficzność klasyfikacji – 90%, dodatnia wartość predykcyjna – 90%, ujemna wartość predykcyjna – 77%.

Fractals, Vol. 29, No. 4 (2021) 2150095 (15 pages)

DOI: 10.1142/S0218348X2150095X

World Scientific
www.worldscientific.com

FRACTAL ANALYSIS AS A METHOD FOR FEATURE EXTRACTION IN DETECTING OSTEOPOROTIC BONE DESTRUCTION

ZBIGNIEW OMIOTEK*,‡, RÓŻA DZIERŻAK* and ANDRZEJ KĘPA†
*Faculty of Electrical Engineering and Computer Science
Lublin University of Technology Nadbystrzycka 38d
20-618 Lublin, Poland
†Department of Radiology and Nuclear Medicine
Independent Public Clinical Hospital No. 4
Jaczewskiego 8, 20-954 Lublin, Poland
‡z.omiotek@pollub.pl

Received June 10, 2018
Accepted December 19, 2020
Published April 19, 2021

Abstract

Fractal analysis was used in the study to determine a set of feature descriptors which could be applied in the process of diagnosing bone damage caused by osteoporosis. The subject of the research was CT images of vertebrae on the thoraco-lumbar region. The dataset contained images of healthy patients and patients diagnosed with osteoporosis. On the basis of fractal analysis and feature selection by linear stepwise regression, three descriptors were obtained. These were two fractal dimensions calculated by the variation method and fractal lacunarity calculated by the box counting method. The first two descriptors were obtained as a result of the analysis of gray images, and the third was the result of analysis of binary images. The effectiveness of the descriptors was verified using six popular supervised classification methods: linear and quadratic discriminant analyses, naive Bayes classifier, decision tree, K-nearest neighbors (K-NN) and random forests. The best results were obtained using the K-NN classifier; they

‡Corresponding author.

were as follows: overall classification accuracy: 81%, classification sensitivity: 78%, classification specificity: 90%, positive predictive value: 90% and negative predictive value: 77%. The results of the research have shown that fractal analysis can be a useful tool to extract features of spinal CT images in the diagnosis of osteoporotic bone defects.

Keywords: Fractal Analysis; Fractal Dimension; Osteoporosis; Feature Extraction; Computed Tomography; Texture Analysis; Feature Selection; Classification.

1. INTRODUCTION

Osteoporosis is a metabolic disease characterized by progressive loss of bone mass, weakening of bone spatial structure and increased susceptibility to fractures. The development of the disease is influenced by a deficiency of calcium, estrogen and genetic determinants. As a result of imbalance between the osteoblast osteogenic activity and osteoclastogenesis and bone resorption, there are changes in tissue microarchitecture. The number of bone beams in the spongy structure decreases, which increases the risk of damage and fractures. The area particularly exposed to them is the thoracolumbar section of the spine.[1,2]

The test performed to diagnose osteoporosis is a study of bone mineral density, called densitometry. The indicator corresponding to the standard deviation (SD) from the peak bone mass serves to assess the patient's condition. Bone mineral content determines the amount of minerals at the site of measurement, which divided by the surface of the studied area gives the bone mineral density (BMD). Considering that the results are related to the constant value of the classification of the indicator, there is a risk that it is not 100% adequate to each examined bone segment.[3,4] This creates the need to search for more precise diagnostic methods.

Due to doubts related to the correct and precise diagnostics of bone defects, new diagnostic solutions are still sought.[3–6] An opportunity to create an effective system is to use the image results of spinal computed tomography (CT). Images from contemporary tomographs, in comparison with other medical imaging techniques, are characterized by high accuracy, high resolution and contrast. Thanks to the good quality of the results obtained, it is possible to analyze the texture of tissues.[7] Its aim is to find a set of parameters, called textural features, each of which is a numerical measure of a specific texture property.[8]

There are several approaches to the extraction of textural features. The most popular are statistical, mathematical, transformational and structural models. In this work, fractal analysis was used to describe the features of the image texture, which offers a tool in the form of the fractal dimension. Fractal analysis is readily used in research using biomedical images.[9] There are also many works in which this method has been used in osteoporosis research. The subject of interest here is various elements of the skeletal system, and the analysis itself is based on the results of various imaging methods. For example, the purpose of the research presented by Camargo *et al.*[10] was to assess the risk of osteoporosis. The fractal dimension was used there to assess the morphology of trabecular bone on the basis of X-ray images of the forearm bones. In turn, the changes in jaw bone caused by osteoporosis were examined by Güngör *et al.*[11] The study used computed tomography images. The results of the research concerning the evaluation of the possibility of applying the fractal dimension to the detection of osteoporosis in postmenopausal women are described by Mostafa *et al.*[12] The subject of the study was CT images of the mandible. In the study carried out by Vijayalakshmi *et al.*,[13] the possibility of using the fractal dimension as an indicator of the occurrence of osteoporosis in women was assessed. X-rays of the mandible were also used for this purpose. As part of the research presented by Harrar and Jennane,[14] the fractal dimension was used to distinguish cases with osteoporotic fractures of the femur, occurring in postmenopausal women, from the cases belonging to the control group. X-rays of the heel bone were used here. Also, Tafraouti *et al.*[15] used images of the same type. Fractal analysis was performed for different orientations of the region of interest (ROI), and as a result of classification with the use of support vector machine method, the general accuracy of 95% was obtained. Fractal analysis was also effective in distinguishing cases of

osteoporosis from healthy cases in postmenopausal women, where CT scans of the forearm bone were the subject of the study.[16] Very often, images of lumbar vertebrae are used in the research. Czyz *et al.*[17] presented the results on the possible use of fractal analysis of CT images of such vertebrae to determine bone density, and Dougherty and Henebry[18] applied fractal lacunarity as an indicator of the severity of osteoporosis and prediction of bone fracture risk. Fractal lacunarity was also used by Zaia,[19] where the analysis of MRI images of lumbar vertebrae presents the possibilities of using this indicator to assess the risk of osteoporotic bone fracture in postmenopausal women.

One of the disadvantages of most of the previously cited works is that during fractal analysis they use only one method (usually box counting), which applies only binary images and does not necessarily give the most accurate estimate of the fractal dimension. In addition, the assessment of the obtained results is made by testing the significance of differences in mean values in the groups (disease and control). This approach is the most correct and required in the presentation of the results of medical research, but it does not give full information about the predicted accuracy of the automatic system for diagnosing osteoporosis.

The new approach presented in this paper is that during the analysis, several different estimators of the fractal dimension are applied, which use both gray and binary images. The best ones are chosen using the appropriate selection method. In addition to the fractal dimension, estimated by different methods, other parameters obtained on the basis of fractal analysis, such as intercept and lacunarity, are also used. This approach extends the possibilities of the present method. In this work, in contrast to the cited works of other authors, the evaluation of the acquired feature vector was carried out by testing the classifiers built on its basis. As a result, information is provided about the values of various classification quality indicators relevant to the patient from a medical point of view. Noteworthy is also the fact that the automatic osteoporosis diagnosis system, based on the presented extraction of features, would only use descriptors obtained as a result of fractal analysis. The aim of the research presented in this paper is to answer the question whether fractal analysis can be a useful tool for the extraction of feature vector of spinal CT images in the detection of osteoporotic bone defects.

This work is divided into five sections. Section 2 describes the research materials and methods, including image segmentation, fractal analysis methods and feature selection. The obtained results are presented in Sec. 3. Discussion of the results of the fractal analysis is provided in Sec. 4. The conclusions presented in Sec. 5 complete the study.

2. MATERIALS AND METHODS

2.1. Materials

The CT images of the thoraco-lumbar region from 13 healthy patients and 11 patients with osteoporosis were used for the analysis. The decision whether a given CT image belonged to the healthy or sick person was made by a medical specialist (an expert in the field) on the basis of clinical tests. From a series of images, cross-sections were selected on which the inside of the vertebra together with the spongy being was visible. The size of the separated samples was chosen so as to maximize the surface of the texture containing the potential information in the image of a vertebra with a cross-section. As a result, 142 ROIs with dimensions of 50×50 pixels were obtained, where 68 samples (*healthy*) presented normal tissue structure and 74 samples (*sick*) showed defects in spongy tissue because of osteoporosis. Then, all the ROIs were converted from RGB to 8-bit grayscale and normalized in the brightness range with a linear correction (Fig. 1). All pre-processing operations were carried out in the MATLAB program.

2.2. Fractal Analysis

A computer representation of a medical image (e.g. radiological, ultrasound or computer tomography)

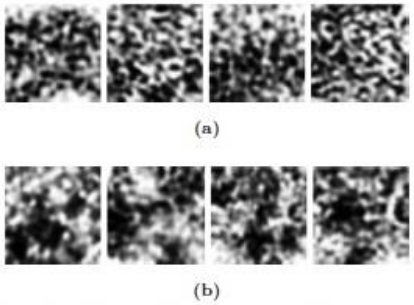

Fig. 1 Examples of ROIs for the analyzed categories: **(a)** healthy and **(b)** sick.

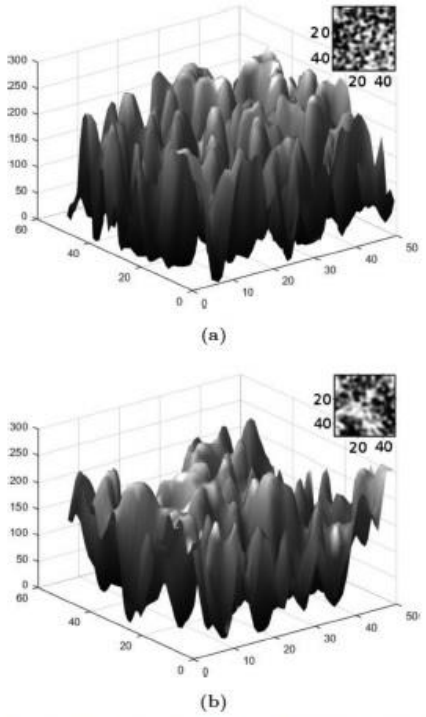

Fig. 2 Sample ROIs and their representations in three-dimensional space: **(a)** healthy and **(b)** sick.

is an image matrix where grayscale (intensity) levels corresponding to the elements x and y form a more or less complex surface (Fig. 2). There are many algorithms for estimating the fractal dimension of such surfaces. In this paper, methods based on power spectral density, triangular prism surface area and variation were used, as well as the box counting method, which in the analysis used a binary image form. The aforementioned methods gave good results in other studies performed by the authors in which the thyroid ultrasound images were the subject of the analysis.[20]

2.2.1. *Image segmentation*

The gray images to be analyzed using the box counting method were segmented. As a result of this process, binary images were obtained, on the basis of which the fractal dimension and lacunarity were calculated. Initially, the results of several segmentation methods were compared, including local and global Otsu thresholding,[21] local Bradley thresholding,[22] level set method, adaptive thresholding and active contour method. All methods have been implemented in the MATLAB program. The disease state of the tissue is visible in CT images in the form of enlarged dark spots. Therefore, the basic criterion for the quality of segmentation was faithful reconstruction of this type of areas. The best results were achieved using the global Bradley thresholding method. Therefore, in further studies, this method was chosen for segmentation of gray images. Exemplary segmentation results are shown in Fig. 3.

2.2.2. *Power spectral density method*

In the case of image matrix $M \times M$, the discrete Fourier transform has the following form:

$$F(u,v) = \sum_{x=0}^{M-1}\sum_{y=0}^{M-1} f(x,y) \times \exp\left(-\frac{2\pi i}{M}(xu+yv)\right), \quad (1)$$

where u and v are spatial frequencies (horizontal and vertical); $0 \le u,\ v \le M-1$; and $0 \le x,\ y \le M-1$. If we define the transforms on a rectangle, then different values for both sums are assumed. The power spectrum $P(u,\ v)$ is calculated as the sum of squares of the real and imaginary Fourier coefficients of the function $F(u,\ v)$,

$$P(u,v) = |F(u,v)|^2 = F(u,v)\cdot F^*(u,v) = F_R^2(u,v) + F_I^2(u,v). \quad (2)$$

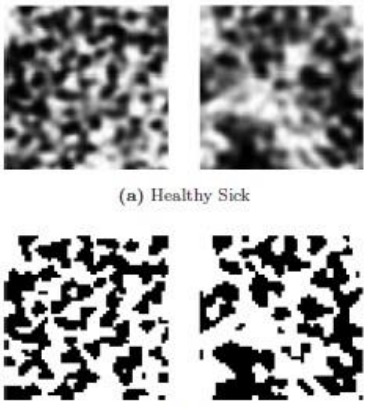

Fig. 3 Example results of image segmentation using the local Bradley thresholding method: **(a)** gray images and **(b)** binary images.

In the case of an isotropic surface, determined by the fractional Brown function, $P(u,v)$ is proportional to a power of the radial frequency ρ (Ref. 23),

$$\rho = (u^2 + v^2)^{\frac{1}{2}}, \tag{3}$$

i.e.

$$P(u,v) = C \cdot \left((u^2 + v^2)^{\frac{1}{2}}\right)^{-\beta} = C \cdot \rho^{-\beta}. \tag{4}$$

Assuming $f = \rho$, we obtain the power law of the form

$$P(f) = C \cdot f^{-\beta}, \tag{5}$$

where C is the scaling constant and β is the slope of the graph of $\log(P(f))$ versus $\log(f)$. This graph is a straight line for fractal surfaces. The relationship between slope β and the fractal dimension D has the following form[24]:

$$\beta = 8 - 2D. \tag{6}$$

Two image descriptors using the power spectral density method were obtained. The first one was the fractal dimension estimated by Eq. (6). The second descriptor was the y-intercept, hereafter referred to as the intercept. Its value is determined on the graph of $\log(P(f))$ versus $\log(f)$ at the point where the straight line crosses the y-axis. The power spectral density method was implemented in the MATLAB program.

2.2.3. *Triangular prism surface area method*

The triangular prism surface area method uses image modeling using prisms which have triangles in the base (Fig. 4). Four adjacent image elements ($\varepsilon = 1$) are taken into account. If a, b, c and d correspond to grays, then their mean value is: $e = (a + b + c + d)/4$. Four triangles can be designated by combining a, e and b; b, e and c; and so on. On this basis, we can calculate the S area that is the sum of the triangular fields ADE, BAE, CBE and DCE. If we repeat the operation for all elements of the image matrix of a given ROI, we obtain the surface $S(\varepsilon)$. The above procedure is performed for different values of ε. The fractal dimension is estimated by the slope of the linear regression $\log(S(\varepsilon))$ versus $\log(\varepsilon)$. The relationship between $S(\varepsilon)$ and ε has the form[25]:

$$S(\varepsilon) = C \cdot \varepsilon^{2-D}, \tag{7}$$

where C is the scaling constant and D is the fractal dimension. This method was used among others for the localization of brain tumors in images obtained by nuclear magnetic resonance.[26] The triangular prism surface area method was implemented in the C language on the basis of Clarke's algorithm.[25]

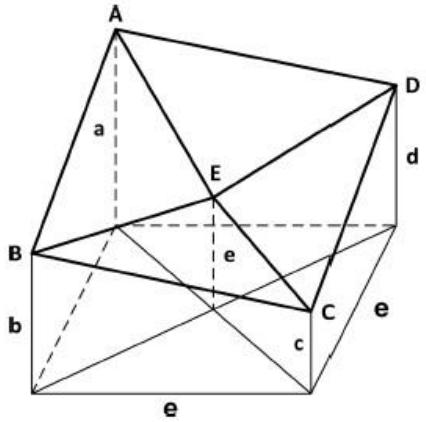

Fig. 4 Modeling of fractal surface with prisms.

2.2.4. *Variation method*

Let us assume that the spatial stochastic process, indexed by the unit square in R^2, is sampled on a regular grid. We then get a surface plot as follows:

$$\left\{(t, X_t) : t = \begin{pmatrix} t_1 \\ t_2 \end{pmatrix} = \frac{1}{n}\begin{pmatrix} i_1 \\ i_2 \end{pmatrix}, \; i_1 = 0, 1, \ldots, n, i_2 = 0, 1, \ldots, n\right\} \subset R^3, \tag{8}$$

where t is a spatial point in R^2; X_t is an observation recorded at point t; and n is the number of observations. For $k > 0$, we have

$$S(k) = \left\{(i_1, i_2, j_1, j_2) \in \{0, 1, \ldots, n\}^4 : \left|\begin{pmatrix} i_1 \\ i_2 \end{pmatrix} - \begin{pmatrix} j_1 \\ j_2 \end{pmatrix}\right| = k\right\}, \tag{9}$$

where $|\cdot|$ is an absolute value of the difference of binomials and $N(k)$ is the size of the above set. If $N(k) > 1$, we treat k as the appropriate distance. The estimators of the fractal dimension, which will be presented later in this subsection, will take the

following form[27]:

$$\hat{D} = 2 - \frac{1}{p}\left\{\sum_{k\in K}(s_k - \bar{s})\log\hat{V}_p(k/n)\right\} \times \left\{\sum_{k\in K}(s_k - \bar{s})^2\right\}^{-1}, \quad (10)$$

where K is a finite set of distances; $s_k = \log(k/n)$; $\bar{s}$ is the average from the set $\{s_k : k \in K\}$ and $\hat{V}_p(k/n)$ is a certain variation with general power index $p > 0$. For $p = 2$, 1 and 0.5, we get the variogram, madogram and rodogram, respectively. In this study, we used a madogram ($p = 1$) and the set of distances $K = \{2, 2\sqrt{2}, 4\}$. Variations were taken into account for the horizontal and vertical distances of first and second points on the grid ($k = 2$ and 4) and for the diagonal distance of individual grid points ($k = 2\sqrt{2}$).

The research applied two methods using linear cross-sections of data. The first one was based on first-order differences, while the second one was based on second-order differences. Both methods use the generalization of the variogram moment estimator.[27]

First-order differences estimator. For time series or linear cross-sections of the given figures:

$$\left\{(t, X_t) : t = \frac{i}{n},\ i = 0, 1, \ldots, n\right\} \subset R^2 \quad (11)$$

and first-order differences, we get a power variation of order p:

$$\hat{V}_{\mathrm{FD};p}(l/n) = \frac{1}{2(n-l)}\sum_{i=l}^{n} \times |X_{i/n} - X_{(i-l)/n}|^p, \quad (12)$$

$$\hat{V}_{\mathrm{FD};1}(l/n) = \frac{1}{2(n-l)}\sum_{i=l}^{n} |X_{i/n} - X_{(i-l)/n}| \times (\text{for } p = 1), \quad (13)$$

where l/n is the scale and l is the distance between observations ($l = 1, 2, \ldots$).

A p-level variation estimator for the fractal dimension has the form

$$\hat{D}_{\mathrm{FD};p} = 2 - \frac{1}{p}\left\{\sum_{l=1}^{L}(s_l - \bar{s})\log\hat{V}_{\mathrm{FD};p}(l/n)\right\} \times \left\{\sum_{l=1}^{L}(s_l - \bar{s})^2\right\}^{-1}, \quad (14)$$

$$\hat{D}_{\mathrm{FD};1} = 2 - \left\{\sum_{l=1}^{L}(s_l - \bar{s})\log\hat{V}_{\mathrm{FD};1}(l/n)\right\} \times \left\{\sum_{l=1}^{L}(s_l - \bar{s})^2\right\}^{-1} \quad (\text{for } p = 1), \quad (15)$$

where $L \geq 2$, $s_l = \log(l/n)$ and $\bar{s}$ is the average of $s_l, \ldots, s_L$.

Second-order differences estimator. For second-order differences, we have

$$\hat{V}_{\mathrm{SD};p}(l/n) = \frac{1}{2(n-2l)}\sum_{i=l}^{n-l} |X_{(i+l)/n} - 2X_{i/n} + X_{(i-l)/n}|^p, \quad (16)$$

$$\hat{V}_{\mathrm{SD};1}(l/n) = \frac{1}{2(n-2l)}\sum_{i=l}^{n-l} |X_{(i+l)/n} - 2X_{i/n} + X_{(i-l)/n}| \quad (\text{for } p = 1). \quad (17)$$

A p-level variation estimator for the fractal dimension has the form

$$\hat{D}_{\mathrm{SD};p} = 2 - \frac{1}{p}\left\{\sum_{l=1}^{L}(s_l - \bar{s})\log\hat{V}_{\mathrm{SD};p}(l/n)\right\} \times \left\{\sum_{l=1}^{L}(s_l - \bar{s})^2\right\}^{-1}, \quad (18)$$

$$\hat{D}_{\mathrm{SD};1} = 2 - \left\{\sum_{l=1}^{L}(s_l - \bar{s})\log\hat{V}_{\mathrm{SD};1}(l/n)\right\} \times \left\{\sum_{l=1}^{L}(s_l - \bar{s})^2\right\}^{-1} \quad (\text{for } p = 1). \quad (19)$$

Filter 1 estimator. In the tests, an approach based on the *Filter* 1 estimator was used, which was proposed by Zhu and Stein.[28] This technique has been generalized by defining the filter estimator with the general exponent $p > 0$ (not $p = 2$, as proposed by Zhu and Stein[28]). Accordingly, for the distance $k > 0$, we have the following variation with the general power exponent $p > 0$ (Ref. 27):

$$\hat{V}_{F;p}(k/n) = \frac{1}{2N(k)}\sum_{S(k)} |X_{i_1/n,\, i_2/n} - 2X_{(i_1+j_1)/(2n),\,(i_2+j_2)/(2n)} + X_{j_1/n,\, j_2/n}|^p, \quad (20)$$

$$\hat{V}_{F;1}(k/n) = \frac{1}{2N(k)} \sum_{S(k)} |X_{i_1/n, i_2/n} - 2X_{(i_1+j_1)/(2n), (i_2+j_2)/(2n)} + X_{j_1/n, j_2/n}| \quad (\text{for } p = 1). \tag{21}$$

The filter estimator with the power exponent p is defined as follows:

$$\hat{D}_{F;p} = 2 - \frac{1}{p}\left\{\sum_{k\in K}(s_k - \bar{s}) \log \hat{V}_{F;p}(k/n)\right\} \times \left\{\sum_{k\in K}(s_k - \bar{s})^2\right\}^{-1}, \tag{22}$$

$$\hat{D}_{F;1} = 2 - \left\{\sum_{k\in K}(s_k - \bar{s}) \log \hat{V}_{F;1}(k/n)\right\} \times \left\{\sum_{k\in K}(s_k - \bar{s})^2\right\}^{-1} \quad (\text{for } p = 1). \tag{23}$$

All estimators of the variation method determine m image cross-sections and for each of them the fractal dimension estimates $\hat{D}_i$ $(i = 1, 2, \ldots, m)$ are calculated. In this study, a set of estimators $\{\hat{D}_i\}$ was obtained for the sections made in accordance with the directions: horizontal, vertical and diagonal with positive and negative gradients. The median of this set gives the final value of the cross-section estimation. The fractal dimension of the entire surface of the image is obtained according to relationship[27]

$$D = 1 + \text{median}\{\hat{D}_i\}. \tag{24}$$

During the analysis, the R program's *fractaldim* package was used, in which the estimators of the variation method discussed earlier were implemented. To calculate the values of Var_FD, Var_SD and Filter variables, estimators defined by the formulas (15), (19) and (23) were used, respectively.

2.2.5. *Box counting method*

In order to calculate the fractal dimension using the box counting method, the image to be examined is placed on a regular grid consisting of elements with sides equal to ε, and then the grid elements (boxes) covering the picture are counted. The number we get $[N(\varepsilon)]$ depends on the size of the grid elements. In further iterations, the value ε is gradually reduced and the corresponding values $N(\varepsilon)$ are determined. The essence of the estimation of the fractal dimension consists in observing how $N(\varepsilon)$ changes when changing ε. It should be noted here that ε is a fraction of the contractual unit length. Depending on the size of the examined objects, the unit length may vary.

For images occurring in nature (including medical images), the number of elements appearing in subsequent iterations is not constant, therefore the fractal dimension is defined as the limit value, where the length of the box goes to zero. Assuming that $N(\varepsilon)$ is the number of boxes with the side length ε covering the image, the fractal dimension estimated by the box counting method (assuming that the boundary exists) is defined by the relation

$$D = -\lim_{\delta\to 0} \frac{\log(N(\varepsilon))}{\log(1/\varepsilon)}. \tag{25}$$

Practically, D is defined by drawing a $\log(N(\varepsilon))$ graph with respect to the $\log(1/\varepsilon)$ function and approximating it with a straight line. The slope of the straight line obtained is an estimate of the fractal dimension.

The box counting method was also used to determine the lacunarity of images. This concept was introduced by Mandelbrot for the additional distinction between figures having the same fractal dimension.[29] In order to determine the lacunarity, two sizes are calculated for each ε-sized box. The first is the sum of the number of pixels in each box $Q_1 = \sum_i p(i, \varepsilon)$. The second size is the sum of the squares of the number of pixels in each box $Q_2 = \sum_i p(i, \varepsilon)^2$. On this basis, the lacunarity for the ε-sized box is defined as

$$L(\varepsilon) = \frac{N(\varepsilon)Q_2}{Q_1^2}, \tag{26}$$

where $N(\varepsilon)$ is the number of ε-sized boxes; $p(i,\varepsilon)$ is the number of pixels in the ith box; and $i \in [1, N(\varepsilon)]$. The estimation of lacunarity is based on the log–log $L(\varepsilon)$ graph with respect to function ε (similarly to the fractal dimension). The coarseness of a given image describes the empty space around the object (hole), thus defining how the object fills the space in the image.[30] The analysis, aimed at calculating the fractal dimension using the box method and lacunarity, was carried out in the ImageJ program.

2.3. Feature Selection

The subject of the methods for feature selection is very extensive and is still an area of active research.

Generally, these methods can be divided into: wrappers — a given subset of features is evaluated using a classifier; embedded methods — the selection process is included in the classifier's learning; and filter methods — they only analyze internal data properties (they do not use the classifier). In this study, a linear stepwise regression method was used, belonging to the third of the previously mentioned groups. It has the advantage that only statistically significant variables are introduced to the model, i.e. predictors that actually "improve" the model built. The linear stepwise regression method involves the systematic addition and elimination of features to the set of input attributes given to the input of the linear classifier model depending on their statistical impact on the result of the system operation. The influence of a feature on the operation of the system is measured by the factor with which it enters the linear model. The method starts from the start-up model, comparing its performance when increasing or decreasing the number of input attributes selected from the full set of potential diagnostic features. At every step (after adding or subtracting a specific attribute), the F-Snedecor statistics are determined for the training set. On the basis of a comparison of the p-value of this statistic with the assumed $p_$enter tolerance, a decision is made whether a specified feature should be entered into the set of features or not. In turn, as a result of comparing the p-value of the F-statistic with the assumed $p_$remove tolerance, a decision is made to remove (or not) a specified feature from the current set of features.

If the specified feature is not in the current set of input attributes, the null hypothesis is tested that its effect on the model's operation is zero. If the hypothesis is not confirmed as a result of the calculation, the attribute is added to the current set of attributes. Conversely, if a particular feature is in the model's input attribute set, the hypothesis is tested that its effect is zero. If this hypothesis is not confirmed, the feature remains in the attribute collection, but if confirmed, it is deleted.

3. RESULTS

Images belonging to the *healthy* and *sick* categories were subjected to fractal analysis in order to obtain the feature descriptors. The following methods were applied (Sec. 2.2): power spectral density, triangular prism surface area, variation (transect: first and second differences and filter 1 estimators) and box counting. On the basis of the power spectral density method, the fractal dimension and intercept of gray images were obtained. The box counting method allowed to estimate the fractal dimension and lacunarity of binary images. The effect of the triangular prism surface area and variation methods was the fractal dimension of gray images.

Table 1 presents a summary of average values of individual descriptors and their standard deviations. For a binary image, the fractal dimension is in the range of 1–2, and for the gray one in the range of 2–3. These values are in line with the theoretical values for these types of images. This situation

Table 1 Mean Values and Standard Deviations of Fractal Descriptors.

Image	Method	Descriptor	Variable	Class	Mean ± SD
Gray	Power spectral density	Fractal dimension	PSD	Healthy	2.42 ± 0.08
				Sick	2.33 ± 0.13
Gray	Power spectral density	Intercept	Int	Healthy	22.57 ± 0.33
				Sick	22.88 ± 0.48
Gray	Triangular prism surface area	Fractal dimension	TPSA	Healthy	2.38 ± 0.04
				Sick	2.37 ± 0.05
Gray	Variation (Transect: first differences)	Fractal dimension	Var_FD	Healthy	2.14 ± 0.01
				Sick	2.12 ± 0.02
Gray	Variation (Transect: second differences)	Fractal dimension	Var_SD	Healthy	2.55 ± 0.02
				Sick	2.51 ± 0.04
Gray	Variation (Filter 1)	Fractal dimension	Filter	Healthy	2.55 ± 0.02
				Sick	2.51 ± 0.04
Binary	Box counting	Fractal dimension	BC	Healthy	1.70 ± 0
				Sick	1.69 ± 0.01
Binary	Box counting	Lacunarity	Lac	Healthy	0.27 ± 0.02
				Sick	0.29 ± 0.02

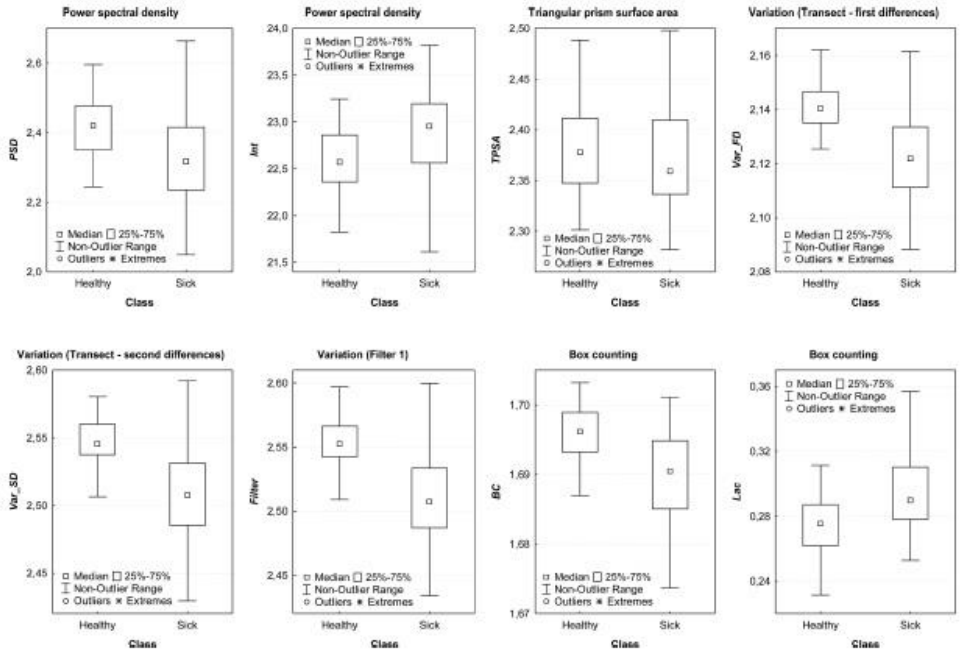

Fig. 5 Dispersions of the values of individual variables. The name of the method used is in the title of each chart. Variables of the specified symbols are described in Table 1

indicates that the analyzed images have fractal features and justify the use of fractal analysis as a method of extracting the feature descriptors.

Box charts for the investigated cases are shown in Fig. 5. They show the dispersion of the value of individual variables. On this basis, we can conclude that the variables Var_FD, Var_SD and Filter best separate observations belonging to the *healthy* and *sick* categories. The values of the above-mentioned variables were estimated using three different estimators based on the variance method.

However, the results of the fractal analysis presented in Table 1 and Fig. 5 do not allow to indicate a set of descriptors that could be used to distinguish clearly between healthy and sick cases. Therefore, the data were subjected to statistical analysis aimed at selecting features that would enable to build the classifier. A linear stepwise regression method was applied for this purpose. The *stepwisefit* function of the MATLAB program was used, in which the aforementioned method was implemented. The built-in values of the F-statistic's tolerance thresholds were as follows: $p\_\text{enter} = 0.05$ and $p\_\text{remove} = 0.1$.

Table 2 Results of Feature Selection by Linear Stepwise Regression.

Variable	B[a]	SE[b]	PV[c]	Status[d]
PSD	0.1013	0.3770	0.7886	0
Int	−0.0808	0.0953	0.3983	0
TPSA	−0.9985	0.6970	0.1543	0
Var_FD	**−9.0866**	**3.6058**	**0.0129**	**1**
Var_SD	1.8604	4.6417	0.6892	0
Filter	**−3.6233**	**1.5195**	**0.0185**	**1**
BC	−10.4602	6.8475	0.1289	0
Lac	**4.3737**	**1.5690**	**0.0061**	**1**

[a] B: Coefficients with which particular features affect the accuracy of model mapping. The greater the value (as to the module), the greater the influence of a given feature.
[b] SE: Standard deviation of the values of B coefficients for individual features.
[c] PV: A p-value variable containing p-statistic values for individual features. The smaller the value, the more difficult it is to reject the hypothesis about the low importance of a given feature.
[d] Status: Value 1 means that the given feature is included as the input attribute of the model, 0 means its elimination.

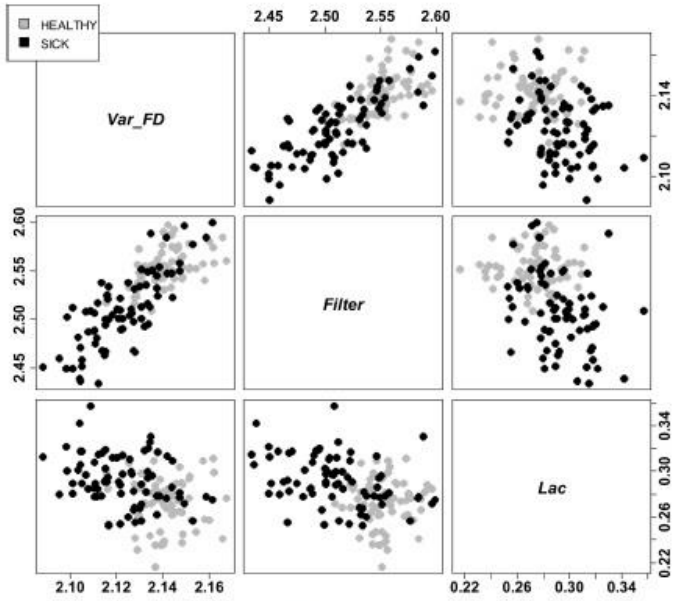

Fig. 6 Scatter plots for the variables selected by linear stepwise regression.

The obtained results (Table 2) show that the most significant effects on the model are those of Var_FD, Filter and Lac (the smallest p-values). They are marked in bold in Table 2. The values of p-statistics for individual features also show the difference in their impacts on the result. The p-value for the Lac variable is more than twice lower than that for Var_FD and three times smaller than that for the Filter variable.

Matrix scatter plots were made for variables selected using the linear stepwise regression method (Fig. 6). It can be seen from the plots that observations of the *healthy* category form a relatively compact group. Apparently, this can be seen for the Var_FD–Filter and Filter–Lac variable pairs. Unfortunately, the observations of the *sick* category have a larger spread of variable values in comparison to the *healthy* cases. Therefore, there are no two clearly separable groups of observations that allow one to clearly distinguish between the two categories. Nevertheless, in the scatter plots one can observe some areas in which observations belonging to particular classes show a certain tendency to group. It seems that this is best seen for the Var_FD–Filter and Filter–Lac variable pairs.

The spatial chart gives slightly better possibilities of observing the grouping of cases. Figure 7 shows

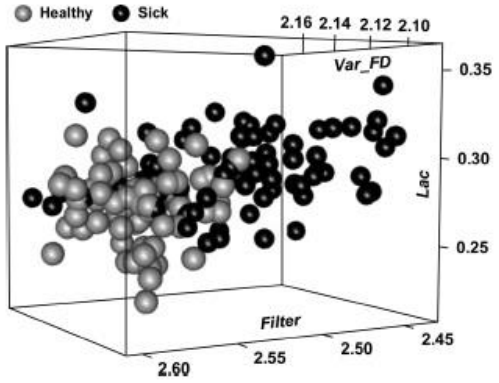

Fig. 7 Spatial scatter plot for the variables Var_FD, Filter and Lac.

such a graph for the variables Var_FD, Filter and Lac. Admittedly, two separate groups of the *sick* and *healthy* categories cannot be seen in the graph, but the characteristic areas of the distribution of these cases can be discerned. This situation justifies the attempt to build classifiers.

In the classification process, three features highlighted in bold font in Table 2 were used: Var_FD, Filter and Lac. The full set of data contained 142

observations, of which 68 were in the *healthy* category and 74 in the *sick* category. From this set, in a random manner, the training and test parts were selected (for the applied classifiers, there was no typical validation process). The size of the training set was 2/3, and the test 1/3 of the full set. The training and testing procedures for classifiers were repeated 10 times. As the final result of the testing process, the average value from all tests was taken. This approach required the preparation of 10 training sets and 10 test sets. Determination of these sets was based on draws with returning. Six popular supervised learning methods were used[31–39]: linear and quadratic discriminant analysis (LDA and QDA), naive Bayes classifier (NBC), decision tree (DT), K-nearest neighbors (K-NN) and random forests (RF). All calculations were done in the R environment.

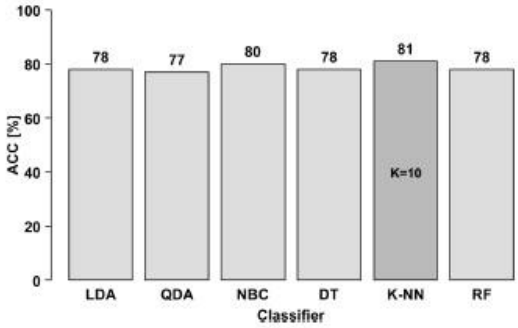

Fig. 8 Overall classification accuracies for the individual classifiers. The meanings of the classifier symbols are as follows: LDA and QDA: linear and quadratic discriminant analyses, NBC: naive Bayes classifier, DT: decision tree, K-NN: K-nearest neighbors and RF: random forests.

To assess the accuracy of classifiers, the following indices were applied:

- Overall classification accuracy (ACC): The ratio of the number of cases correctly classified to the number of all analyzed cases [$\mathrm{ACC} = (\mathrm{TP} + \mathrm{TN})/(\mathrm{TP} + \mathrm{TN} + \mathrm{FP} + \mathrm{FN})$].
- True positive rate (TPR, classification sensitivity): The probability of correct classification of a case as *sick*, provided that it actually belongs to the *sick* class [$\mathrm{TPR} = \mathrm{TP}/(\mathrm{TP} + \mathrm{FN})$].
- True negative rate (TNR, classification specificity): The probability of correct classification of the case as a *healthy* one, provided that it actually belongs to the *healthy* class [$\mathrm{TNR} = \mathrm{TN}/(\mathrm{TN} + \mathrm{FP})$].
- Positive predictive value (PPV): The probability that the case really belongs to the *sick* class, with its positive classification [$\mathrm{PPV} = \mathrm{TP}/(\mathrm{TP} + \mathrm{FP})$].
- Negative predictive value (NPV): The probability that the case really belongs to the *healthy* class, with its negative classification [$\mathrm{NPV} = \mathrm{TN}/(\mathrm{TN} + \mathrm{FN})$].

Here, TP (true positive) denotes the number of *sick* cases classified to the class of *sick* ones; FN (false negative) is the number of *sick* cases classified to the class of *healthy* ones; TN (true negative) denotes the number of *healthy* cases classified to the class of *healthy* ones; and FP (false positive) signifies the number of *healthy* cases classified to the class of *sick* ones.

Figure 8 shows the bar charts showing the general classification accuracies obtained for the test set. The highest value, equal to 81%, was achieved for the classifier K-NN ($K = 10$). A comparable accuracy was also obtained by the NBC classifier, for

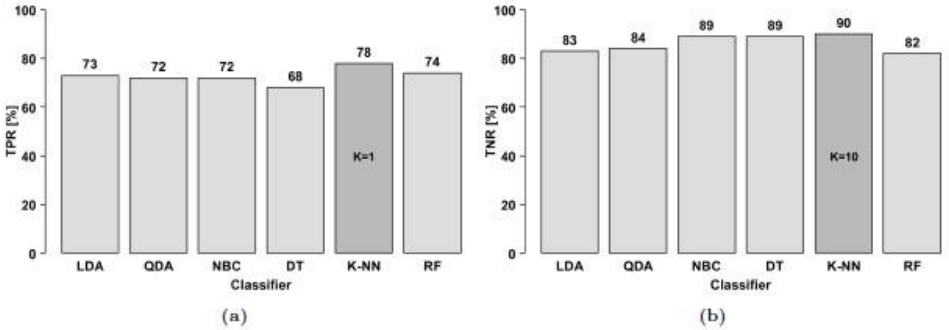

Fig. 9 Classification **(a)** sensitivities and **(b)** specificities for the individual classifiers.

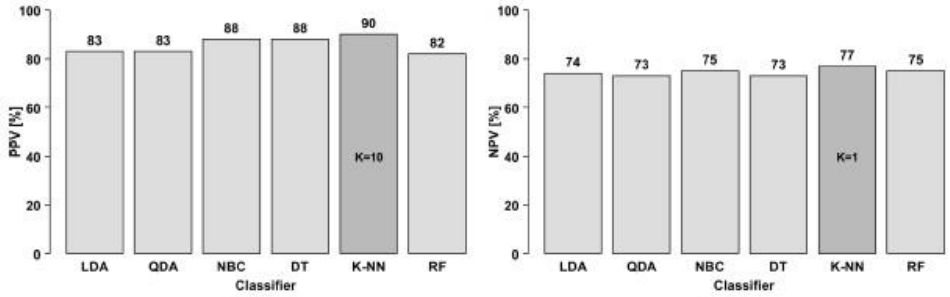

Fig. 10 **(a)** Positive predictive values and **(b)** negative predictive values for the individual classifiers.

which ACC was equal to 80%. For all classification methods, ACC was equal to or greater than 77%. The results regarding the sensitivity and specificity of the classification are presented in Figs. 9a and 9b, respectively. The highest sensitivity, equal to 78%, was achieved for the K-NN classifier ($K = 1$). In the case of specificity, the best result — equal to 90% — was also obtained for the K-NN classifier ($K = 10$). The fairly large difference between sensitivity and specificity of classification, amounting to 12%, results from a much larger scatter of variable values for the cases of the *sick* class, compared to the cases of the *healthy* class (as shown in Fig. 6). Bar charts showing the results for the positive and negative predictive values are shown in Figs. 10a and 10b, respectively. The PPV index, equal to 90%, was the highest for the classifier K-NN ($K = 10$). In turn, NPV obtained the largest value (77%) also for the classifier K-NN ($K = 1$). The difference between these values (13%) results from a fairly large dispersion of the *sick* category, resulting in some of them being classified as *healthy* ones.

4. DISCUSSION

The study used eight fractal descriptors estimated by various methods. The ranges of changes in their values confirm the fractal nature of the CT images being studied (Table 1) and justify the use of fractal analysis as a tool of feature vector extraction. From among this set, three descriptors for constructing classifiers were selected using the linear stepwise regression method. These were: two fractal dimensions calculated by the variation method (transect: first differences and filter 1 estimators) and lacunarity calculated by the box counting method. The first two descriptors (Var_FD and Filter) were calculated on the basis of a gray image analysis, while the third (Lac) was based on a binary image.

Table 3 **A Summary of the Best Classification Results shown in Figs. 8–10.**

Index	Value (%)	Classifier
ACC[a]	81	K-NN ($K = 10$)
TPR[b]	78	K-NN ($K = 1$)
TNR[c]	90	K-NN ($K = 10$)
PPV[d]	90	K-NN ($K = 10$)
NPV[e]	77	K-NN ($K = 1$)

[a]Overall classification accuracy.
[b]True positive rate (classification sensitivity).
[c]True negative rate (classification specificity).
[d]Positive predictive value.
[e]Negative predictive value.

Table 3 provides a summary of the best results obtained while testing the classifiers. They are as follows: ACC = 81%, TPR = 78%, TNR = 90%, PPV = 90% and NPV = 77%. It is worth noting that in each case the best result was obtained for the K-NN classifier (for the number of K-nearest neighbors equal to 1 or 10). The value of the TPR parameter is much lower than the TNR value. The same situation applies to the other two parameters, i.e. PPV and NPV. Unfortunately, such relationships between the values of the listed quality classification indices are not beneficial to the patient from the medical point of view. They mean that some cases of the *sick* category would be classified as *healthy* ones. Therefore, further research is required to find such features that have a smaller dispersion of values for the *sick* cases. It seems that good results might be achieved by combining the effects of fractal analysis with the results of other methods for texture feature

extraction, e.g. autoregression model, wavelet transform and statistical methods (grayscale histogram, co-occurrence matrix, higher-order statistics, run-length matrix and gradient matrix).[40]

The results obtained are difficult to compare with the results of other authors, because (as noted in the introduction) there are no known publications presenting classification results aimed at the detection of osteoporosis, where the fractal analysis of spine CT images on the thoraco-lumbar region would be used to extract the textural features. The advantages of the presented method include the fact that it is noninvasive and offers an acceptable (from a medical point of view) accuracy of recognizing cases belonging to particular categories. In addition, the method is based on only three features selected solely on the basis of fractal analysis. This situation should simplify the implementation of the future computer system. On the other hand, a certain drawback of the applied method of analysis is the fact that there is a lack of standardization of methods for estimating the fractal dimension. Consequently, the values of this parameter for the same image, estimated by different methods, are similar but not identical. In addition, the range of the estimation of the slope of regression line can be determined in various ways, which influences the value of the estimated parameter. Finally, the presented method must be tested on datasets of a larger size. Future studies should also consider the impact of changes in size and position of the ROIs on the results. Despite the problems indicated, fractal analysis seems to be an interesting tool for extracting the feature vector in the study of textures of spinal CT images. Relatively high classification accuracy, achieved thanks to the fractal descriptors, gives a chance to use them in a computer system aimed at recognizing osteoporotic bone defects.

5. CONCLUSIONS

A set of feature descriptors provided by the fractal analysis allowed to obtain the following results: overall classification accuracy: 81%, classification sensitivity: 78%, classification specificity: 90%, positive predictive value: 90% and negative predictive value: 77%. Achieving a relatively high accuracy of classification was possible due to the simultaneous use of fractal descriptors of the gray and binary images. These were two fractal dimensions calculated by the variation method (two different estimators) and fractal lacunarity calculated by the box counting method. Research showed that the fractal analysis can be an alternative approach in the study of spinal CT images to recognize bone damage caused by osteoporosis. Its results, combined with the K-NN classifier, could be applied in the construction of a computer system that would support the physician in the initial diagnosis of difficult cases based on CT images. Thanks to this, the physician would have a quick and objective additional opinion that would be very valuable at the initial diagnosis stage. In the case of osteoporosis, this is particularly important because the detection of the disease at an early stage increases the patient's chances of effective therapy.

REFERENCES

1. P. A. Downey and M. I. Siegel, Bone biology and the clinical implications for osteoporosis, *Phys. Ther.* **86** (2006) 77–91.
2. R. Marcus, D. Feldman, D. Dempster, M. Luckey and J. Cauley, *Osteoporosis*, 4th edn. (Academic Press, 2013).
3. C. Reshmalakshmi and M. Sasikumar, Trabecular bone quality metric from X-ray images for osteoporosis detection, in *Proceedings of the* 2017 *International Conference on Intelligent Computing, Instrumentation and Control Technologies* (*ICICICT*), Kerala, India, 2017, pp. 1694–1697.
4. Y. Nasser, M. Hassouni, A. Brahim, H. Toumi, E. Lespessailles and R. Jennane, Diagnosis of osteoporosis disease from bone X-ray images with stacked sparse autoencoder and SVM classifier, in *Proceedings of the* 2017 *International Conference on Advanced Technologies for Signal and Image Processing (ATSIP)*, Fez, Morroco, 2017, pp. 1–5.
5. C. Reshmalakshmi and M. Sasikumar, Fuzzy inference system for osteoporosis detection, in *Proceedings of the* 2016 *IEEE Global Humanitarian Technology Conference* (*GHTC*), Seattle, WA, 2016, pp. 675–681.
6. E. Tejaswini, P. Vaishnavi and R. Sunitha, Detection and prediction of osteoporosis using impulse response technique and artificial neural network, in *Proceedings of the* 2016 *International Conference on Advances in Computing, Communications and Informatics* (*ICACCI*), Jaipur, India, 2016, pp. 1571–1575.
7. K. Shahabaz, D. K. Somwanshi, A. K. Yadav and R. Roy, Medical images texture analysis: A review, in *Proceedings of the* 2017 *International Conference on Computer, Communications and Electronics* (*Comptelix*), Jaipur, India, 2017, pp. 436–441.

8. M. Strzelecki and A. Materka, *Tekstura obrazów biomedycznych: Metody analizy komputerowej* (Wydawnictwo Naukowe PWN, Wydawca, 2017).
9. P. Leszczyński and J. Sokalski, The use of fractal analysis in medicine: A literature review, *Dent. Med. Probl.* **54** (2017) 79–83.
10. A. J. Camargo, A. R. G. Côrtes, E. M. Aoki, M. G. Baladi, E. S. Arita and P. C. A. Watanabe, Analysis of bone quality on panoramic radiograph in osteoporosis research by fractal dimension, *Appl. Math.* **7** (2016) 375–386.
11. E. Güngör, D. Yildirim and R. Çevik, Evaluation of osteoporosis in jaw bones using cone beam CT and dual-energy X-ray absorptiometry, *J. Oral Sci.* **58** (2016) 185–194.
12. R. A. Mostafa, E. A. Arnout and M. M. Abo El-Fotouh, Feasibility of cone beam computed tomography radiomorphometric analysis and fractal dimension in assessment of postmenopausal osteoporosis in correlation with dual X-ray absorptiometry, *Dentomaxillofac. Radiol.* **45** (2016) 20160212.
13. K. Vijayalakshmi, C. L. Krithika, P. H. Raghuram and A. Kannan, Fractal analysis of trabecular bone pattern in the mandible as an indicator of osteoporosis in women: A clinical study, *Asian J. Pharm. Clin. Res.* **11** (2018) 157–160.
14. K. Harrar and R. Jennane, Trabecular texture analysis using fractal metrics for bone fragility assessment, *Int. J. Med. Health Biomed. Bioeng. Pharm. Eng.* **9** (2015) 618–623.
15. A. Tafraouti, M. El-Hassouni, H. Toumi, E. Lespessailles and R. Jennane, Osteoporosis diagnosis using fractal analysis and support vector machine, in *Proceedings of the 2014 Tenth International Conference on Signal-Image Technology & Internet-Based Systems*, Marrakech, Morocco, 2014, pp. 73–77.
16. A. Taleb-Ahmed, P. Dubois and E. Duquenoy, Analysis methods of CT-scan images for the characterization of the bone texture: First results, *Pattern Recognit. Lett.* **24** (2003) 1971–1982.
17. M. Czyz, A. Kapinas, J. Holton, R. Pyzik, B. M. Boszczyk and N. A. Quraishi, The computed tomography-based fractal analysis of trabecular bone structure may help in detecting decreased quality of bone before urgent spinal procedures, *Spine J.* **17** (2017) 1156–1162.
18. G. Dougherty and G. M. Henebry, Lacunarity analysis of spatial pattern in CT images of vertebral trabecular bone for assessing osteoporosis, *Med. Eng. Phys.* **24** (2002) 129–138.
19. A. Zaia, Fractal lacunarity of trabecular bone and magnetic resonance imaging: New perspectives for osteoporotic fracture risk assessment, *World J. Orthop.* **6** (2015) 221–235.
20. Z. Omiotek, Fractal analysis of the grey and binary images in diagnosis of Hashimoto's thyroiditis, *Biocybern. Biomed. Eng.* **37** (2017) 655–665.
21. N. Otsu, A threshold selection method from gray-level histograms, *IEEE Trans. Syst. Man Cybern.* **9** (1979) 62–66.
22. D. Bradley and G. Roth, Adaptive thresholding using the integral image (2007), http://www.scs.carleton.ca/~/iit-publications-iti/docs/gerh-50002.pdf.
23. T. J. Dennis and N. G. Dessipris, Fractal modelling in image texture analysis, *IEE Proc. F Radar Signal Process.* **136** (1989) 227–235.
24. B. J. Super and A. C. Bovik, Localized measurement of image fractal dimension using Gabor filters, *J. Vis. Commun. Image Represent.* **2** (1991) 114–128.
25. K. C. Clarke, Computation of the fractal dimension of topographic surfaces using the triangular prism surface area method, *Comput. Geosci.* **12** (1986) 713–722.
26. K. M. Iftekharuddin, W. Jia and R. Marsh, Fractal analysis of tumor in brain MR images, *Mach. Vis. Appl.* **13** (2003) 352–362.
27. T. Gneiting, H. Sevcikova and D. Percival, Estimators of fractal dimension: Assessing the roughness of time series and spatial data, *Stat. Sci.* **27** (2012) 247–277.
28. Z. Zhu and M. Stein, Parameter estimation for fractional Brownian surfaces, *Stat. Sin.* **12** (2002) 863–883.
29. B. Mandelbrot, *The Fractal Geometry of Nature* (W. H. Freeman and Company, New York, 1983).
30. R. E. Plotnick, R. H. Gardner and R. V. O'Neil, Lacunarity indices as measures of landscape texture, *Landsc. Ecol.* **8** (1993) 201–211.
31. L. Breiman, J. Friedman, C. J. Stone and R. A. Olshen, *Classification and Regression Trees* (CRC Press, London, 1984).
32. G. G. Enas and S. C. Chai, Choice of the smoothing parameter and efficiency of the k-nearest neighbor classification, *Comput. Math. Appl.* **12** (1986) 235–244.
33. S. H. Liao, P. H. Chu and P. Y. Hsiao, Data mining techniques and applications: A decade review from 2000 to 2011, *Expert Syst. Appl.* **39** (2012) 11303–11311.
34. J. R. Quinlan, Induction of decision trees, *Mach. Learn.* **1** (1986) 81–106.
35. L. Breiman, Bagging predictors, *Mach. Learn.* **24** (1996) 123–140.
36. L. Breiman, Random forests, *Mach. Learn.* **45** (2001) 5–32.
37. W. N. Venables and B. D. Ripley, *Modern Applied Statistics with S-PLUS* (Springer, Berlin, 1998).

38. Y. Freund and R. E. Schapire, A decision-theoretic generalization of on-line learning and an application to boosting, *J. Comput. Syst. Sci.* **55** (1996) 119–139.
39. T. Hothorn and B. Lausen, Bundling classifiers by bagging trees, *Comput. Stat. Data Anal.* **49** (2005) 1068–1078.
40. Z. Omiotek, Improvement of the classification quality in detection of Hashimoto's disease with a combined classifier approach, *Proc. Inst. Mech. Eng. H J. Eng. Med.* **231** (2017) 774–782.

2150095-15

Lublin, 20.12.2022

Dr hab. inż. Zbigniew Omiotek, prof. Uczelni
Wydział Elektrotechniki i Informatyki
Politechnika Lubelska

Oświadczenie współautora

Oświadczam, iż mój udział w przygotowaniu publikacji:

1. *Fractal analysis as a method for feature extraction in detecting osteoporotic bone destruction,* Zbigniew Omiotek, **Róża Dzierżak**, Andrzej Kępa / Fractals : Complex Geometry, Patterns, and Scaling in Nature and Society, 2021, vol. 29, nr 4, s. 1-15, (2021).

wchodzącej w skład rozprawy doktorskiej Pani dr inż. Róży Dzierżak polegał na opracowaniu koncepcji i metodologii badań oraz przeprowadzeniu symulacji i wstępnej analizy otrzymanych wyników.

Zbigniew Omiotek
Podpis

Lublin, 20.12.2022

mgr Andrzej Kępa
Zakład Radiologii Lekarskiej
Samodzielny Publiczny Szpital Kliniczny nr 4
w Lublinie

Oświadczenie współautora

Oświadczam, iż mój udział w przygotowaniu publikacji:

1. *Fractal analysis as a method for feature extraction in detecting osteoporotic bone destruction,* Zbigniew Omiotek, **Róża Dzierżak**, Andrzej Kępa / Fractals : Complex Geometry, Patterns, and Scaling in Nature and Society, 2021, vol. 29, nr 4, s. 1-15, (2021).

wchodzącej w skład rozprawy doktorskiej Pani dr inż. Róży Dzierżak polegał na zgromadzeniu danych obrazowych.

Podpis

4.4 *The influence of the normalisation of spinal CT images on the significance of textural features in the identification of defects in the spongy tissue structure*

Autorzy: **Róża Dzierżak**, Zbigniew Omiotek, Ewaryst Tkacz, Andrzej Kępa

Opublikowano: [W] Tkacz, E., Gzik, M., Paszenda, Z., Piętka, E. (eds) Innovations in Biomedical Engineering. IBE 2018. Advances in Intelligent Systems and Computing, vol 925. Springer - 2019, s. 55−66.
DOI: https://doi.org/10.1007/978-3-030-15472-1_7

Liczba punktów ministerialnych: **20**

Udział pierwszego autora w poniżej załączonym artykule polegał na opracowaniu koncepcji badań, analizie otrzymanych wyników oraz przygotowaniu manuskryptu (50%). Wkład współautorów, w formie oświadczenia, zamieszczono na końcu artykułu.

Celem badań było określenie wpływu normalizacji obrazów CT kręgosłupa na dokładność automatycznego rozpoznawania ubytków w strukturze tkanki gąbczastej kręgów na odcinku piersiowo-lędźwiowym. Deskryptory cech oparte były na histogramie poziomów szarości, macierzy gradientu, macierzy RL, macierzy zdarzeń, modelu autoregresji i transformacie falkowej. Zastosowano 6 metod selekcji cech: współczynnik Fishera, minimalizację prawdopodobieństwa błędu klasyfikacji wraz z zakumulowanym współczynnikiem korelacji, informację wzajemną, korelację Spearmana, heurystyczną identyfikację zmiennych zakłócających, liniową regresję krokową. Wyniki selekcji użyto do budowy 6 popularnych klasyfikatorów. Uzyskano następujące wartości poszczególnych współczynników jakości klasyfikacji (przed normalizacją / po normalizacji): ogólna dokładność klasyfikacji – 90%/82%, wrażliwość klasyfikacji – 89%/85%, specyficzność klasyfikacji – 96%/82%, wartość predykcyjna dodatnia – 95%/95%, wartość predykcyjna ujemna – 89%/84%. Dla zastosowanego zbioru cech teksturalnych, oraz metod selekcji i klasyfikacji, normalizacja obrazu zdecydowanie pogorszyła dokładność automatycznego rozpoznawania osteoporozy na podstawie zdjęć CT kręgosłupa. W związku z tym, należy ostrożnie stosować wspomnianą operację tak, aby nie usunąć z przetwarzanych obrazów informacji istotnej z punktu widzenia celu realizowanych badań.

The Influence of the Normalisation of Spinal CT Images on the Significance of Textural Features in the Identification of Defects in the Spongy Tissue Structure

Róża Dzierżak[1(✉)], Zbigniew Omiotek[1], Ewaryst Tkacz[2], and Andrzej Kępa[3]

[1] Faculty of Electrical Engineering and Computer Science, Lublin University of Technology, Lublin, Poland
rozadzierzak@gmail.com
[2] Faculty of Biomedical Engineering, Silesian University of Technology, Zabrze, Poland
[3] Department of Radiology and Nuclear Medicine, Independent Public Clinical Hospital No. 4, Lublin, Poland

Abstract. The aim of the study was to determine the effect of normalisation of spinal CT images on the accuracy of automatic recognition of defects in the spongy tissue structure of the vertebrae on the thoracolumbar region. Feature descriptors were based on the grey-levels histogram, gradient matrix, run-length matrix, coocurrence matrix, autoregression model and wavelet transform. Six methods of feature selection were used: Fisher coefficient, minimisation of classification error probability and average correlation coefficients between chosen features, mutual information, Spearman correlation, heuristic identification of noisy variables, linear stepwise regression. Selection results were used to build 6 popular classifiers. The following values of individual classification quality factors were obtained (before normalisation/after normalisation): general accuracy of classification - 90%/82%, classification sensitivity - 89%/85%, classification specificity - 96%/82%, positive predictive value - 95%/95%, negative predictive value - 89%/84%. For the applied set of textural features, as well as the methods of selection and classification, image normalisation significantly worsened the accuracy of the automatic diagnosis of osteoporosis based on CT images of the spine. Therefore, it is necessary to use this operation with caution so as not to remove from the processed images information significant from the point of view of the purpose of the research.

Keywords: Osteoporosis · CT images · Image normalisation · Feature selection · Classification

1 Introduction

Bone tissue is an active tissue and is subject to the remodelling process throughout human life. The condition for its proper course is the balance between

E. Tkacz et al. (Eds.): IBE 2018, AISC 925, pp. 55–66, 2019.
https://doi.org/10.1007/978-3-030-15472-1_7

the excitation of osteoblast osteogenic activity and osteoclastogenesis and bone resorption. The disruption of this process leads to the loss of bone mass and the weakening of the spatial structure of the bone referred to as osteoporosis. This disease is metabolic, causing changes in the microarchitecture of the bone tissue consisting in the reduction of the number of bone beams in the spongy structure and a high risk of fractures. Although the overall bone mass of the entire skeleton decreases with age, some of its structures are particularly vulnerable. Highly risk areas are vertebrae, especially around the thoraco-lumbar section [1].

A commonly used diagnosis of osteoporosis is a densitometric examination involving the measurement of bone density. The X-ray absorptiometry method is used to study the entire skeleton or selected sites, particularly vulnerable to fractures. The bone mineral content determines the amount of minerals at the site of measurement, which divided by the surface area gives the bone mineral density (BMD). Therefore, this technique provides information on the correct mineral density of the entire study area, without the exact identification of the section where the defect occurs. The index corresponding to the standard deviation from the peak bone mass serves to qualify the patient as healthy or ill. Considering that it is a constant classification value of the indicator, there is a risk that it is not 100% adequate to each bone segment examined [2].

Due to doubts related to the correct and precise diagnostics of bone defects, new diagnostic solutions are still sought [3–6]. An opportunity to create an effective system is to use the spinal CT image results. Images from contemporary tomographs, in comparison with other medical imaging techniques, are characterised by high accuracy, high resolution and contrast. Thanks to the good quality of the obtained results, it is possible to analyse the texture of tissues [7]. Its aim is to find a set of parameters, called textural features, each of which is a numerical measure of a specific texture property [8]. To obtain the best information about the tissue under investigation, it is necessary to select appropriate pre-processing activities. This article presents the impact of the image normalisation process on changes in its significant textural features.

2 Materials and Methods

2.1 Material

The CT images of the thoraco-lumbar region from 13 healthy patients and 11 with osteoporosis were used for the analysis. From the series of images, cross-sections were selected on which the inside of the vertebra together with the spongy being is visible (Fig. 1).

The size of the separated samples was chosen so as to maximise the surface of the texture containing the potential information in the image of a vertebra with a cross-section. As a result, 168 samples with dimensions of 50×50 pixels were obtained, where 84 samples presented normal tissue structure and 84 samples showed defects in spongy tissue.

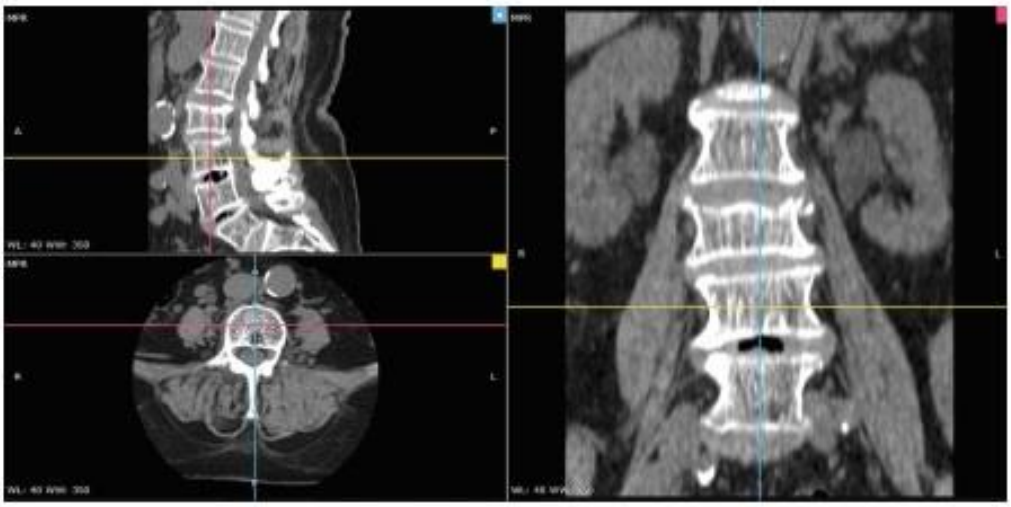

Fig. 1. Alignment of the axis in the centre of one of the vertebra (picture in three views).

2.2 Pre-processing

When analysing the texture of tissues, the pre-processing procedures should be limited in order not to distort the natural features of the images. Therefore, only the conversion from RGB mode to eight bit grey scale (two hundred and fifty six shades) was performed. The next step was to normalise the brightness range of the obtained samples with linear correction. The results are presented below (Fig. 2).

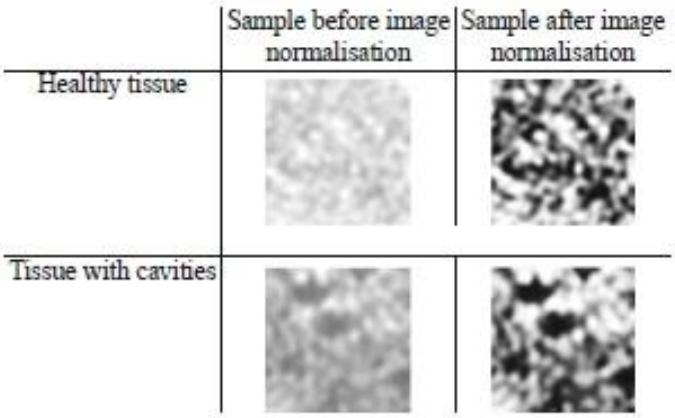

Fig. 2. Structure of spongy tissue before and after image normalisation.

2.3 Image Analysis

Image analysis was made with the MaZda program (version 4.6), developed at the Institute of Electronics of the Łódź University of Technology, whose author

is Piotr M. Szczypiński [9]. This program has been made available free of charge on the Internet for scientific purposes. It allows to analyse grey cardboard images and determine the numerical values of image features. A detailed description of these features can be found in [10–13], as well as in the MaZda documentation. The advantage of the program is that in addition to the statistical approach to image analysis, it also uses a mathematical model (autoregression model) and a transformational approach (wavelet transform). The set of features has been obtained on the basis of:

- Histogram (9 features): histogram's mean, histogram's variance, histogram's skewness, histogram's kurtosis, percentiles 1%, 10%, 50%, 90% and 99%.
- Gradient (5 features): absolute gradient mean, absolute gradient variance, absolute gradient skewness, absolute gradient kurtosis, percentage of pixels with nonzero gradient.
- Run length matrix (5 features $\times 4$ various directions): run length nonuniformity, grey level nonuniformity, long run emphasis, short run emphasis, fraction of image in runs.
- Coocurrence matrix (11 features $\times 4$ various directions $\times 5$ between-pixels distances) angular second moment, contrast, correlation, sum of squares, inverse difference moment, sum average, sum variance, sum entropy, entropy, difference variance, difference entropy.
- Autoregressive model (5 features): parameters 1, 2, 3, 4, standard deviation.
- Haar wavelet (24 features): wavelet energy (features are computed at 6 scales within 4 frequency bands LL, LH, HL, and HH).

The textural features obtained by the above methods have been used by the authors in previous studies, where they allowed for high classification accuracy of the thyroid ultrasound images [14].

2.4 Feature Selection

The results of image analysis were subjected to the process of reducing the dimension of feature space. The following selection methods were used [15–19]:

- Fisher coefficient (FC);
- minimisation of classification error probability and average correlation coefficients between chosen features (POE+ACC);
- mutual information (MI);
- Spearman correlation between chosen features and decision variable (SC);
- heuristic identification of noisy variables (HINoV);
- linear stepwise regression (LSR).

2.5 Classification

The complete set of data contained 168 observations, of which 84 were in the healthy category and 84 in the sick category. From this set, a training part (56

cases) and a test part (28 cases) were randomly selected. Thus, the training set was 2/3, and the test set was 1/3 of the full set. The training and testing procedure for classifiers was repeated 10 times. As the final result of the testing process, the average value from all tests was taken. This approach required the preparation of 10 training sets and 10 test sets for each data set. Determination of these sets was based on draws with returning. Six popular supervised learning

Table 1. Feature selection results.

Method	Not normalised images				Normalised images			
FC	Feature name	Fisher coeff.	Feature name	Fisher coeff.	Feature name	Fisher coeff.	Feature name	Fisher coeff.
	Perc.01%	3.2420	S(3,0)SumAverg	2.5486	S(0,5)SumAverg	0.5214	S(5,5)SumAverg	0.3893
	Perc.10%	2.9733	S(0,1)SumAverg	2.5422	S(0,4)SumAverg	0.5154	S(3,0)Entropy	0.3824
	Mean	2.5760	S(4,0)SumAverg	2.5408	S(0,3)SumAverg	0.4728	S(1,0)Entropy	0.3774
	S(1,0)SumAverg	2.5664	S(5,0)SumAverg	2.5340	S(5,0)Entropy	0.4369	S(4,0)Entropy	0.3722
	S(2,0)SumAverg	2.5567	S(1,-1)SumAverg	2.5303	S(0,2)SumAverg	0.3990	S(4,4)SumAverg	0.3709
POE+ ACC	Feature name	POE+ACC coeff.	Feature name	POE+ACC coeff.	Feature name	POE+ACC coeff.	Feature name	POE+ACC coeff.
	S(2,0)InvDfMom	0.4571	S(5,5)Entropy	0.5068	S(5,5)SumOfSqs	0.4731	S(0,5)SumAverg	0.5341
	Teta2	0.4824	S(1,0)Entropy	0.5072	S(4,4)SumEntrp	0.4866	S(1,-1)DifEntrp	0.5348
	S(5,0)SumAverg	0.4860	S(4,4)Entropy	0.5099	S(4,4)Entropy	0.5202	S(5,0)SumAverg	0.5380
	WavEnLL_s-1	0.4871	S(1,0)SumEntrp	0.5204	Perc.50%	0.5225	135dr_LngREmph	0.5416
	Mean	0.5043	WavEnLL_s-2	0.5952	S(0,3)Entropy	0.5252	Teta2	0.8869
MI	Feature name	Mutual inf. coeff.	Feature name	Mutual inf. coeff.	Feature name	Mutual inf. coeff.	Feature name	Mutual inf. coeff.
	WavEnLL_s-2	0.4937	S(0,1)SumAverg	0.4689	Teta2	0.1535	S(0,1)Correlat	0.1251
	S(1,1)SumAverg	0.4692	S(3,0)SumAverg	0.4686	S(0,1)DifEntrp	0.1352	S(3,3)SumOfSqs	0.1231
	S(1,-1)SumAverg	0.4692	Mean	0.4683	S(1,1)SumAverg	0.1345	S(2,-2)SumAverg	0.1224
	S(0,2)SumAverg	0.4692	S(1,0)SumAverg	0.4683	S(3,-3)SumAverg	0.1286	S(0,3)InvDfMom	0.1216
	S(0,3)SumAverg	0.4692	S(2,0)SumAverg	0.4683	S(4,-4)SumAverg	0.1262	S(0,5)SumAverg	0.1184
SC	Feature name	Spearman corr. coeff.	Feature name	Spearman corr. coeff.	Feature name	Spearman corr. coeff.	Feature name	Spearman corr. coeff.
	Perc.01%	-0.664066	S(2,0)SumAverg	-0.612954	S(1,0)AngScMom	-0.363675	S(1,0)Entropy	0.300463
	Perc.10%	-0.648436	S(4,0)SumAverg	-0.612709	S(2,0)AngScMom	-0.324153	S(2,0)Entropy	0.295063
	WavEnLL_s-2	-0.618355	S(3,0)SumAverg	-0.612709	S(0,4)SumAverg	0.317647	S(3,0)Entropy	0.292362
	Mean	-0.613936	WavEnLL_s-1	-0.612463	S(5,0)Entropy	0.311264	S(4,0)Entropy	0.292117
	S(1,0)SumAverg	-0.612954	S(0,1)SumAverg	-0.612218	S(0,5)SumAverg	0.307091	S(0,2)SumAverg	0.284631
HINoV	Feature name	Corrected Rand index	Feature name	Corrected Rand index	Feature name	Corrected Rand index	Feature name	Corrected Rand index
	S(4,4)Entropy	98.1598	S(2,-2)SumOfSqs	96.5498	S(0,4)DifEntrp	62.9893	S(0,3)DifEntrp	59.7709
	S(5,-5)Entropy	97.0083	S(0,1)SumOfSqs	96.4397	S(1,1)DifEntrp	61.8615	S(0,3)Correlat	59.6221
	S(4,4)AngScMom	96.9330	S(2,2)SumOfSqs	96.4305	S(2,2)DifEntrp	61.7884	S(3,0)Correlat	58.9342
	S(3,3)Entropy	96.8439	S(0,3)SumOfSqs	96.4305	GrMean	61.1595	S(2,2)DifVarnc	58.8955
	S(3,-3)Entropy	96.7139	S(3,3)SumOfSqs	96.4305	GrVariance	60.6692	S(2,2)Contrast	58.7767
LSR	Feature name	p-value	Feature name	p-value	Feature name	p-value	Feature name	p-value
	S(0,1)InvDfMom	5.1987e-09	S(4,4)InvDfMom	0.0483	S(1,0)DifVarnc	2.1316e-11	S(2,-2)DifVarnc	1.0875e-05
	Mean	7.0798e-07	S(5,5)InvDfMom	0.0736	S(1,1)SumEntrp	9.7742e-07	S(0,3)DifVarnc	8.4893e-05
	S(0,3)SumAverg	2.5439e-06			S(1,1)DifEntrp	1.4112e-06	S(0,3)InvDfMom	0.0939
	Teta2	4.9077e-06			S(0,5)SumAverg	3.3761e-06		

The symbols of the feature selection methods: FC - Fisher coefficient; POE+ACC - minimisation of classification error probability and average correlation coefficients between chosen features; MI - mutual information; SC - Spearman correlation between chosen features and decision variable; HINoV - heuristic identification of noisy variables; LSR - linear stepwise regression.

Table 2. Classification results.

Feature selection method	Not normalised images						Normalised images					
	Classifier	ACC	TPR	TNR	PPV	NPV	Classifier	ACC	TPR	TNR	PPV	NPV
FC	LDA	83.21	81.43	85.00	85.12	82.64	LDA	63.39	67.14	59.64	62.85	65.90
	QDA	82.32	**85.00**	79.64	81.19	**84.91**	QDA	**65.54**	68.57	62.50	64.76	66.74
	NBC	78.75	78.21	79.29	80.54	78.91	NBC	65.00	**78.93**	51.07	61.92	**71.58**
	DT	85.00	76.43	93.57	93.00	80.44	DT	61.43	67.14	55.71	61.70	62.75
	9-NN	**85.54**	75.36	**95.71**	**95.13**	80.23	3-NN	65.18	53.57	**76.79**	**70.11**	62.35
	RF	82.68	79.29	86.07	85.64	81.29	RF	63.21	66.43	60.00	62.65	64.63
POE+ACC	LDA	85.71	80.36	91.07	90.49	82.47	LDA	68.04	72.14	63.93	67.76	69.56
	QDA	89.11	**89.29**	88.93	89.12	**89.50**	QDA	**71.25**	**79.64**	62.86	68.55	**75.60**
	NBC	86.07	81.79	90.36	89.77	83.50	NBC	66.25	76.07	56.43	63.81	70.62
	DT	83.75	76.79	90.71	90.99	80.12	DT	63.57	61.43	65.71	64.27	64.65
	5-NN	**90.54**	85.71	**95.36**	**95.29**	87.29	5-NN	69.29	57.86	**80.71**	**75.44**	65.96
	RF	88.04	82.50	93.57	93.20	84.66	RF	70.18	70.00	70.36	70.74	70.82
MI	LDA	83.93	77.50	90.36	88.98	80.32	LDA	70.36	76.07	64.64	68.81	73.35
	QDA	**84.29**	**80.71**	87.86	86.91	**82.26**	QDA	**72.50**	69.64	**75.36**	**73.87**	71.58
	NBC	78.75	75.36	82.14	81.62	77.09	NBC	66.07	**82.14**	50.00	62.28	74.76
	DT	81.79	68.21	95.36	93.74	75.33	DT	66.43	60.00	72.86	69.68	65.29
	9-NN	81.43	66.79	**96.07**	**94.87**	74.72	9-NN	71.07	71.07	71.07	71.18	71.98
	RF	79.11	76.79	81.43	81.37	78.44	RF	72.32	75.71	68.93	71.20	**75.83**
SC	LDA	85.36	83.21	87.50	87.24	83.99	LDA	62.14	63.57	60.71	62.11	63.03
	QDA	**88.04**	**85.36**	90.71	90.29	**86.23**	QDA	**65.00**	75.71	54.29	63.18	68.92
	NBC	80.71	80.36	81.07	81.08	80.66	NBC	62.68	**80.36**	45.00	59.45	**70.05**
	DT	83.39	75.36	91.43	91.16	79.34	DT	59.29	70.71	47.86	58.95	62.09
	6-NN	85.36	77.14	**93.57**	**92.76**	80.53	1-NN	62.68	64.64	60.71	62.21	63.91
	RF	84.82	81.43	88.21	87.64	82.89	RF	64.11	63.93	**64.29**	**64.53**	64.50
HINoV	LDA	**67.14**	65.36	**68.93**	**68.18**	**66.94**	LDA	69.11	69.64	68.57	69.25	69.63
	QDA	60.89	**68.93**	52.86	60.13	63.63	QDA	**71.79**	**75.36**	68.21	**70.52**	**73.85**
	NBC	63.93	55.36	72.50	66.74	62.29	NBC	52.86	47.14	58.57	54.53	51.73
	DT	58.21	56.79	59.64	60.84	57.97	DT	56.25	59.29	53.21	56.62	57.04
	3-NN	60.71	62.86	58.57	60.59	61.13	1-NN	69.64	68.57	**70.71**	70.12	70.17
	RF	57.68	61.07	54.29	57.71	58.06	RF	65.18	64.29	66.07	65.41	65.38
LSR	LDA	87.68	83.93	91.43	90.85	85.22	LDA	**81.61**	81.43	81.79	**82.29**	81.80
	QDA	**90.00**	87.50	92.50	92.14	88.34	QDA	79.46	**85.36**	73.57	76.60	**83.73**
	NBC	80.89	74.29	87.50	85.72	77.42	NBC	68.75	77.14	60.36	66.77	73.08
	DT	84.29	75.36	**93.21**	**92.87**	79.74	DT	63.93	62.50	65.36	64.72	63.87
	1-NN	89.11	**88.57**	89.64	89.87	**88.97**	4-NN	74.29	66.43	**82.14**	79.11	71.22
	RF	86.255	79.64	92.86	91.75	82.35	RF	73.04	72.14	73.93	73.23	73.09

The meaning of the classifier symbols used in Table 2 is as follows: LDA, QDA - linear and quadratic discriminant analysis; NBC - naive Bayes classifier; DT - decision tree; *K*-NN - *K*-nearest neighbours; RF - random forests. The symbols of the classification quality indices: ACC - overall classification accuracy; TPR - classification sensitivity; TNR - classification specificity; PPV - positive predictive value; NPV - negative predictive value. All numerical values are expressed in %.

methods [20–25] were used: linear and quadratic discriminant analysis (QDA, LDA), naive Bayes classifier (NBC), decision tree (DT), K-nearest neighbours (K-NN) random forests (RF). To assess the accuracy of classifiers, the following were used: overall classification accuracy (ACC), true positive rate (TPR, classification sensitivity), true negative rate (TNR, classification specificity), positive predictive value (PPV) and negative predictive value (NPV).

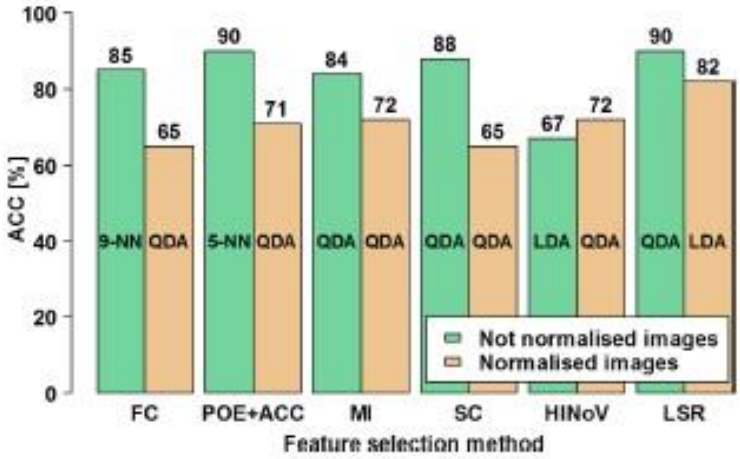

Fig. 3. Overall classification accuracy for individual feature selection methods.

3 Results

As a result of the image analysis, 290 descriptors of textural features were obtained. In the further part of the research, the dimension of the space of features was reduced. For this purpose, 6 selection methods were used, which are characterised in Subsect. 2.4. Table 1 presents the result obtained by each of the methods for the images before and after normalisation. Each of the first five methods of selection drew 10 features occupying the initial place in the ranking made according to its own coefficient. The sixth method, i.e. linear stepwise regression, returned 6 features for images before normalisation and 7 features for images after this operation. The data presented in Table 1 show that sets of features obtained by the same selection method are different for images before and after image normalisation. This is due to the fact that the operation mentioned changes the brightness of pixels, thus changing the results of the analysis.

The sets of features selected in the selection process were evaluated using six popular supervised classification methods. These were: linear and quadratic discriminant analysis, naive Bayes classifier, decision tree, K-nearest neighbours and random forests. The data sets needed for the construction and testing of classifiers were prepared as described in Sect. 2.5 Classification factors have been used to assess the quality of classification, which are often used in medical research (ACC, TPR, TNR, PPV, NPV). Detailed classification results are given in Table 2. For each method of feature selection, the bold font indicates the largest value of the appropriate classification quality factor. This allowed to indicate the classifier, which for the given selection method proved to be the best.

The best classification results in Table 2 are shown in bar charts (Figs. 3, 4 and 5). They present the values of individual indicators of the quality of classification, depending on the applied method of selection of features and image form (before and after normalisation). In addition, there is a symbol of the classification

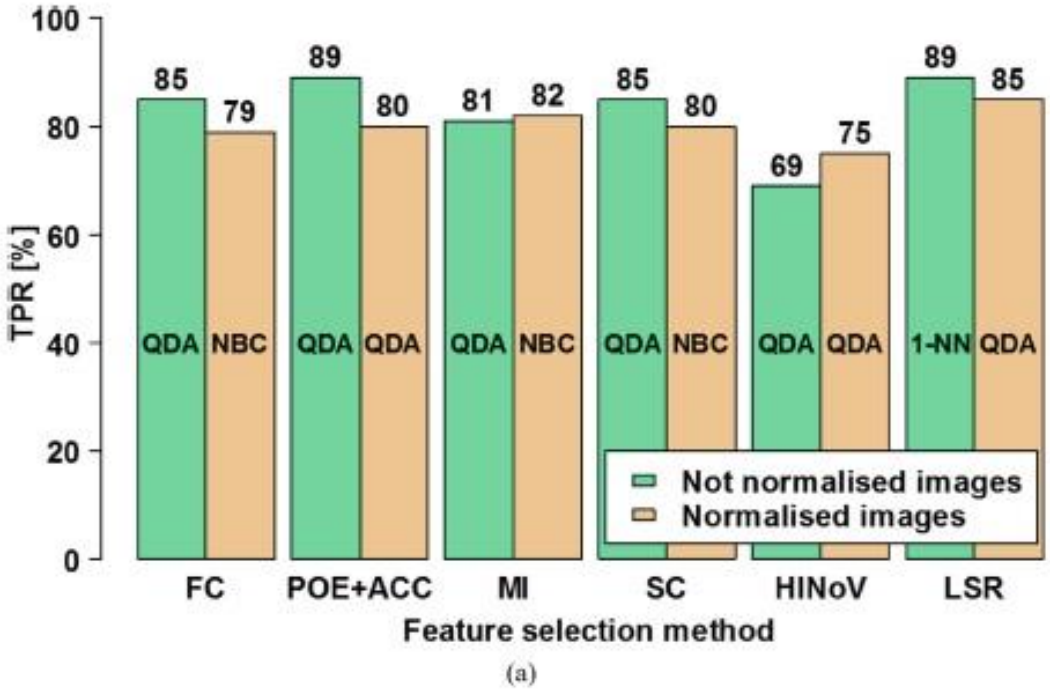

(a)

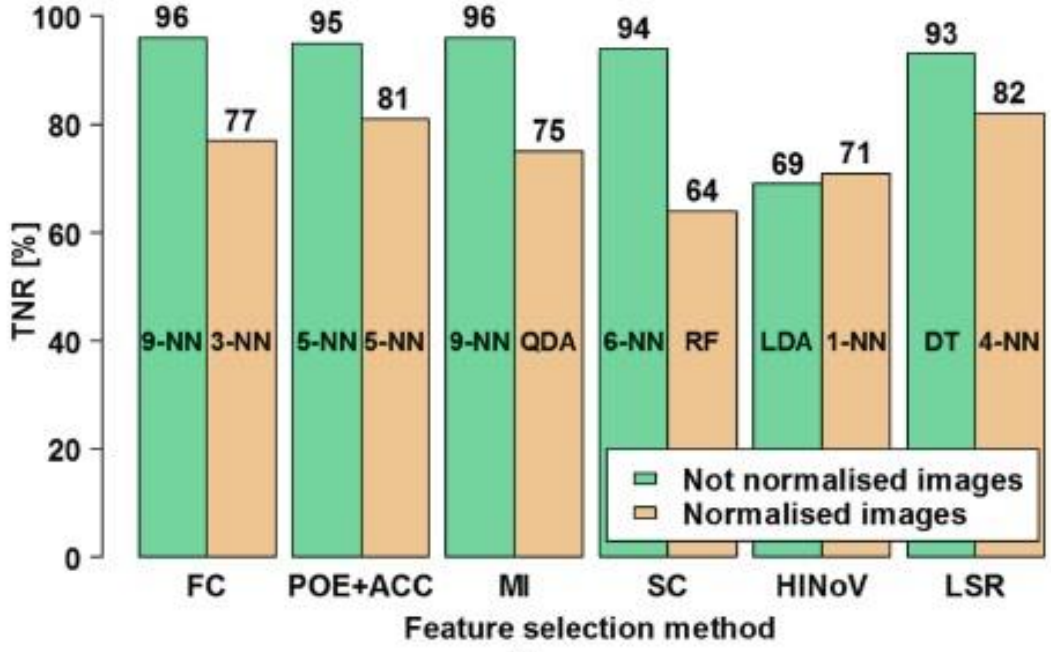

(b)

Fig. 4. Classification sensitivity (a) and specificity (b) for individual feature selection methods.

method in each bar graph, by means of which a given result was obtained. It should be noted that in almost all cases, a higher value of individual quality indicators was obtained for images without normalisation of brightness.

Table 3. A summary of the best classification results shown in Figs. 3, 4 and 5.

Index	Image	Value (%)	Method/Classifier
ACC	Not normalised	90	POE+ACC/5-NN, LSR/QDA
	Normalised	82	LSR/LDA
TPR	Not normalised	89	POE+ACC/QDA, LSR/1-NN
	Normalised	85	LSR/QDA
TNR	Not normalised	96	FC/9-NN, MI/9-NN
	Normalised	82	LSR/4-NN
PPV	Not normalised	95	FC/9-NN, POE+ACC/5-NN, MI/9-NN
	Normalised	95	POE+ACC/5-NN
NPV	Not normalised	89	POE+ACC/5-NN
	Normalised	84	LSR/QDA

4 Conclusions

Conducting the normalisation of the examined images caused a change in the brightness of individual pixels. As a result, the textural features of the images changed, as demonstrated by the results of the analysis. The sets of descriptors, obtained as a result of the chosen selection methods, were different for the images before and after the normalisation. The individual sets of features were evaluated in terms of the accuracy of the automatic classification of images into healthy and sick (osteoporotic) cases. Almost all of the applied classification quality factors achieved a higher value for images without normalisation of brightness. Differences in deterioration in accuracy, as a result of normalisation, ranged from 4% for TPR to 14% for ACC. The exception was the PPV coefficient, which did not change as a result of the normalisation.

The obtained results showed that the pre-processing operations should be carefully selected, because they do not always lead to improvement of the intended effects. Normalisation, by extending the range of shades to the maximum acceptable, improves the quality of the image, making it easier to distinguish the details on it. However, as research has shown, information that is important from the point of view of texture recognition may be lost. For the applied feature descriptors and classification methods, normalisation of spinal CT images led to the deterioration of the accuracy of the automatic diagnosis of osteoporosis. Therefore, this operation should not be recommended for use in the context of the present Research.

References

1. Downey, P.A., Siegel, M.I.: Bone biology and the clinical implications for osteoporosis. Phys. Ther. **86**, 77–91 (2006)
2. Marcus, R., Feldman, D., Dempster, D., Luckey, M., Cauley, J.: Osteoporosis, 4th edn. Academic Press (2013)
3. Reshmalakshmi, C., Sasikumar, M.: Trabecular bone quality metric from X-ray images for osteoporosis detection. In: 2017 International Conference on Intelligent Computing, Instrumentation and Control Technologies (ICICICT), pp. 1694–1697 (2017)
4. Nasser, Y., Hassouni, M., Brahim, A., Toumi, H., Lespessailles, E., Jennane, R.: Diagnosis of osteoporosis disease from bone X-ray images with stacked sparse autoencoder and SVM classifier. In: 2017 International Conference on Advanced Technologies for Signal and Image Processing (ATSIP), pp. 1–5 (2017)
5. Reshmalakshmi, C., Sasikumar, M.: Fuzzy inference system for osteoporosis detection. In: 2016 IEEE Global Humanitarian Technology Conference (GHTC), pp. 675–681 (2016)
6. Tejaswini, E., Vaishnavi, P., Sunitha, R.: Detection and prediction of osteoporosis using impulse response technique and artificial neural network. In: 2016 International Conference on Advances in Computing, Communications and Informatics (ICACCI), pp. 1571–1575 (2016)
7. Shahabaz, Somwanshi, D.K., Yadav, A.K., Roy, R.: Medical images texture analysis: a review. In: 2017 International Conference on Computer, Communications and Electronics (Comptelix), pp. 436–441 (2017)
8. Strzelecki, M., Materka, A.: Tekstura obrazów biomedycznych. Wydawnictwo Naukowe PWN (2017)
9. MaZda. www.eletel.p.lodz.pl/programy/cost/progr_mazda.html. Accessed 6 May 2018
10. Haralick, R.: Statistical and structural approaches to texture. Proc. IEEE **67**(5), 786–804 (1979)
11. Haralick, R., Shanmugam, K., Dinstein, I.: Textural features for image classification. IEEE Trans. Syst. Man Cybern. **3**(6), 610–621 (1973)
12. Hu, Y., Dennis, T.: Textured image segmentation by context enhanced clustering. IEE Proc.-Vis. Image Sig. Process. **141**(6), 413–421 (1994)
13. Lerski, R., Straughan, K., Shad, L., et al.: MR image texture analysis - an approach to tissue characterization. Magn. Reson. Imaging **11**, 873–887 (1993)
14. Omiotek, Z.: Improvement of the classification quality in detection of Hashimoto's disease with a combined classifier approach. Proc. Inst. Mech. Eng. Part H: J. Eng. Med. **231**(8), 774–782 (2017)
15. Shurmann, J.: Pattern Classification. Wiley, Hoboken (1996)
16. Dash, M., Liu, H.: Feature selection for classification. Intell. Data Anal. **1**(3), 131–156 (1997)
17. Tourassi, G.D., Frederick, E.D., Markey, M.K., Floyd, C.E.: Application of the mutual information criterion for feature selection in computer-aided diagnosis. Med. Phys. **28**(12), 2394–2402 (2001)
18. Carmone, F.J., Kara, A., Maxwell, S.: HINoV: a new method to improve market segment definition by identifying noisy rariables. J. Mark. Res. **36**, 501–509 (1999)
19. Omiotek, Z., Burda, A.: Feature selection methods in image-based screening for the detection of Hashimoto's thyroiditis in first-contact hospitals. Barometr Regionalny **14**(2), 187–196 (2016)

20. Breiman, L., Friedman, J., Olshen, R., et al.: Classification and Regression Trees. CRC Press, London (1984)
21. Enas, G.G., Chai, S.C.: Choice of the smoothing parameter and efficiency of the k-nearest neighbor classification. Comput. Math. Appl. **2**, 235–244 (1986)
22. Liao, S.H., Chu, P.H., Hsiao, P.Y.: Data mining techniques and applications - a decade review from 2000 to 2011. Expert. Syst. Appl. **39**, 11303–11311 (2012)
23. Quinlan, J.R.: Induction of decision trees. Mach. Learn. **1**, 81–106 (1986)
24. Venables, W.N., Ripley, B.D.: Modern Applied Statistics with S-PLUS. Springer, Berlin (1998)
25. Breiman, L.: Random forests. Mach. Learn. **45**, 5–32 (2001)

Lublin, 27.01.2023

mgr Andrzej Kępa
Zakład Radiologii Lekarskiej
Samodzielny Publiczny Szpital Kliniczny nr 4
w Lublinie

Oświadczenie współautora

Oświadczam, iż mój udział w przygotowaniu publikacji:

The Influence of the Normalisation of Spinal CT Images on the Significance of Textural Features in the Identification of Defects in the Spongy Tissue Structure / **Róża Dzierżak**, Zbigniew Omiotek, Ewaryst Tkacz, Andrzej Kępa. [W]: Innovations in Biomedical Engineering, Springer, s. 55-66, (2019).

wchodzącej w skład rozprawy doktorskiej Pani dr inż. Róży Dzierżak polegał na pomocy w zgromadzeniu danych obrazowych.

Andrzej Kępa
Podpis

Zabrze, 27.01.2023

prof. dr hab. inż. Ewaryst Tkacz
Wydział Inżynierii Biomedycznej/
Katedra Biosensorów i Przetwarzania Sygnałów Biomedycznych

Oświadczenie współautora

Oświadczam, iż mój udział w przygotowaniu publikacji:

The Influence of the Normalisation of Spinal CT Images on the Significance of Textural Features in the Identification of Defects in the Spongy Tissue Structure / Róża Dzierżak, Zbigniew Omiotek, Ewaryst Tkacz, Andrzej Kępa. [W]: Innovations in Biomedical Engineering, Springer, s. 55-66, (2019).

wchodzącej w skład rozprawy doktorskiej Pani dr inż. Róży Dzierżak polegał na konsultacji zakresu badań oraz ostatecznej wersji manuskryptu.

.....

Podpis

Dr hab. inż. Zbigniew Omiotek, prof. Uczelni
Wydział Elektrotechniki i Informatyki
Politechnika Lubelska

Lublin, 27.01.2023

Oświadczenie współautora

Oświadczam, iż mój udział w przygotowaniu publikacji:

The Influence of the Normalisation of Spinal CT Images on the Significance of Textural Features in the Identification of Defects in the Spongy Tissue Structure / **Róża Dzierżak**, Zbigniew Omiotek, Ewaryst Tkacz, Andrzej Kępa. [W]: Innovations in Biomedical Engineering, Springer, s. 55-66, (2019).

wchodzącej w skład rozprawy doktorskiej Pani dr inż. Róży Dzierżak polegał na przeprowadzeniu symulacji i wstępnej analizy otrzymanych wyników.

Zbigniew Omiotek
.....
Podpis

5. WYKAZ AKTYWNOŚCI I OSIĄGNIĘĆ NAUKOWYCH

Orcid: 0000-0001-5640-0204

WoS ResearcherID: D-6985-2017

Indeks Hirscha: **4** (wg Web of Science), **7** (wg Scopus)

Cytowania: **66** (wg Web of Science), **134** (wg Scopus)

Staże naukowe i wizyty studyjne:

- Wizyta studyjna w Zhejiang A & F University, Hangzhou, Chiny (2019 r.)
- Staż naukowy w Virginia Commonwealth University, Richmond, USA (2019 r.)
- Staż naukowy w Universidad Rey Juan Carlos w Madrycie, Hiszpania (2018 r. i 2019 r.)

Nagrody naukowe:

- Stypendium Prezydenta Miasta Lublin (dwukrotnie jako doktorantka w roku 2020 oraz 2018)
- Nagroda Rektora PL za działalność naukową (2020).

Moja aktywność obejmuje również działalność lokalną oraz ogólnopolską na rzecz środowiska akademickiego oraz działalność na rzecz popularyzacji nauki:

- Pełnienie funkcji Pełnomocnika Zarządu Krajowej Reprezentacji Doktorantów ds. naukowych i edukacyjnych (2020 r.)
- Pełnienie funkcji Przewodniczącej Rady Uczelnianej Samorządu Doktorantów PL (2018 – 2020)
- Organizacja wymiany studencko-doktoranckiej z Zhejiang A&F University w Chinach (2019 r.)
- Działalność w Lubelskim Porozumieniu Doktorantów (2020)
- Funkcja przedstawiciela doktorantów w Radzie Szkoły Doktorskiej w Politechnice Lubelskiej (2019 – 2020)
- Reprezentowanie doktorantów PL w Związku Uczelni Lubelskich (2018 – 2020)
- Udział w organizacji corocznych Warsztatów Doktorantów Wydziału Elektrotechniki i Informatyki
- Reprezentacja doktorantów PL w Senacie Politechniki Lubelskiej (2018 – 2020)

6. PODSUMOWANIE

Niniejszą rozprawę stanowi cykl czterech publikacji dotyczących diagnostyki osteoporozy na podstawie analizy obrazu CT tkanki gąbczastej kręgosłupa. Otrzymane wyniki świadczą o skuteczności zastosowanych metod. Metody te mogą stać się podstawą do stworzenia systemu automatycznej diagnostyki ubytków w mikroarchitekturze tkanki kostnej.

Najlepsze wyniki uzyskano w przypadku zastosowania modelu konwolucyjnej sieci neuronowej VGG16 charakteryzującego się najmniejszą głębokością topologiczną. Pozwoliło to na osiągnięcie dokładności klasyfikacji na poziomie 95%, a wartości parametrów TPR i TNR osiągnęły odpowiednio 96% i 94%. Porównywalnie dobre wyniki uzyskano za pomocą metody analizy tekstury obrazu rekonstrukcji miękkotkankowej, gdzie wszystkie trzy parametry ACC, TPR i TNR osiągnęły wartość 95%. Najmniejszą dokładność uzyskano w przypadku zastosowania analizy fraktalnej. W tym przypadku wyniki dla klasyfikatora K-NN (dla k=1 lub 10) wyniosły ACC=81%, TPR=78%, TNR=90%, PPV=90%, NPV=77%.

Przeprowadzone badania pokazują, że testowanie nowych metod pozwala osiągnąć coraz lepsze wyniki klasyfikacji obrazów tkanki gąbczastej, a tym samym stwarza podstawy do dalszych prac ukierunkowanych na diagnostykę osteoporozy. Kolejne, nieopublikowane jeszcze badania autorki bazujące na zastosowaniu koncepcji uczenia wieloinstancyjnego pozwoliły osiągnąć jeszcze lepsze niż dotychczas wyniki. W związku z tym autorka ma w planach kolejne działania związane z badaniami nad analizą i klasyfikacją obrazów pod kątem identyfikacji ubytków mikroarchitektury tkanki kostnej.

- Jako główny i najbliższy cel autorka założyła rozbudowę bazy danych obrazów CT kręgosłupa, co w ostatnich miesiącach ze względu na sytuację pandemiczną nie było możliwe do zrealizowania. Przeprowadzenie symulacji na większej liczbie próbek pozwoli zweryfikować działanie dotychczas stosowanych algorytmów oraz umożliwi testowanie metod wymagających większego zbioru danych obrazowych.
- Kolejnym ważnym aspektem, który jest niezbędny do uwzględnienia w dalszych pracach jest dołączenie do systemu predykcyjnego dodatkowej klasy obrazów reprezentujących osteopenię. Ma to kluczowe znaczenie w przygotowaniu systemu pozwalającego identyfikować ubytki tkanki kostnej już w początkowej fazie procesu chorobowego.

- Istotną kwestią jest również automatyczna segmentacja obszaru badanej tkanki z sekwencji obrazów DICOM uzyskiwanych podczas badania CT. W założeniu system diagnostyczny ma umożliwić maksymalnie prostą i szybką ocenę stanu tkanki w związku z czym proces segmentacji musi przebiegać w sposób zautomatyzowany. Tylko w takim wypadku istnieje szansa na wprowadzenie go do powszechnego użytku jako standardowej procedury diagnostycznej podczas wykonywania badań CT kręgosłupa.
- W dalszych planach autorka ma również dostosowanie opracowanych algorytmów do analizy tkanki kostnej w innych obszarach np. kości udowej lub przedramienia.

7. LITERATURA

1. Baravalle R, Thomsen F, Delrieux C, Lu Y, Gómez JC, Stošić B, Stošić T. *Three-dimensional multifractal analysis of trabecular bone under clinical computed tomography*, Med Phys. 44(12), 6404-6412, 2017. doi: 10.1002/mp.12603.
2. Błaszczyk B., Błaszczyk T., *Zastosowanie densytometru DXA w diagnostyce osteoporozy*, Inżynier i Fizyk Medyczny 9(3), 212—215, 2020.
3. Borowska M., Bębas E., Szarmach J., Oczeretko E., *Multifractal characterization of healing process after bone loss*, Biomedical Signal Processing and Control 52, 179−186, 2019.
4. Bouzeboudja O., Haddad B., Taleb-Ahmed A., Ameur S., El Hassouni M., Jennane R., *Multifractal analysis for improved osteoporosis classification*. Biomedical Signal Processing and Control, 80, 2023. 104225.
5. Buckley L., Solomon C.G., Humphrey M.B., *Glucocorticoid-Induced Osteoporosis*, New England Journal of Medicine 379, 2547−2556, 2018.
6. Chappard D., Pascaretti-Grizon F., Gallois Y., Mercier P., Baslé M.F., Audran M., *Medullar Fat Influences Texture Analysis of Trabecular Microarchitecture on X-Ray Radiographs*. Eur. J. Radiol., 58, 404–410, 2006. doi.org/10.1016/j.ejrad.2005.12.033.
7. *COVID-19 pandemic has dramatic impact on osteoporosis management, finds new global study*, International Osteoporosis Foundation (IOF), 2020.
8. Dhevendra A. P., Sivakumaran N., Sainarayanan G., Rachid J., *Multifractal-based lacunarity analysis of trabecular bone in radiography*, Compute. Biol. Med. 116, 2020.
9. Dzierżak R., Zastosowanie konwolucyjnych sieci neuronowych w diagnostyce osteoporozy, rozprawa doktorska, Politechnika Lubelska, Lublin 2020.
10. Emohare, O., Cagan, A., Morgan, R., Davis, R., Asis, M., Switzer, J., Polly, D.W. *The Use of Computed Tomography Attenuation to Evaluate Osteoporosis Following Acute Fractures of the Thoracic and Lumbar Vertebra*, Geriatr. Orthop. Surg. Rehabil. 5, 50–55, 2014. https://doi.org/10.1177/2151458514525042.
11. Fang, Y., Li, W., Chen, X., Chen, K., Kang, H., Yu, P., Li, S., *Opportunistic osteoporosis screening in multi-detector CT images using deep convolutional neural networks*, European Radiology 31, 1831−1842, 2021.
12. Fernandez−Cruz A., Ruiz−Antoran B., Munoz−Gomez A., Sancho−Lopez A., Mills−Sanchez P., Centeno−Soto GA, et al. *A Retrospective Controlled Cohort Study of the Impact of Glucocorticoid Treatment in SARS-CoV-2 Infection Mortality*, Antimicrob Agents Chemother, 64, 2020.

13. Gaidel A. V., Pervushkin S. S., *Research of the textural features for the bony tissue diseases diagnostics using the roentgenograms*, Comput. Opt. 37 (1), 113–119, 2013.
14. Gaidel A., Khramov A., *Application of Texture Analysis for Automated Osteoporosis Diagnostics by Plain Hip Radiography*, Pattern Recognit. Image Anal. 25, 301–305, 2015. https://doi.org/10.1134/S1054661815020108.
15. Guła Z., Korkosz M., *Osteoporoza u osób w wieku podeszłym — patogeneza, ocena ryzyka złamań i skuteczność przeciwzłamaniowa leków*, Medycyna Wieku Podeszłego 1 (1), 23–28, 2011.
16. Huang C, Wang Y, Li X, Ren L, Zhao J, Hu Y, et al. *Clinical features of patients infected with 2019 novel coronavirus in Wuhan, China*. Lancet, 395, 497−506, 2020.
17. *Informacja o sytuacji osób starszych w Polsce za 2021 r.,* Ministerstwo Rodziny i Polityki Społecznej, Warszawa, 2022.
18. Jang, R., Choi, J. H., Kim, N., Chang, J. S., Yoon, P. W., Kim, C. H., *Prediction of osteoporosis from simple hip radiography using deep learning algorithm*, Scientific reports 11(1), 2021.
19. Klibanski, A., Adams-Campbell, L., Bassford, T., Blair, S.N., Boden, S.D., Dickersin, K., Gifford, D.R., Glasse, L., Goldring, S.R., Hruska, K., et al. *Osteoporosis Prevention, Diagnosis, and Therapy*, JAMA 285, 785–795, 2001.
20. Leib E.S., Lewiecki E.M., Binkley N., Hamdy R.C., *International Society for Clinical Densitometry. Official positions of the International Society for Clinical Densitometry*, J. Clin. Densitom 7, 1–6, 2004.
21. Lespessailles E., Gadois C., Kousignian I., Neveu J.P., Fardellone P., Kolta S., Roux C., Do-Huu, J.P., Benhamou C.L., *Clinical Interest of Bone Texture Analysis in Osteoporosis: A Case Control Multicenter Study*, Osteoporos. Int. 19, 1019–1028, 2008. https://doi.org/10.1007/s00198-007-0532-8.
22. Lespessailles E., Gadois C., Lemineur G., Do-Huu J.P., Benhamou L., *Bone Texture Analysis on Direct Digital Radiographic Images: Precision Study and Relationship with Bone Mineral Density at the Os Calcis*, Calcif. Tissue Int. 2007, 80, 97–102. https://doi.org/10.1007/s00223-006-0216-y.
23. Mao L., Xia Z., Pan L., Chen J., Liu X., Li Z., Liu B., *Deep learning for screening primary osteopenia and osteoporosis using spine radiographs and patient clinical covariates in a Chinese population*, Frontiers in Endocrinology 13, 2022.
24. McCloskey E.V., Harvey N.C., Johansson H. et al. *Global impact of COVID-19 on non-communicable disease management: descriptive analysis of access to FRAX fracture risk*

online tool for prevention of osteoporotic fractures, Osteoporosis Int., 2020. https://doi.org/10.1007/s00198-020-05542-6

25. Mebarkia M., Meraoumia A., Houam L., Khemaissia S., X-*ray image analysis for osteoporosis diagnosis: From shallow to deep analysis*, Displays 76, 102343, 2023.
26. *Narodowy Fundusz Zdrowia, NFZ o zdrowiu. Osteoporoza*, raport, Centrala Narodowego Funduszu Zdrowia, Warszawa, listopad 2019.
27. *Osteoporoza - cicha epidemia w Polsce,* raport Europejskiej Fundacja Osteoporozy i Chorób Mięśniowo-Szkieletowych, Polskie Towarzystwo Ortopedyczne i Traumatologiczne, Kraków 2015.
28. Palanivel D. A., Natarajan S., Gopalakrishnan S., Jennane R., *Multifractal-based lacunarity analysis of trabecular bone in radiography*, Computers in biology and medicine 116, 2020. 103559.
29. Ran S.U., Liu T., Sun C., Jin Q., Jennane R., Leyi W., *Fusing convolutional neural network features with hand-crafted features for osteoporosis diagnoses*, Neurocomputing 385, 300–309, 2020.
30. Reid D. M., Devogelaer J. P., Saag K., Roux C., Lau C. S., Reginster J. Y., et al. *Zoledronic acid and risedronate in the prevention and treatment of glucocorticoid-induced osteoporosis (HORIZON): a multicentre, double-blind, double-dummy, randomised controlled trial*, The Lancet 373, 1253−1263, 2009.
31. Roczniak W., Babuśka-Roczniak M., Roczniak A., *Diagnostyka i farmakoterapia osteoporozy*, Lekarz 12, 14−22, 2010.
32. Smektała A., Dobosz A., *Osteoporoza – patofizjologia, objawy, profilaktyka i leczenie*, Farmacja Polska 76 (6), 2020. doi: 10.32383/farmpol/125762
33. Szafrański T., Kostyk T., Leszczyński P., *Interpretacja badañ densytometrycznych i morfometrycznych metodą DXA,* Przegląd Menopauzalny 5, 392–395, 2012. DOI: 10.5114/pm.2012.31465
34. Tang J., *COVID-19 Pandemic and Osteoporosis in Elderly Patients*, Aging Dis. 13(4), 960−969, 2022. doi: 10.14336/AD.2021.1201.
35. Ukon Y., Makino T., Kodama J., Tsukazaki H., Tateiwa D., Yoshikawa H., Kaito T., *Molecular-Based Treatment Strategies for Osteoporosis: A Literature Review*, International Journal of Molecular Sciences 20(10), 2557, 2019. https://doi.org/10.3390/ijms20102557.
36. van Staa T.P., Leufkens H.G., Cooper C., *The epidemiology of corticosteroid-induced osteoporosis: a meta-analysis*, Osteoporos Int, 13, 777−787, 2002.

37. Yousefi B., Valizadeh S., Ghaffari H., Vahedi A., Karbalaei M., Eslami M., *A global treatments for coronaviruses including COVID-19*, J Cell Physiol. 235(12), 9133–9142, 2020.
38. Zhang, B., Yu, K., Ning, Z., Wang, K., Dong, Y., Liu, X., Zhang, S. *Deep learning of lumbar spine X-ray for osteopenia and osteoporosis screening: A multicenter retrospective cohort study*, Bone 140, 2020. 115561.
39. Zheng K., Makrogiannis S., *Bone texture characterization for osteoporosis diagnosis using digital radiography*, in: 38th Annual International Conference of the IEEE Engineering in Medicine and Biology Society (EMBC), Orlando, FL, USA, 1034–1037, 2016.

8. ZAŁĄCZNIK 1

Tab. 8. 1 Próbki obrazowe tkanki gąbczastej zastosowane w badaniach – grupa kontrolna

1	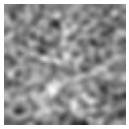	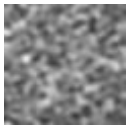	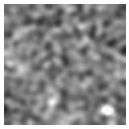	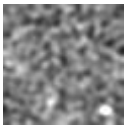
2	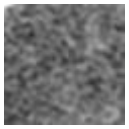	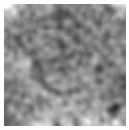	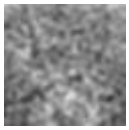	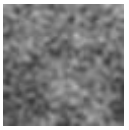
3	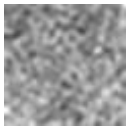	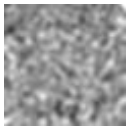	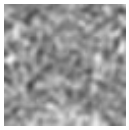	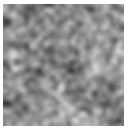
4	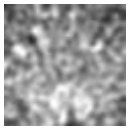	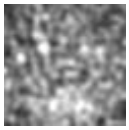		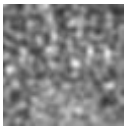
5	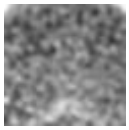	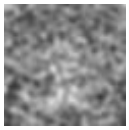	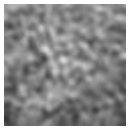	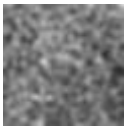
6	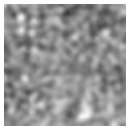	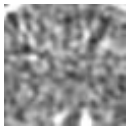	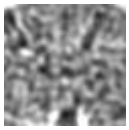	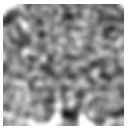
7	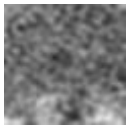		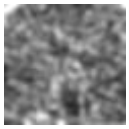	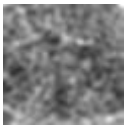
8	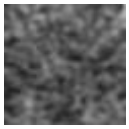	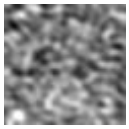	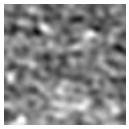	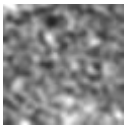
10	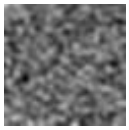	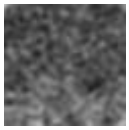	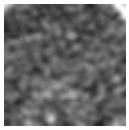	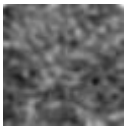
11	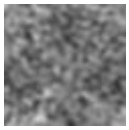	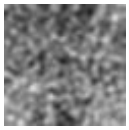	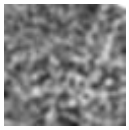	

12		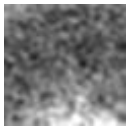	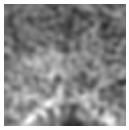	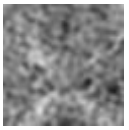
13	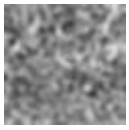		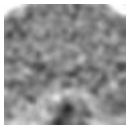	
14		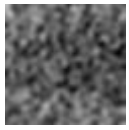	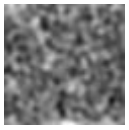	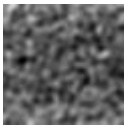
15	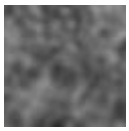	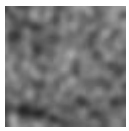		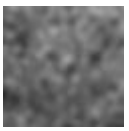
16	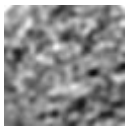	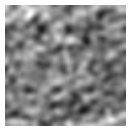	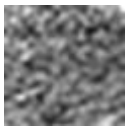	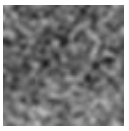
17		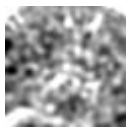	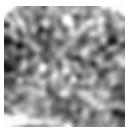	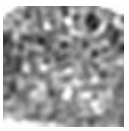
18	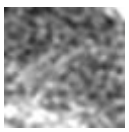		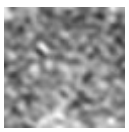	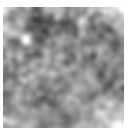
19	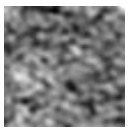	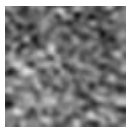	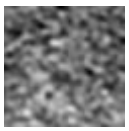	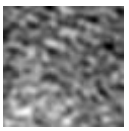
20	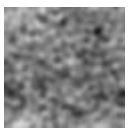		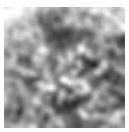	
21	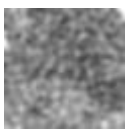	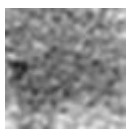	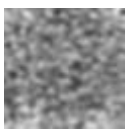	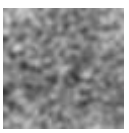
22				

23	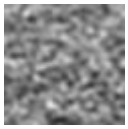	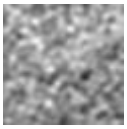	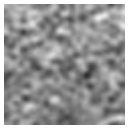	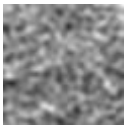
24	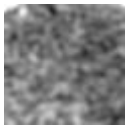	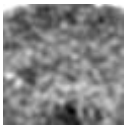	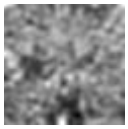	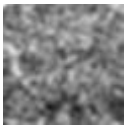
25		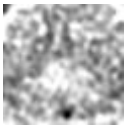		
26	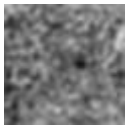	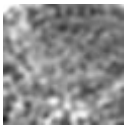	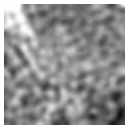	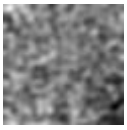
27	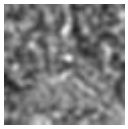	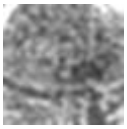	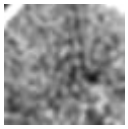	
28	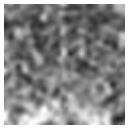			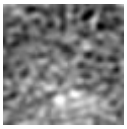
29	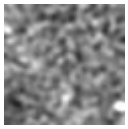	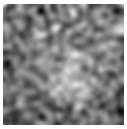	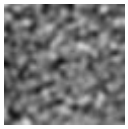	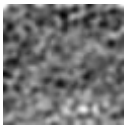
30	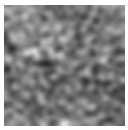	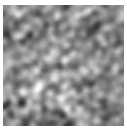	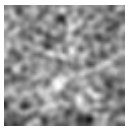	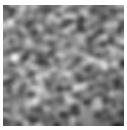
31	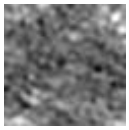	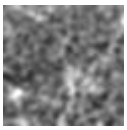		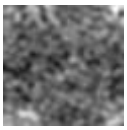
32		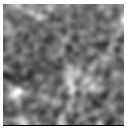	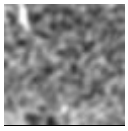	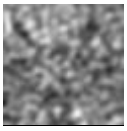
33				

34	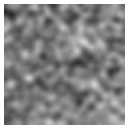	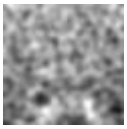		
35	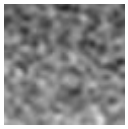	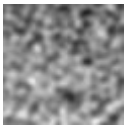	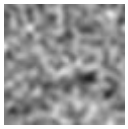	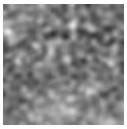
36	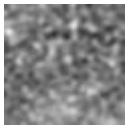	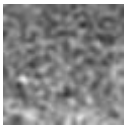	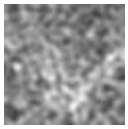	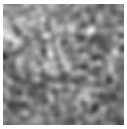
37	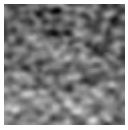	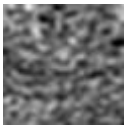		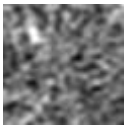
38	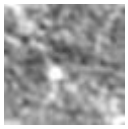			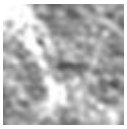
39	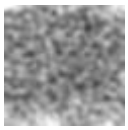	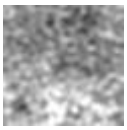	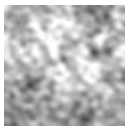	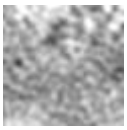
40	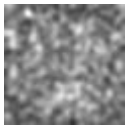	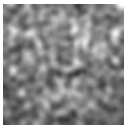	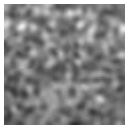	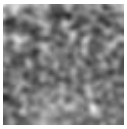
41	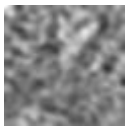	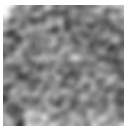	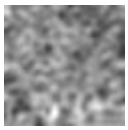	
42	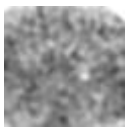		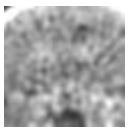	
43	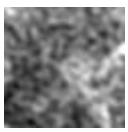	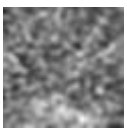	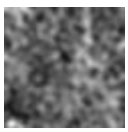	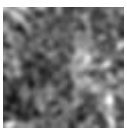

44	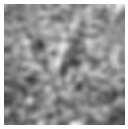	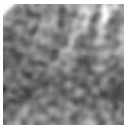	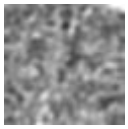	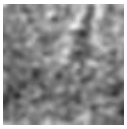
45	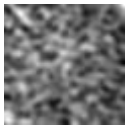	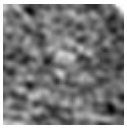	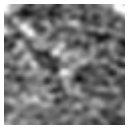	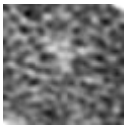
46	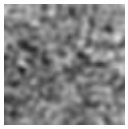	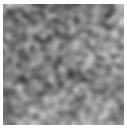	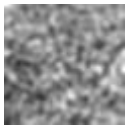	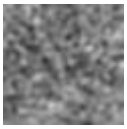
47	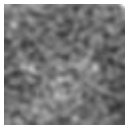	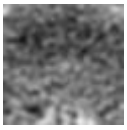	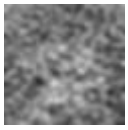	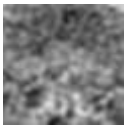
48	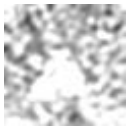		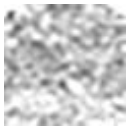	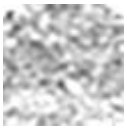
49	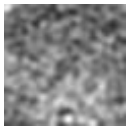	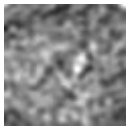	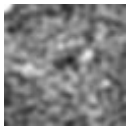	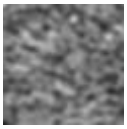
50	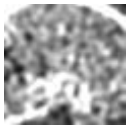	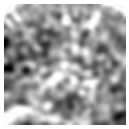		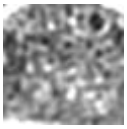

Tab. 8.2. Próbki obrazowe tkanki gąbczastej zastosowane w badaniach – grupa chorych.

1	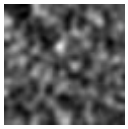	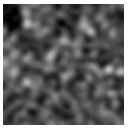	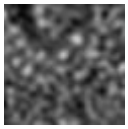	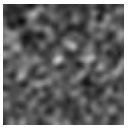
2		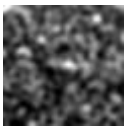	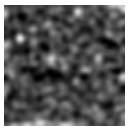	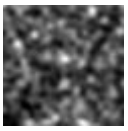
3	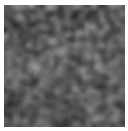	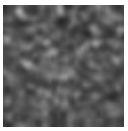	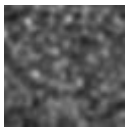	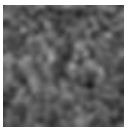
4		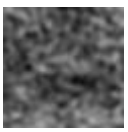	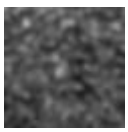	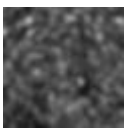
5	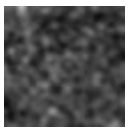	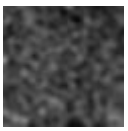	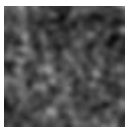	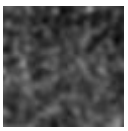
6	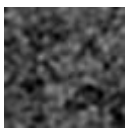	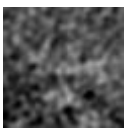	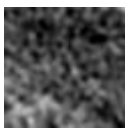	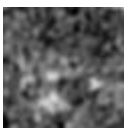
7	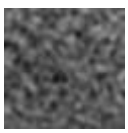	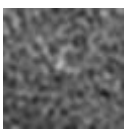	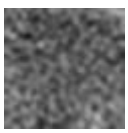	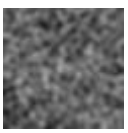
8	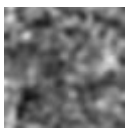		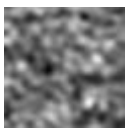	
10		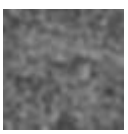		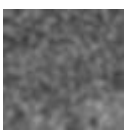
11	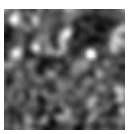	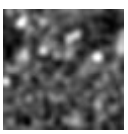	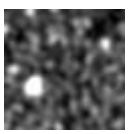	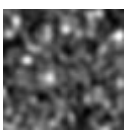

12	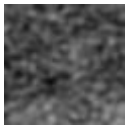	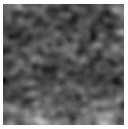	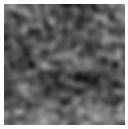	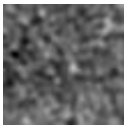
13	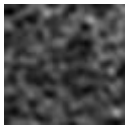	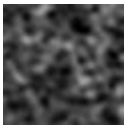	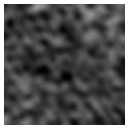	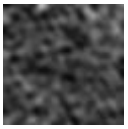
14	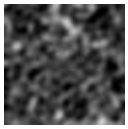	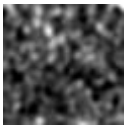	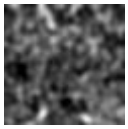	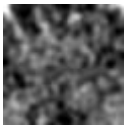
15	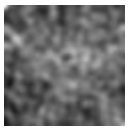		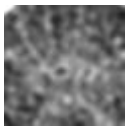	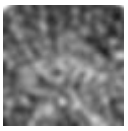
16	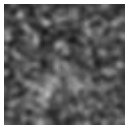	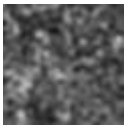	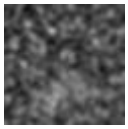	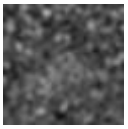
17	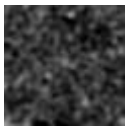	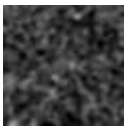	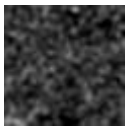	
18			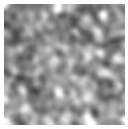	
19	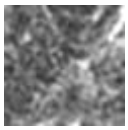	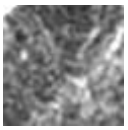	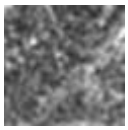	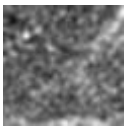
20		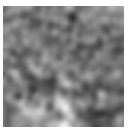	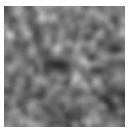	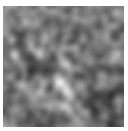
21	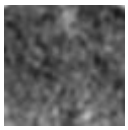	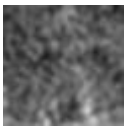	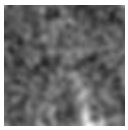	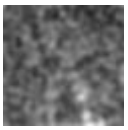

22	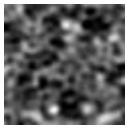	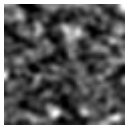	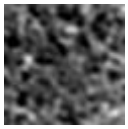	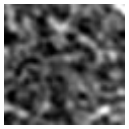
23	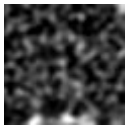		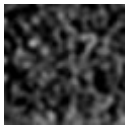	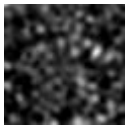
24		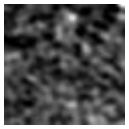	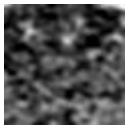	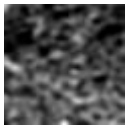
25	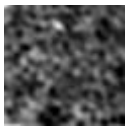	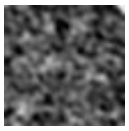	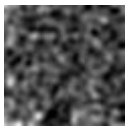	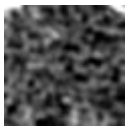
26	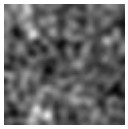	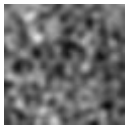	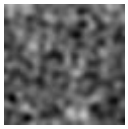	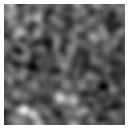
27	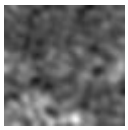	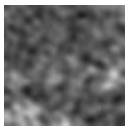	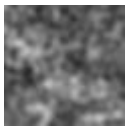	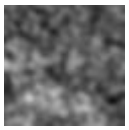
28	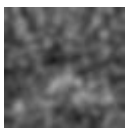	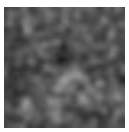	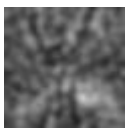	
29	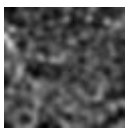	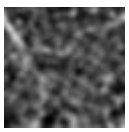	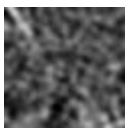	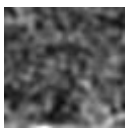
30		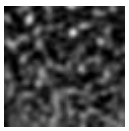	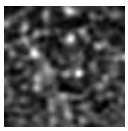	
31	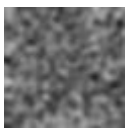	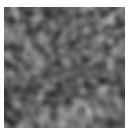	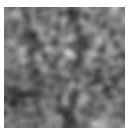	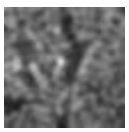

32		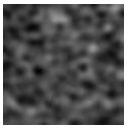	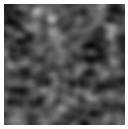	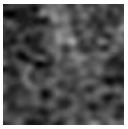
33	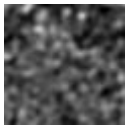	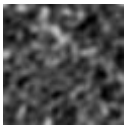	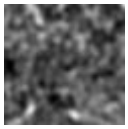	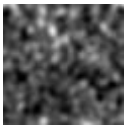
34	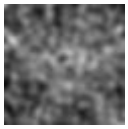	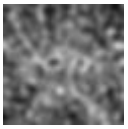	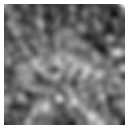	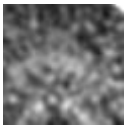
35	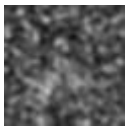	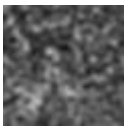	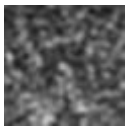	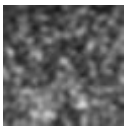
36	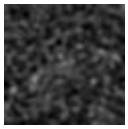	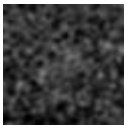	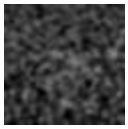	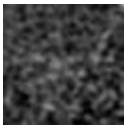
37		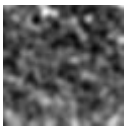	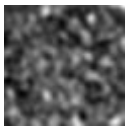	
38	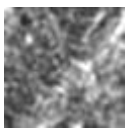	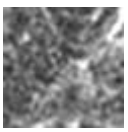	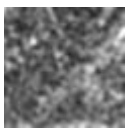	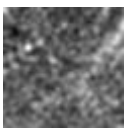
39	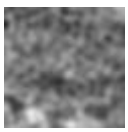	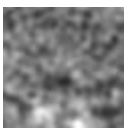	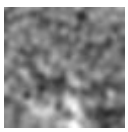	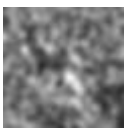
40	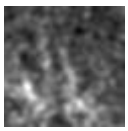	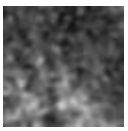		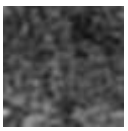
41	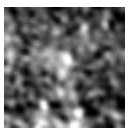	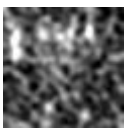	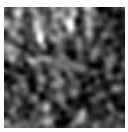	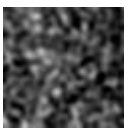

42	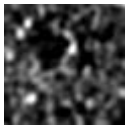	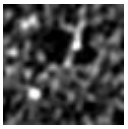	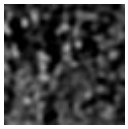	
43	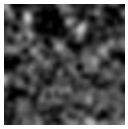	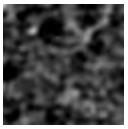	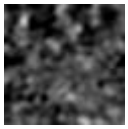	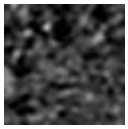
44	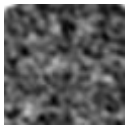	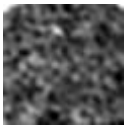	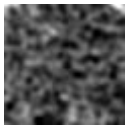	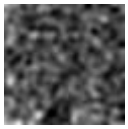
45	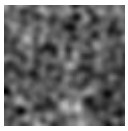	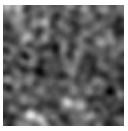		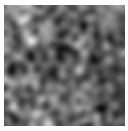
46	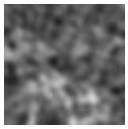		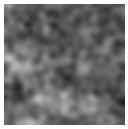	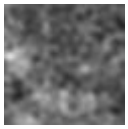
47	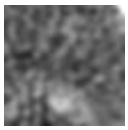	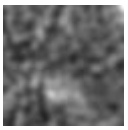	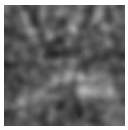	
48	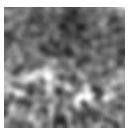	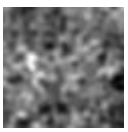	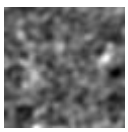	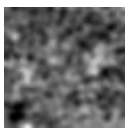
49	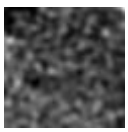	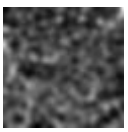	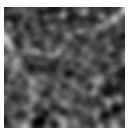	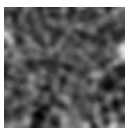
50	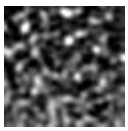	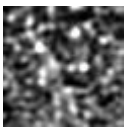	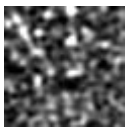	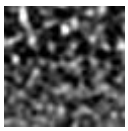

9. ZAŁĄCZNIK 2

Wykaz publikacji, które nie wchodzą w skład niniejszej rozprawy

Artykuły:

1. *An integrated texture analysis and machine learning approach for durability assessment of lightweight cement composites with hydrophobic coatings modified by nanocellulose* / Danuta Barnat-Hunek, Zbigniew Omiotek, Małgorzata Szafraniec, Róża Dzierżak // Measurement.- 2021, vol. 179, s. 1−20 [MNiSW: 200].
2. *Analiza skuteczności wybranych metod segmentacji struktur anatomicznych mózgu* / Róża Dzierżak, Magdalena Michalska // Informatyka, Automatyka, Pomiary w Gospodarce i Ochronie Środowiska.- 2018, vol. 8, nr 2, s. 58−61 [MNiSW: 7].
3. *Application of neural networks in the classification of medical images textures* / Róża Dzierżak, Waldemar Wójcik // Iskusstvennyj Intellekt-Naučno-Teoretičeskij Žurnal (Искусственный Интеллект).- 2018, vol. 79, nr 1, s. 49−55.
4. *Comparison of the influence of standardization and normalization of data on the effectiveness of spongy tissue texture classification* / Róża Dzierżak // Informatyka, Automatyka, Pomiary w Gospodarce i Ochronie Środowiska.- 2019, vol. 9, nr 3, s. 66−69 [MNiSW: 20]
5. *Fractal analysis of the computed tomography images of vertebrae on the thoraco-lumbar region in diagnosing osteoporotic bone damage* / Zbigniew Omiotek, Róża Dzierżak, Sebastian Uhlig // Proceedings of the Institution of Mechanical Engineers Part H-Journal of Engineering in Medicine.- 2019, vol. 233, nr 12, s. 1269−1281 [MNiSW: 40]
6. *The influence of the principal component analysis of texture features on the classification quality of sponge tissue images* / Róża Dzierżak // Informatyka, Automatyka, Pomiary w Gospodarce i Ochronie Środowiska.- 2020, vol. 10, nr 3, s. 13−16 [MNiSW: 20]
7. *Usage of application osirix in the evaluation of the aortic contractility in patients examined by computer heart tomography* / Róża Dzierżak, Ryszard Maciejewski, Sebastian Uhlig // Information Innovative Technologies.- 2017, nr 1, s. 236−240.

Rodziały monografii:

1. *An approach to determination of the criteria of harmony of biological objects* / Olena V. Vysotska, Konstantin V. Nosov, Marine Georgiyants, Yurii Balym, Yurii

G. Bespalov, Petr Kabalyants, Hanna Dobrorodnia, Nataliia B. Savina, Andrii I. Bezuglyi, Róża Dzierżak, Aliya Aizhanova. [W]: Photonics Applications in Astronomy, Communications, Industry, and High-Energy Physics Experiments 2018.- 2018, s. 1012−1020 [MNiSW: 15]

2. *Analysis of vertebrae segmentation methods in computed tomography images* / Róża Dzierżak, Magdalena Michalska, Khassen Dassibekov. [W]: Photonics Applications in Astronomy, Communications, Industry, and High-Energy Physics Experiments 2018.- 2018, s. 1130−1138 [MNiSW: 15]
3. *Assessment of Pesticide Phytotoxicity with the Bioindication Method* / Roman V. Petruk, Natalia M. Kravets, Serhii M. Kvaterniuk, Yuriy M. Furman, Róża Dzierżak, Mukaddas Arshidinova, Assel Jaxylykova. [W]: Biomass as Raw Material for the Production of Biofuels and Chemicals.- 2022, s. 43−52 [MNiSW: 50]
4. *Automated method for structural segmentation of nasal airways based on cone beam computed tomography* / Maksym Yu. Tymkovych, Oleg G. Avrunin, Victor G. Paliy, Maksim Filzow, Oleksandr Gryshkov, Birgit Glasmacher, Zbigniew Omiotek, Róża Dzierżak, Saule Smailova, Ainur Kozbekova. [W]: Photonics Applications in Astronomy, Communications, Industry, and High-Energy Physics Experiments 2017.- 2017, s. 1039−1046 [MNiSW: 15]
5. *Cereals role in carbon dioxide absorption in China and Poland* / Lucjan Pawłowski, Małgorzata Pawłowska, Wojciech Cel, Katarzyna Wójcik-Oliveira and Róża Dzierżak, Lei Wang, C. Li, Guomo Zhou. [W]: The Role of Agriculture in Climate Change Mitigation.- 2020, s. 40−44 [MNiSW: 20]
6. *Comparison of the effectiveness of tree algorithms in the diagnosis of spongy tissue* / Róża Dzierżak, Zbigniew Omiotek, Waldemar Wójcik. [W]: IIPhDW 2019: International Interdisciplinary PhD Workshop.- 2019, s. 1−4 [MNiSW: 20]
7. *Device to determine the level of peripheral blood circulation and saturation* / T. I. Kozlovska, Sergii V. Sander, Sergii M. Zlepko, Valentina B. Vasilenko, Volodymyr S. Pavlov, Victoria P. Dumenko, A. Klapouschak, Marcin Maciejewski, Róża Dzierżak, Wojciech Surtel. [W]: Photonics Applications in Astronomy, Communications, Industry, and High-Energy Physics Experiments 2016 [WOS].- 2016, s. 816−821 [MNiSW: 15]
8. *Double-compression method for biomedical images* / Yevhenii A. Antonenko, Timofey N. Mustetsov, Rami R. Hamdi, Teresa Małecka-Massalska, Nurbek Orshubekov, Róża Dzierżak, Svetlana Uvaysova. [W]: Photonics Applications in Astronomy,

Communications, Industry, and High-Energy Physics Experiments 2017.- 2017, s. 1115−1124 [MNiSW: 15]

9. *Evaluation of aortic contractility based on analysis of CT images of the heart* / Róża Dzierżak, Ryszard Maciejewski, Sebastian Uhlig. [W]: Photonics Applications in Astronomy, Communications, Industry, and High-Energy Physics Experiments 2017.- 2017, s. 1206−1211 [MNiSW: 15]
10. *Human ECG indicators for fast screening and evaluation* / Marcin Maciejewski, Róża Dzierżak, Wojciech Surtel, Tomasz Saran. [W]: Photonics Applications in Astronomy, Communications, Industry, and High-Energy Physics Experiments 2016 [WOS].- 2016, s. 833−838 [MNiSW: 15]
11. *Improving the quality of the ECG signal by filtering in wavelet transform domain* / Róża Dzierżak, Wojciech Surtel, Marcin Maciejewski, Grzegorz Dzida. [W]: Photonics Applications in Astronomy, Communications, Industry, and High-Energy Physics Experiments 2016 [WOS].- 2016, s. 1420−1424 [MNiSW: 15]
12. *Information model for the evaluation of the efficiency of osteoplasty performing in case of amputations on below knee* / Yurii O. Bezsmertnyi, Viktor I. Shevchuk, Olexander V. Grushko, Sergii V. Tymchyk, Halyna V. Bezsmertna, Róża Dzierżak, Khassen Dassibekov. [W]: Photonics Applications in Astronomy, Communications, Industry, and High-Energy Physics Experiments 2018.- 2018, s. 1063−1070 [MNiSW: 15]
13. *Medical expert system for assessment of coronary heart disease destabilization based on the analysis of the level of soluble vascular adhesion molecules* / Valentina K. Serkova, Sergey V. Pavlov, Valentina A. Romanava, Yuriy I. Monastyrskiy, Sergey M. Ziepko, Nanaliya V. Kuzminova, Waldemar Wójcik, Róża Dzierżak, Aliya Kalizhanova, Gulzhan Kashaganova. [W]: Photonics Applications in Astronomy, Communications, Industry, and High-Energy Physics Experiments 2017.- 2017, s. 1107−1114 [MNiSW: 15]
14. *Method of indicators forecasting of biomedical images using a parallel-hierarchical network* / Leonid I. Timchenko, Nataliya I. Kokriatskaia, Sergii V. Pavlov, Dmytro S. Stepaniuk, Tatiana V. Sichko, Igor D. Ivasyuk, Róża Dzierżak, Saltanat Amirgaliyeva. [W]: Photonics Applications in Astronomy, Communications, Industry, and High-Energy Physics Experiments 2019.- 2019, s. 808−813 [MNiSW: 20]
15. *Metrological analysis of a neural network measuring system for medical purposes* / O. A. Avdeyuk, Yu. P. Mukha, D. N. Avdeyuk, M. G. Skvortsov, Z.Omiotek, R. Dzierżak, M. Dzieńkowski, A. Kozbakova. [W]: Information Technology in Medical

Diagnostics III : Metrological Aspects of Biomedical Research.- 2021, s. 65−80 [MNiSW: 50]

16. *Podstawowe metody segmentacji obiektów w obrazach medycznych* / Róża Dzierżak. [W]: Trendy i rozwiązania technologiczne – odpowiedź na potrzeby współczesnego społeczeństwa. T. 1.- 2017, s. 222−232 [MNiSW: 20]
17. *Polarimetric characterisation of histological section of skin with pathological changes* / Ronald H. Rovira, Stanislav Ye.Tuzhanskyy, S.V. Pavlov, Sergii N. Savenkov, Ivan S. Kolomiets, Vladyslav A. Stasenko, Marsia M. Bayas, Zbigniew Omiotek, Teresa Małecka-Massalska, Róża Dzierżak. [W]: Photonics Applications in Astronomy, Communications, Industry, and High-Energy Physics Experiments 2016 [WOS].- 2016, s. 930−933 [MNiSW: 15]
18. *Prevention of complications in children in the early postoperative period after surgical treatment of the single ventricle heart* / O.K.Nosovets, V.S.Yakymchuk, V.Y.Kotovskyi, E.M.Bairamov, V.G.Paliy, R.Dzierżak, K.Dassibekov. [W]: Information Technology in Medical Diagnostics II : proceedings of the International Scientific Internet Conference “Computer Graphics and Image Processing" and the XLVIIIth International Scientific and Practical Conference “Application of Lasers in Medicine and Biology".- 2019, s. 127−136 [MNiSW: 20]
19. *Protein Tertiary Structure Prediction with Hybrid Clonal Selection and Differential Evolution Algorithms* / Iryna Fefelova, Andrey Fefelov, Volodymyr Lytvynenko, Róża Dzierżak, Iryna Lurie, Nataliia Savina, Mariia Voronenko, Svitlana Vyshemyrska. [W]: Lecture Notes in Computational Intelligence and Decision Making : proceedings of the XV International Scientific Conference“Intellectual Systems of Decision Making and Problems of Computational Intelligence”(ISDMCI’2019), Ukraine, May 21–25, 2019.- 2020, s. 673−688 [MNiSW: 20]
20. *Przetwarzanie i analiza obrazów medycznych uzyskanych metodą tomografii komputerowej* / Róża Dzierżak. [W]: Aplikacyjne metody obliczeniowe oraz zarządzanie danymi.- 2017, s. 277−287 [MNiSW: 20]
21. *Quantum effects of electric potential hysteresis in biological macro objects* / Valeryy V. Boyko, Evgenyy I. Sokol, Petro M. Zamyatin, Pavlo F. Shchapov, Roman S. Tomashevskyi, Róża Dzierżak, Gali Duskazaev. [W]: Photonics Applications in Astronomy, Communications, Industry, and High-Energy Physics Experiments 2018.- 2018, s. 1046−1054 [MNiSW: 15]

22. *The complex degree of coherence of the laser images of blood plasma and the diagnostics of oncological changes of human tissues* / O.V.Dubolazov, A.G.Ushenko, Y.A.Ushenko, M.Yu.Sakhnovskiy, P.M.Grygoryshyn, N.Pavlyukovich, O.V.Pavlyukovich, V.T.Bachynskiy, S.V.Pavlov, R.Dzierżak, O.Mamyrbaev. [W]: Information Technology in Medical Diagnostics II : proceedings of the International Scientific Internet Conference “Computer Graphics and Image Processing" and the XLVIIIth International Scientific and Practical Conference “Application of Lasers in Medicine and Biology".- 2019, s. 185−194 [MNiSW: 20]
23. *The human body metabolism process mathematical simulation based on Lotka-Volterra model* / Andriy Oliynyk, Eugene Oliynyk, Olexandr Pyptiuk, Róża Dzierżak, Małgorzata Szatkowska, Svetlana Uvaysova, Ainur Kozbakova. [W]: Photonics Applications in Astronomy, Communications, Industry, and High-Energy Physics Experiments 2017.- 2017, s. 1080−1086 [MNiSW: 15]
24. *The optoelectronic sensor creatinine and urea* / Maria V. Vistak, Vasyl Ye. Dmytrakh, Ivan S. Diskovskyi, Lesya I. Kobylinska, Zinoviy M. Mikityuk, Vasyl S. Petryshak, Hryhoriy I. Barylo, Roman L. Holyaka, Yedilkhan Amirgaliyev, Wojciech Surtel, Róża Dzierżak. [W]: Photonics Applications in Astronomy, Communications, Industry, and High-Energy Physics Experiments 2017.- 2017, s. 1125−1130 [MNiSW: 15]
25. *The visualization quality improvement method of x-ray images with locally concentrated features (IMRI-method)* / Anatolii I. Povoroznyuk, Anna E. Filatova, Róża Dzierżak, Ulzhalgas Zhunissova. [W]: Photonics Applications in Astronomy, Communications, Industry, and High-Energy Physics Experiments 2019.- 2019, s. 214−224 [MNiSW: 20]
26. *Toxicity by Digestate of Methanogenic Processing of Biomass* / Volodymyr V. Nykyforov, Dmitrii M. Salamatin, Sergii V. Digtiar, Oksana A. Sakun, Leonid K. Polishchuk, Róża Dzierżak, Maksat Kalimoldayev, Yedilkhan Amirgaliyev. [W]: Biomass as Raw Material for the Production of Biofuels and Chemicals.- 2022, s. 155−170 [MNiSW: 50]
27. *Zastosowanie „deep learningu” w analizie obrazów medycznych* / Róża Dzierżak. [W]: Prace doktorantów Wydziału Elektrotechniki i Informatyki Politechniki Lubelskiej : wybrane zagadnienia z zakresu elektrotechniki i inżynierii biomedycznej.- 2018, s. 59−69 [MNiSW: 20]

28. *Zastosowanie klasyfikatorów tekstury w analizie obrazów medycznych* / Róża Dzierżak. [W]: Trendy i rozwiązania technologiczne – odpowiedź na potrzeby współczesnego społeczeństwa. T. 1.- 2017, s. 212−221 [MNiSW: 20]

Redakcja książek:

1. *Interdyscyplinarne prace doktorantów Politechniki Lubelskiej* / red.: Róża Dzierżak, Żaklin Maria Grądz.- Lublin : Wydawnictwo Politechniki Lubelskiej, 2019.- 192 s.- ISBN 978-83-7947-376-2 [MNiSW: 20]
2. *Interdyscyplinarność w badaniach naukowych : prace doktorantów Politechniki Lubelskiej* / red. Róża Dzierżak, Żaklin Maria Grądz.- Lublin : Wydawnictwo Politechniki Lubelskiej, 2020.- 181 s.- ISBN 978-83-7947-432-5 [MNiSW: 20]
3. *Prace doktorantów Politechniki Lubelskiej* / red. Róża Dzierżak, Żaklin Maria Grądz.- Lublin : Wydawnictwo Politechniki Lubelskiej, 2020.- 163, ISBN 978-83-7947-431-8 [MNiSW: 20]
4. *Prace doktorantów Wydziału Elektrotechniki i Informatyki Politechniki Lubelskiej : wybrane zagadnienia z zakresu elektrotechniki i inżynierii biomedycznej* / red.: Róża Dzierżak, Żaklin Grądz.- Lublin : Wydawnictwo Politechniki Lubelskiej, 2018.- 156 s. ISBN 978-83-7947-328-1 [MNiSW: 20]
5. *Wybrane zagadnienia z zakresu elektrotechniki, inżynierii biomedycznej i budownictwa: prace doktorantów Politechniki Lubelskiej* / red.: Róża Dzierżak, Żaklin Maria Grądz.- Lublin : Wydawnictwo Politechniki Lubelskiej, 2019.- 185 s. ISBN 978-83-7947-377-9 [MNiSW: 20]